Preprint typeset using LaTeX style emulateapj

THE KINEMATICS OF INTERMEDIATE REDSHIFT Mg II ABSORBERS[1]

Christopher W. Churchill[2]
Department of Astronomy and Astrophysics
The Pennsylvania State University
University Park, PA 16802
cwc@astro.psu.edu

AND

Steven S. Vogt
UCO/Lick Observatories
Board of Studies in Astronomy and Astrophysics
University of California, Santa Cruz, CA 96054
vogt@ucolick.org

The Astonomical Journal (2001) 122, in press (August)

ABSTRACT

We present 23 quasar absorption line systems selected by the Mg II $\lambda\lambda 2796, 2803$ doublet with $W_r(2796) > 0.3$ Å over the redshift range $0.4 \leq z \leq 1.2$. The kinematics and "profile morphologies" are studied at $\simeq 6$ km s^{-1} resolution to a 5 σ equivalent width detection threshold of $W_r(2796) = 0.015$ Å. We are thus sensitive to very weak "clouds" isolated in velocity. The absorption profiles were segregated into "kinematic subsystems", and the properties (velocities, velocity widths, column densities, etc.) were measured directly from the data and by Voigt profile modeling.

Most absorbers are characterized by a dominant kinematic subsystem with $W_r(2796) > 0.2$ Å and velocity spreads ranging from 10 to 50 km s^{-1} in proportion to the system equivalent width. Additional kinematic subsystems have velocities separations as large as 400 km s^{-1} relative to the dominant subsystem. The equivalent widths and velocity spreads of these weaker subsystems are anti–correlated with their velocities and their equivalent width distribution turns down from a power law below $W_r(2796) \simeq 0.08$ Å. These "moderate" and "high velocity" subsystems are inferred to have sub–Lyman limit H I, and therefore are probably not higher redshift analogues to Galactic high velocity clouds (HVCs).

Weak subsystems are asymmetrically distributed in velocity such that they are either all blueshifted or all redshifted with respect to the dominant subsystem. This implies, that although the "kinematic morphologies" vary greatly on a case–by–case basis, a given line of sight is apparently probing a well defined spatial and kinematic structure. We investigate a simple kinematic model that relies on a rotating disk to explain the observed asymmetries. There are systematic differences, or trends, in both the subsystem to subsystem velocity clustering and in the overall kinematic morphologies with increasing equivalent width; we discuss how these may provide clues to the observed differential evolution in the equivalent width distribution of Mg II absorbers.

Subject headings: (galaxies:) — quasar absorption lines; galaxies: — halos; galaxies: — kinematics and dynamics; galaxies: — ISM

1. INTRODUCTION

Ultimately, the goal of studying absorption lines in the spectra of quasars is to chart the details of cosmic evolution and to develop an understanding of the role of gas in the formation and evolution of galaxies. Strong metal–line absorption systems are excellent candidates for pursuing this line of research because metals are produced in stars, and stars are produced in galaxies. Furthermore, an α–group element is best suited since it is a tracer of the earliest stages of stellar evolution (i.e. Type II supernovae), and is not significantly produced in secondary or later stages. The resonant Mg II $\lambda\lambda 2796, 2803$ doublet is ideally suited for these reasons and for the reason that it is a low ionization species that traces neutral hydrogen column densities commonly associated with galaxy environments [i.e. Lyman limit systems; $\log N(\mathrm{H\,I}) \geq 17.3$ cm^{-2}].

Ground–based, low resolution ($\sim$ 1–2 Å) surveys searching for Mg II absorption systems in the spectra of quasars have yielded insights into the evolution of their number density, absorption cross section, and cosmological clustering over the redshift range $0.2 \leq z \leq 2.2$ (e.g. Lanzetta, Turnshek, & Wolfe 1987; Sargent, Steidel & Boksenberg 1988; Boissé et al. 1992; Steidel & Sargent 1992). In particular, Steidel & Sargent (1992, hereafter SS92) have presented a comprehensive look at the distributions of the equivalent widths, doublet ratios, and velocity clustering (on scales greater than 500 km s^{-1}). Mg II absorbers having rest–frame equivalent widths, $W_r(2796)$, greater than

[1]Based in part on observations obtained at the W. M. Keck Observatory, which is operated as a scientific partnership among Caltech, the University of California, and NASA. The Observatory was made possible by the generous financial support of the W. M. Keck Foundation.

[2]Work partially conducted while at UCO/Lick Observatories and the Board of Studies in Astronomy and Astrophysics, University of California, Santa Cruz, CA 96054

0.3 Å are consistent with a population of cosmologically distributed objects, i.e. galaxies. The co–moving redshift path density[3] is consistent with a non–evolving population of objects. However, as the sample is progressively restricted to stronger systems, evolution becomes progressively more pronounced with a high significance level; the strongest systems are evolving away with cosmic time. In other words, the mean $W_r(2796)$ increases with redshift.

In principle, this evolution could be attributed to changes in the mean quantity of gas, or in the chemical, ionization, and/or kinematic conditions in galaxies. It is unlikely that the chemical enrichment of the gas is decreasing with cosmic time, since the mean metallicity in the universe continues to increase. Bergeron et al. (1994) established that the mean ionization level in metal–line absorbers decreases with cosmic time over this same redshift interval. Bergeron et al. also reported finding sub–Lyman limit MgII absorbers at the lower end of the redshift interval, indicating that the HI gas mass may be decreasing with cosmic time in these systems. In tandem with the ionization evolution, this would indicate that the *total*, not just the neutral, gas mass is decreasing with cosmic time, and this could be linked to the observed MgII evolution.

On the other hand, perhaps the velocity spreads of the individual systems are decreasing with time. Petitjean and Bergeron (1990) studied ~ 30 MgII absorbing systems with a moderate resolution of 30 km s^{-1}. They resolved multi–component substructure in complex absorption profiles, measured the cloud–cloud velocity clustering on the scale of galaxy halo velocity dispersions, and established a correlation between the equivalent width and the number of subcomponents[4]. Since the doublet ratio does not evolve with redshift (SS92), it has been inferred that *each of the individual subcomponents* within an overall system is saturated, or nearly saturated. Indeed, Petitjean & Bergeron (1990) suggested that the typical subcomponent has a strength of $W_r(2796) \simeq 0.1$ Å, which is saturated for small Doppler parameters. The total equivalent width, then, would be proportional to the number and velocity spread of these individual, relatively narrow, saturated subcomponents. As another example of what could be governing the evolution– if the velocity spread is decreasing with cosmic time, the evolution in $W_r(2796)$ may not be due to a decrease in the gas mass, but due to the kinematics becoming more systematic or settled with time.

Now that the general statistics and evolution of MgII absorbers are established and that several important, but limited, observational clues are available for inferring what physically is evolving, the next logical step is to undertake a comprehensive study of the kinematics. The first goal is to simply establish the nature of the gas kinematics and the second is to investigate what physical processes are governing the redshift evolution in the $W_r(2796)$ distribution.

High–resolution spectra are required for resolving the absorption profiles into *individual* components for determining both the line–of–sight velocity distributions (kinematics) and the relative component–to–component absorption strengths. In addition, high signal–to–noise ratios are required for measuring weaker transitions with similar ionization potentials (esp. MgI and FeII). These transitions can provide clues to the ionization conditions, and, in the cases where the MgII profiles are saturated, provide the gas kinematics. With the advent of 8–10 meter class telescopes and efficient, very high–resolution spectrographs, it has become possible to acquire the requisite data in sufficient quantities.

In this paper, we present the high resolution ($\sim$ 6 km s^{-1}) absorption profiles of 23 MgII selected absorbing systems observed with the HIRES spectrograph (Vogt et al. 1994). In § 2, we present the observed quasars and briefly address the reduction and analysis of the data (i.e. how the varied, complex absorption profiles are parameterized into one to several quantified "properties"). The statistical properties of the sample and the individual absorbing systems are given in § 3. The observed distributions of the kinematics, absorption strengths, and column densities are presented in § 4, followed by discussions in § 5, § 6, and § 7. Conclusions are given in § 8.

2. OBSERVATIONS, DATA REDUCTION AND ANALYSIS

A total of 25 quasars were observed with the HIRES spectrometer (Vogt et al. 1994) on the Keck I telescope over the nights of 4–5 July 1994, 23–25 January 1995, and 19–20 July 1996 UT. HIRES was configured in first–order using the $0.861'' \times 7''$ decker, C1. Because of the first–order HIRES format, there are small gaps in the spectral coverage redward of 5100 Å where the free spectral range exceeds the width of the 2048×2048 Tektronix CCD. The $0.861''$ slit width disperses the light with $R = \lambda/\Delta\lambda = 45,000$ ($\simeq 6.6$ km s^{-1}) projected to $\simeq 3$ pixels per resolution element, $\Delta\lambda$.

Three separate, consecutive integrations were obtained for each quasar spectrum, bracketed by Th–Ar calibration lamps. In a given night, almost all quasars were observed with identical HIRES echelle and cross disperser settings, so the instrument was rarely reconfigured in a given night. At the time of the observations, there was no image rotator for HIRES, so the slit was not aligned with nor held constant with respect to the parallactic angle throughout the observations.

July runs were adversely affected by high, patchy cirrus clouds, so these spectra typically have lower signal–to–noise ratios. The January 1995 spectra were obtained in clear and stable $\sim 0.5''$ seeing conditions. In the continuum near the observed MgII profiles, the rest–frame equivalent width detection limit (5 σ) ranges from 0.008–0.016 Å.

2.1. *Sample Selection*

The absorbing systems were selected from the spectroscopic surveys of SS92 and Sargent, Steidel, & Boksenberg (1988). These surveys were complete to a 5 σ rest–frame equivalent width threshold of 0.3 Å. The spectra presented here are complete to 0.02 Å within ± 500 km s^{-1} of the MgII λ2796 optical depth centroids.

The quasars were selected based upon the criteria that each (1) was observable during the alloted telescope time,

[3]The redshift path density is defined as the number of objects per unit redshift. It constrains the product of the number density and physical cross section projected on the sky.

[4]This relationship had been proposed by York et al. (1986) and Wolfe (1986).

TABLE 1
JOURNAL OF OBSERVATIONS

Quasar	V [mag]	$z_{\rm em}$	Date [UT]	Exp [s]	λ Range [Å]
$0002+051$	16.2	1.90	1994 Jul 5	2700	3655.7–6079.0
$0117+213$	16.1	1.49	1995 Jan 23	5400	4317.7–6775.1
$0420-014$	17.0	0.92	1995 Jan 23	3600	3810.5–6304.9
$0454+039$	16.5	1.34	1995 Jan 22	4500	3765.8–6198.9
$0454-220$	15.5	0.53	1995 Jan 22	5400	3765.8–6198.9
$0823-223$	15.7	>0.92	1995 Jan 24	3600	3977.8–6411.8
$1101-264$[a]	16.1	2.14	···	100,200	3791.8–3847.8
$1148+384$	17.0	1.30	1995 Jan 24	5400	3986.5–6424.5
$1206+459$	16.1	1.16	1995 Jan 23	3600	3810.5–6304.9
$1222+228$	15.5	2.04	1995 Jan 23	3600	3810.5–6304.9
$1241+176$	15.4	1.28	1995 Jan 22	2400	3765.8–6189.9
$1248+401$	16.3	1.03	1995 Jan 22	4200	3765.8–6189.9
$1254+044$	16.0	1.02	1995 Jan 22	2400	3765.8–6189.9
$1317+274$	16.0	1.01	1995 Jan 23	3600	3810.5–6304.9
$1354+193$	16.0	0.72	1995 Jan 22	3600	3765.8–6189.9
$1421+331$	16.7	1.91	1995 Jan 23	3600	3818.6–6316.9
$1634+706$	14.9	1.34	1994 Jul 4,5	2700	3723.3–6185.7
$2128-123$	15.9	0.50	1996 Jul 19	3900	3766.2–5791.3
$2145+064$	16.3	1.00	1996 Jul 18	4500	3766.2–5791.3

[a]Observed with the IPCS on the AAT by M. Pettini and R. Hunstead.

(2) had $V \leq 17.5$ (in order to obtain a high signal–to–noise ratio in roughly a 3600 second integration), and (3) preferably had multiple systems along the line of sight that could be observed with a single setting of the HIRES echelle.

The journal of observations is listed in Table 1. Tabulated are the V magnitudes, the emission redshifts of the quasars, the UT date of observation, the total integration time in seconds, and the wavelength coverage (not including breaks above 5100 Å). Included is the spectrum of $Q1101-264$, which was observed with the IPCS on the AAT and generously donated to this study by M. Pettini.

2.2. *Data Reduction*

The HIRES data were reduced with the IRAF[5] APEXTRACT package (V2.10.3) for echelle data. Further details of the data reduction can be found in Churchill (1995), and Churchill (1997).

Each observed data frame was overscan subtracted, bias frame corrected, scattered light corrected, and flatfielded in the standard fashion. Cosmic rays were removed by averaging the frames with the IRAF task IMCOMBINE using the *crreject* option. This technique was possible only because the HIRES spectrograph was extremely stable between exposures; there was no quantifiable shifting of the cross disperser or echelle settings. The spectra were extracted using the optimal routines of Horne (1986) and Marsh (1989) as implemented by the IRAF APEXTRACT package. Also extracted were the uncertainty spectra and the sky spectra.

Due to the instrument stability, the Th–Ar lamps bracketing each series of quasar observations were simply added together for the wavelength calibration. The wavelengths were calibrated to vacuum using the "vacthar.dat" line list provided with the IRAF ECIDENTIFY task. For the dispersion correction, using DISPCORR, the spectra were *not* linearized, in that the data were not interpolated to enforce equal wavelength intervals per pixel. This preserves uncorrelated counts in each pixel and leaves the profile shapes unaltered. Finally, the heliocentric velocity correction was manually applied to each echelle order, where the heliocentric velocity was calculated using the IRAF RVCORR task.

The continuum flux was normalized using the methods described by Sembach & Savage (1992; also see Churchill 1997), where the fitting was performed interactively using the IRAF SFIT task embedded in an iterative script.

2.3. *Data Analysis*

2.3.1. *Feature Finding*

For each quasar spectrum, an objective line list of all 5 σ absorption features was constructed using a method very similar to the one described in Schneider et al. (1993). This method is optimal for finding unresolved lines (see Churchill et al. 2000a). The HIRES instrumental spread function (ISF) is well approximated as a Gaussian with $\sigma_{\rm ISF}(\lambda) = 0.0453(\lambda/5500)$ Å. In terms of the formalism of Schneider et al. , we set $J_0 = 6$. The HIRES spectra have 3 pixels per resolution element so that this value samples the ISF over 4.3 resolution elements (13 pixels).

2.3.2. *Feature Identification*

Line and line blending identifications were accomplished as follows. A list of roughly 100 transitions with accurate

[5]IRAF is distributed by the National Optical Astronomy Observatories, which are operated by AURA, Inc., under contract to the NSF.

TABLE 2
TRANSITIONS COVERED

Tran	$\lambda_{\rm vac}$ [Å]	f	$\Gamma \times 10^8$
FeII 2344	2344.214	0.1097	2.6800
FeII 2374	2374.4612	0.0282	2.9900
FeII 2383	2382.765	0.3006	3.1000
FeII 2587	2586.650	0.0646	2.7200
FeII 2600	2600.1729	0.2239	2.7000
MgII 2796	2796.352	0.6123	2.6120
MgII 2803	2803.531	0.3054	2.5920
MgI 2853	2852.964	1.8100	4.9500

rest–frame wavelengths (Morton 1991) was compiled. The literature was exhaustively searched for known absorption systems in each quasar and a list of their redshifts was constructed (even if the strong MgII and CIV doublets were not covered in our spectra). This list also included the redshifts of the discovered "weak" MgII systems (Churchill et al. 1999b). The point of including all known redshifts from the literature was to document line blending with transitions from other redshifts with those in our sample.

We then scanned the spectra at the expected location for each transition in our list. Output was a list identifying probable blends, i.e. instances when the expected wavelength locations covered by two or more different transitions from different redshifted systems overlapped. The final adopted identifications and limits were obtained by examining the spectra by hand. Very few blends were found and when they were, the details are given in the discussions of the individual systems.

In Table 2 we present the transitions included in our study. From left to right, the columns are the ionization species and transition identity, the vacuum laboratory wavelengths, the oscillator strengths, and the natural broadening constants. The atomic data are taken from the compilation of Morton (1991), except for the FeII λ2587 and λ2374 transitions, which are taken from Cardelli & Savage (1995). Tripp et al. (1996) review the reasons why these f values likely represent an improvement over the Morton values.

For this work, we include only the MgII, MgI, and FeII transitions that have been redshifted into our observed spectral range. In some systems, MnII, CaII, and TiII transitions were detected (see Churchill et al. 2000a). Since this work is focused primarily on the kinematics of MgII selected absorption systems, we present only the transition listed in Table 2. In the velocity ranges where MgII profiles are saturated, i.e. where kinematic information is lost, the FeII and MgI kinematics can be used assuming that they arise in the same ionization phase as the MgII. Note that there is now evidence for both a "warm" and a "cold" HI component in damped Lyman–α absorbers (DLAs) (Lane, Briggs, & Smette 2000); some of the MgI may arise in this separate "cold" phase (Rao 2000). It is possible that such multiphase structure is also present in Lyman–limit MgII absorbers and that MgI is partially arising in the "cold" phase.

2.3.3. *Defining Kinematic Subsystems*

Many of the overall absorption profiles are comprised of two to several absorption features that are separated by more than three pixels (i.e. a resolution element) of continuum flux. We quantify the properties for each of these separate absorption regions, which we call "kinematic subsystems". Kinematic subsystems are defined using only the MgII λ2796 transition. The wavelength region defining each kinematic subsystem is determined objectively by searching to either side of subsystem centroid for the wavelength at which the per pixel equivalent width (see Schneider et al. 1993; Churchill et al. 2000a) becomes insignificant, i.e. $W(\lambda_j) < \sigma_W(\lambda_j)$ where j denotes the pixel index (for a graphical example, see Figure 3 of Churchill et al. 1999b).

The MgII λ2796 profiles for each of the systems in our sample are presented in Figure 1. The upper subpanels show a rest–frame 1000 km s^{-1} range about the MgII λ2796 transition at its observed (redshifted) wavelength. Shaded regions indicate the wavelengths regions of each kinematic subsystem, which are numbered from blue to red. The lower subpanels show the 5 σ rest–frame equivalent width threshold, given by 5 $\sigma^2_{W(\lambda_i)}$, as a function of wavelength.

2.4. *Calculating Absorption Properties*

We compute most absorption properties directly from the flux values of the data. For the overall systemss, we compute the systemic redshift from the optical depth mean of the profile. For each kinematic subsystem, we compute the equivalent widths, velocities, velocity widths, and apparent column densities. We also parameterize the profiles using Voigt profile decomposition to measure the number of "clouds", their column densities, velocities, and Doppler parameters. The mathematical formalism is given in Appendix A.

Analysis of the VP results will be presented in a companion paper (Churchill, Vogt, & Charlton 2000). Here we simply describe the formalism and present the VP decomposition results for two reasons: (1) the model fits need to be presented with the data, and (2) inferences based upon VP results, whether statistical or for individual systems, absolutely require extensive simulations (e.g. Hu et al.

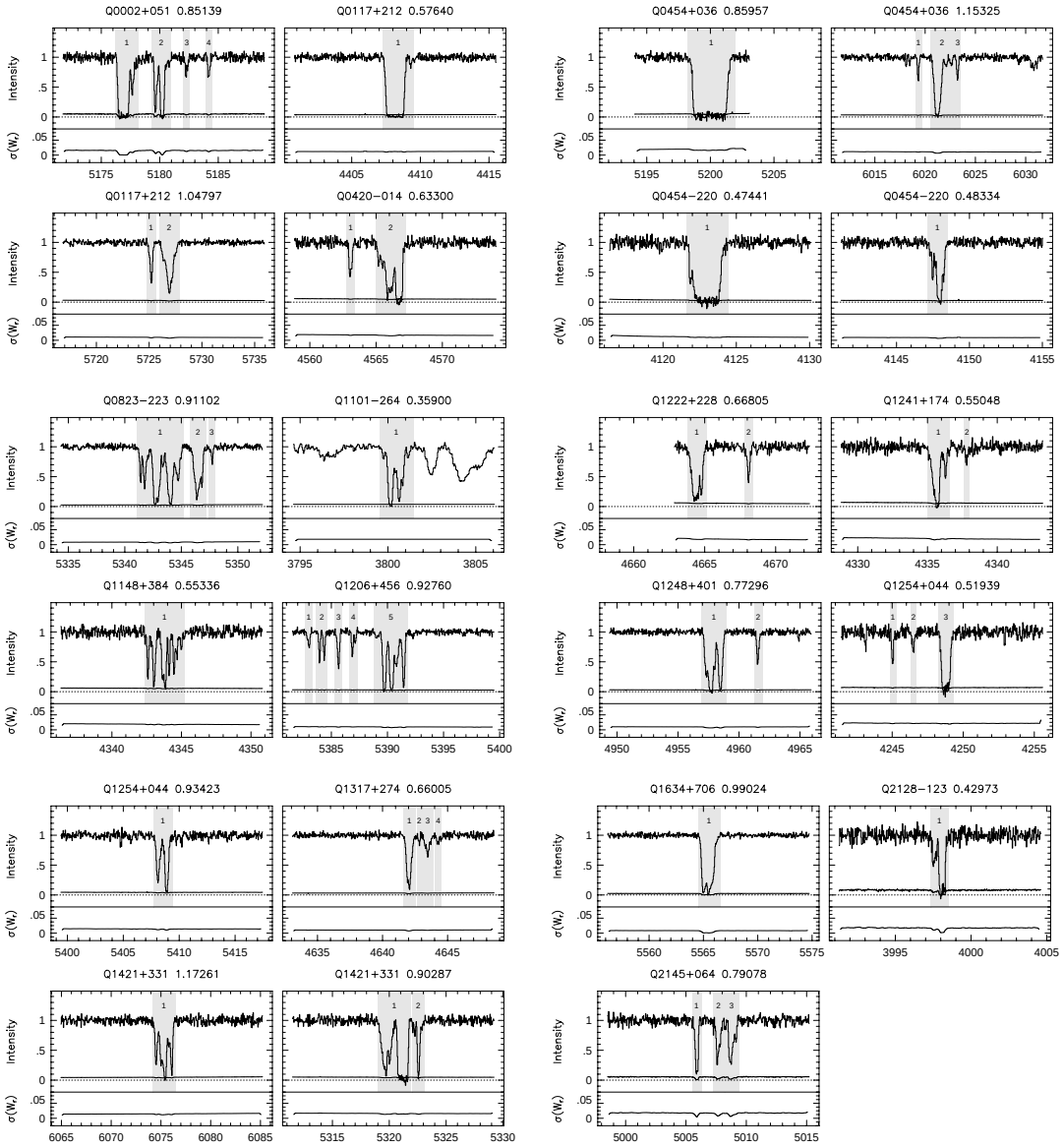

FIG. 1.— The normalized MgII λ2796 HIRES/Keck profiles and the 5 σ equivalent width detection thresholds presented as a function of observed wavelength. Each spectrum, however is plotted over a 1000 km s^{-1} span in its rest–frame. The shaded areas show where the kinematic subsystems have been defined. Throughout this work, they are identified by number from blue to red.

1995; Lu et al. 1996b) in order to establish the systematic effects of the fitting process. We will calibrate our VP results using simulations in the companion paper.

3. THE SYSTEMS

The HIRES data of the detected transitions are presented in Figure 2 (at the end of the paper). The profiles are aligned in rest–frame velocity, where $v = 0$ corresponds to λ_{sys} computed from Equation A1. Systems are defined to be all absorption that lies with $\pm$500km s^{-1} of the systemic velocity zero point. In no case is there a system, weak or strong, that lies anywhere near this velocity window; in practice, this velocity window could be increased to an arbitrarily large size.

Ticks above the normalized spectra are the centroids of the VP components. The VP model spectra (the fits) are shown as solid curves superimposed upon the data. Because the component velocities are tied together for all ions, ticks appear over spectral regions even where a VP column density is an upper limit.

In Table 3, we list the absorption redshifts, $z_{\rm abs}$, the kinematic spreads, ω_v, the rest–frame equivalent widths, $W_r(2796)$, and the MgII doublet ratios. We also list these quantities and the velocity, $\langle v \rangle$, for all kinematic subsystem, which are numbered as illustrated in Figure 1.

3.1. *Sample Properties*

In Figure 3*a*, we present the binned redshift distribution of our sample. The redshift range is $0.36 \leq z \leq 1.17$. The mean is $\langle z \rangle = 0.77$, with 43% of the systems between $0.4 \leq z \leq 0.7$ and 39% of the systems between $0.7 \leq z \leq 1.0$. In panel *b* of Figure 3, we show the cumula-

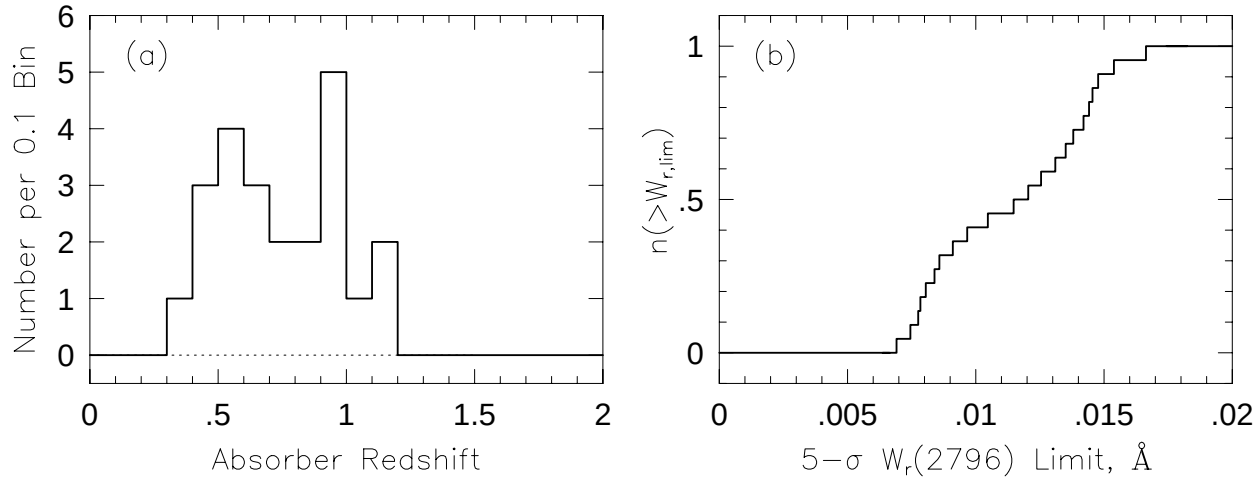

FIG. 3.— (a) The binned redshift distribution of our sample. — (b) The cumulative distribution of the 5 σ, rest–frame equivalent width detection threshold within a 1000 km s^{-1} range about MgII λ2796.

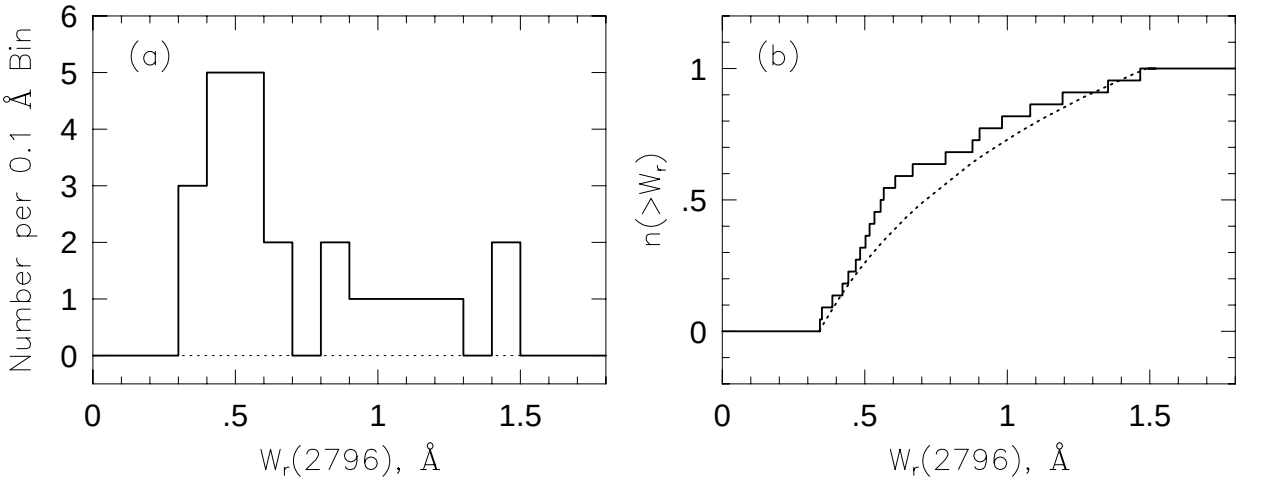

FIG. 4.— (a) The binned, rest–frame equivalent width distribution for MgII λ2796 of our sample. — (b) The cumulative distribution of our sample (histogram) compared to the distribution for an unbiased survey with the same equivalent width range as observed (dot–dot curve).

tive distribution of the 5 σ, rest–frame, MgII λ2796 equivalent width detection limit for the sample. More precisely, this illustrates the distribution of the detection sensitivity to very weak MgII absorption averaged over a 1000 km s^{-1} region ($\pm$500 km s^{-1}) about each absorber. The data are 100% complete to 0.017 Å and 80% to 0.014 Å. There is no sensitivity below 0.007 Å. That is, unresolved kinematic subsystems with $\log N(\mathrm{MgII}) \simeq 11.6$ cm^{-2} could be detected in *all* absorbers in the sample; below $\log N(\mathrm{MgII}) \simeq 11.2$ cm^{-2} there is no sensitivity.

The rest–frame equivalent width distribution for the sample is presented in Figure 4. In panel *a*, we show the binned distribution and in panel *b* we show the cumulative distribution. The dot–dot curve is the cumulative distribution of a "fair" sample (i.e. unbiased) over the same $W_r(2796)$ range for a power–law distribution function, $n(W_r) \propto W_r^{-\delta}$. Over the range $0.02 \leq W_r(2796) \leq 1.3$, the power–law exponent, δ, was shown to be 1.0 ± 0.1 (Churchill et al. 1999b). The steep rise to $W_r(2796) \simeq 0.6$ in the observed distribution, as compared to the "fair" distribution, indicates that the the sample is slightly "bottom heavy", having an overabundance of smaller equivalent width systems. However, a Kolmogorov–Smirnov (KS) test (Press et al. 1982) applied to the observed and "fair" cumulative distribution functions yields a KS statistic of 0.21 with significance 0.25. That the observed distribution is fair cannot be ruled out by the KS statistic; the sample apparently does not contained any significant bias with equivalent width.

Since we have a reasonably fair equivalent width distribution, we can contrast and compare inferences drawn from our moderate size sample to those drawn from the overall population, including behavior that is differential with $W_r(2796)$. To this end, we have divided our full sample into four subsamples based upon MgII absorption strength. In Table 4, we present the mean properties of these samples and the sample members. Sample A is the entire sample, which has $W_r(2796) \geq 0.3$ Å; sample B systems have $0.3 \leq W_r(2796) < 0.6$ Å; sample C systems have $0.6 \leq W_r(2796) < 1.0$ Å; sample D systems have $W_r(2796) \geq 0.6$ Å; and sample E, which is a subsample of

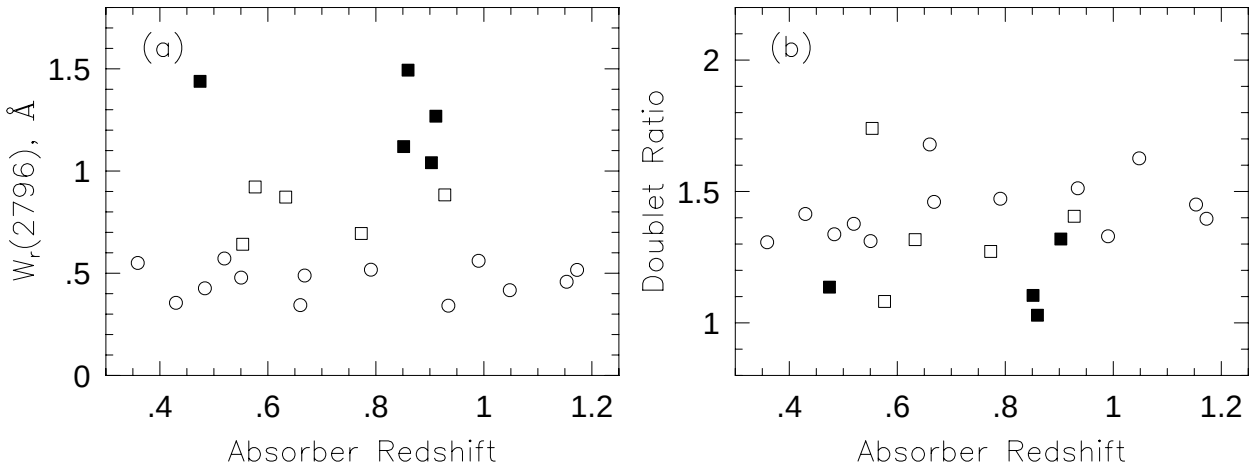

FIG. 5.— (a) The rest–frame, Mg II λ2796 equivalent width vs. absorber redshift. Open circles represent sample B ($0.3 \leq W_r(2796) < 0.6$ Å) and open boxes represent sample C ($0.6 \leq W_r(2796) < 1.0$ Å). sample E ($W_r(2796) \geq 1.0$ Å) is represented with filled boxes. — (b) The Mg II doublet ratio vs. absorber redshift. Data points are as defined in panel *a*. Measurement errors are given, on average, by the size of the data points for the data in both panels.

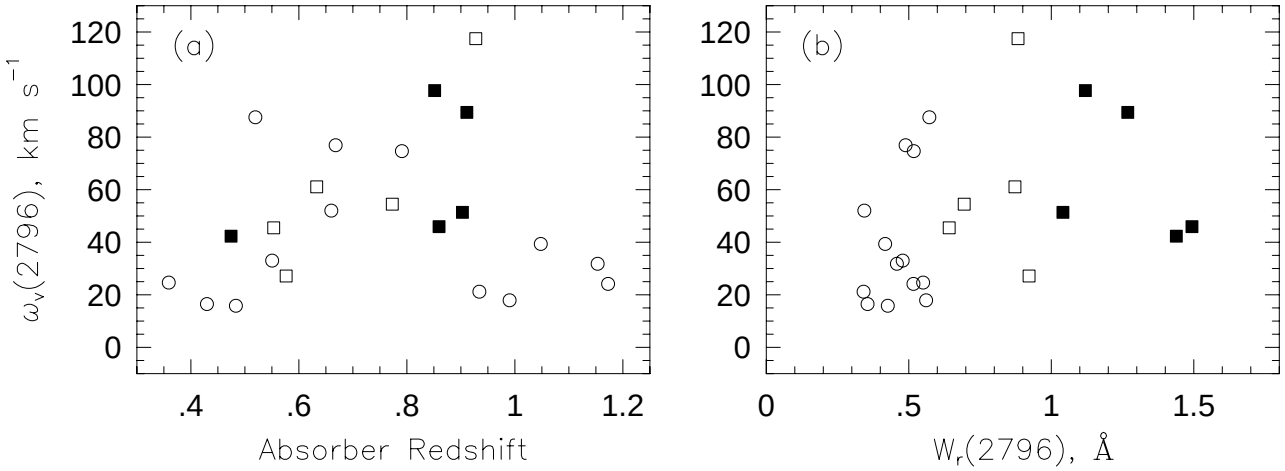

FIG. 6.— (a) The kinematic velocity spread of Mg II λ2796 vs. absorber redshift. Data points are as defined for Figure 5. — (b) The kinematic velocity spread of Mg II λ2796 vs. the rest–frame equivalent width of Mg II λ2796.

sample D, has $W_r(2796) \geq 1.0$ Å. These equivalent width ranges are chosen based upon historical precedent. SS92 have shown that each of these samples exhibits a different level of cosmological evolution (see § 1).

3.2. *Global Absorption Properties*

In Figures 5*a*–*b*, we present $W_r(2796)$ and the Mg II doublet ratio, DR, vs. absorber redshift. Sample B systems are plotted as open circles, sample C as open squares, and sample E as filled squares. Sample E is highly concentrated at $z \sim 0.9$, whereas sample B is fairly uniform over the covered redshift range. The mean DR is 1.36 and shows no trend with redshift. The system DR are really the flux weighted averages of the individual kinematic subsystems, which exhibit the full range of doublet ratios (not plotted); some weak subsystems are unresolved and somewhat saturated while some are optically thin. As listed in Table 4, there is a trend for DR to decrease from sample B to sample E.

In panel *a* of Figure 6, we present the full system kinematic spread, ω_v, vs. absorption redshift, where the data point types denote samples B, C, and E. Note that the kinematic spread of a system, as defined in Equation A5, is not the full velocity spread. For example, the full velocity spread of the $z = 0.9276$ system toward Q 1206 + 459 is $\Delta v \simeq 450$ km s^{-1}, whereas its kinematic spread is $\omega_v \simeq 120$ km s^{-1}. The kinematic spread provides an optical depth weighted velocity spread; it essentially is equivalent to the width of a Gaussian fitted to the complex, full system optical depth profile (i.e. it is column density weighted).

In panel *b* of Figure 6, we show the full system kinematic spread vs. $W_r(2796)$. Though a Spearman–Kendell test reveals a significant correlation, what is most telling is that there is a large scatter in the kinematic spread for each sample, B, C, and E; it is the mean of this scatter that is increasing with equivalent width.

In Table 5, we present the rest–frame equivalent widths for the transitions listed in Table 2. The velocity range of each kinematic subsystems is given, where the subsystem

number is as defined in Figure 1. The velocities are the limits of integration for Equation A3. The system totals are also listed. No entry for a given transition means that it was not covered.

In Table 6, we present the integrated column densities using the apparent optical depth method (Equation A7). Lower limits are provided when all transitions of a given ion were saturated within the subsystem. For MgI and FeII, upper limits are provided when the ion was not detected in any of its transitions. No entry means that no transitions were covered for the given ion.

In Table 7, we present the VP parameters from MINFIT. Following each component's velocity, we give the kinematic subsystem number; this allows the complexity of the subsystems to be examined. In the case of no detections, the column density is an upper limit. If there is no coverage of any transition for a given ion, the entry is left blank.

3.3. *Individual Systems*

3.3.1. Q 0002 + 051, UM 18 $z_{\rm abs} = 0.851394$

This system has a kinematically intriguing absorption profile, with a total velocity spread of roughly 475 km s^{-1}; it was fitted with a total of twelve VP components. Classified as a "double" systems by Churchill et al. (2000b), the overall MgII profile was found to have four kinematic subsystems. This is one of only two systems in our sample in which two subsystems (#1 and #2) have $W_r(2796) > 0.3$ Å. Furthermore, these subsystems are separated by 180 km s^{-1}. Subsystem #1 is fully saturated, exhibiting the kinematic spread and morphology characteristic of a DLA MgII profile [though it is not a DLA (Churchill et al. 2000b)]. But for its proximity in velocity to subsystem #1, subsystem #2 could be considered a system in its own right. Its large equivalent width and kinematic morphology are similar to those of Q 1101 − 264 at $z = 0.3590$, Q 1248+401 at $z = 0.7730$, and Q 1254+044 at $z = 0.9342$.

3.3.2. PG 0117 + 213 $z_{\rm abs} = 0.576398$

This DLA (Churchill et al. 2000b) exhibits fully saturated MgII profiles and a MgI profile with definite variations in strength in velocity space. There is a slight blending in the blue wing of MgI with the red wing of FeII λ2600 at $z_{\rm abs} = 0.7291$. The profiles were fitted with four VP components, though this fit is constrained only by the MgI profile. No FeII transitions were captured by the CCD.

3.3.3. PG 0117 + 213 $z_{\rm abs} = 1.047971$

This system has two kinematic subfeatures separated by roughly $v \sim 100$ km s^{-1}. Both exhibit blueward asymmetry and both have very weak MgI. The overall profile was fitted with seven VP components. This is a CIV–deficient system (Churchill et al. 2000b).

3.3.4. *Q* 0420 − 014 $z_{\rm abs} = 0.633004$

The overall profile is comprised of two kinematic subfeatures separated by $v \sim 200$ km s^{-1}. One of them is broad and complex. The red–most saturated components in subsystem #2 have MgI and FeII, whereas the bluer, more complex components do not. This suggests either strong variations in abundance patterns or in ionization/density conditions. A total of nine VP components were fitted.

3.3.5. PKS 0454 + 039 $z_{\rm abs} = 0.859565$

This DLA was studied by Steidel et al. (1995) and by Lu et al. (1996b) and Churchill et al. (2000a, b). The profile is a single fully saturated feature with a ~ 200 km s^{-1} spread. Though eleven VP components were fitted, the column densities and Doppler b values for components three through eight are not well constrained. In Table 7, formal errors are not provided for these components, only the approximate N and b values; any inferences regarding this system based upon the VP decomposition should be viewed with caution. Based upon the profile fit to the FeII λ2344 transition, there may be an offset in the continuum placement across that profile. There is a spurious, unidentified, weak feature at $v = +100$ km s^{-1} relative to MgII λ2803.

3.3.6. PKS 0454 + 039 $z_{\rm abs} = 1.153248$

This "classic" system (Churchill et al. 2000b) has the only profile in the sample that has weak, high–velocity absorption distributed *symmetrically* about the central main absorption region. However, there is confusion near both the MgII doublet transitions, in that weak, unidentified absorption features are seen. Additionally, there appears to be a weak, unidentified feature precisely where FeII λ2374 transition is predicted. This is apparent because of the unphysical strength ratios with respect to the other FeII transitions and is further suggested by another possible nearby unidentified feature. Very weak MgI is detected in the core of the strongest MgII component, but, again, there is a weak, unidentified feature within −50 km s^{-1}.

3.3.7. PKS 0454 − 220 $z_{\rm abs} = 0.474410$

Though not a DLA, based upon the definition $\log N({\rm HI}) \geq 20.3$ cm^{-2}, this system has been classified as "DLA/HI–Rich" by Churchill et al. (2000b). A total of eight VP components were fitted to this broad saturated profile. Though formal uncertainties are quoted in Table 7, it should be noted that the column density uncertainties in most central components are greater than a dex. Thus, inferences regarding this system based upon the VP parameters should be viewed with caution. There is possibly a weak component missed at $v = +80$ km s^{-1} in the wings of MgII; however, it was formally rejected by MINFIT. The FeII λ2344, 2374, and 2383 transitions were not captured by the CCD.

3.3.8. PKS 0454 − 220 $z_{\rm abs} = 0.483340$

This system is classified as CIV–deficient (Churchill et al. 2000b). There are no higher velocity kinematic subsystems; the absence of these subsystems is a common characteristic of CIV–deficient systems. The profile was fitted with a total of seven VP components, which were all well constrained in that they have small fractional errors. The strongest FeII and MgI components are aligned in velocity with the maximum MgII absorption.

3.3.9. PKS 0823 − 223 $z_{\rm abs} = 0.911017$

This systems is classified as a "double" (Churchill et al. 2000b). Unlike other double systems, this one exhibits

strong, complex absorption over most of the kinematic spread of ∼350 km s^{-1}. Most double systems are characterized by a single, large subsystem with a velocity spread less than 20 km s^{-1} and several weak, narrow, higher–velocity subsystems. The MgII λ2803 transition was captured only for subsystem #1. A total of 18 VP components were fitted to the system. The system is rich in FeII absorption in all subsystems. MgI, on the other hand, is unambiguously strong only in VP components four, five, and nine. From this, it can be inferred that there is a strong variation in the ionization conditions between the complex at $-50 \leq v \leq -90$ km s^{-1} and at $-10 \leq v \leq +30$ km s^{-1}, even though the FeII might suggest otherwise (unless there are abundance differences in the [α/Fe]).

3.3.10. Q 1101 − 264 $z_{\rm abs} = 0.359153$

The fully reduced and continuum normalized spectra studied in this work were kindly provided by Max Pettini. The observations were obtained with the UCL echelle spectrograph on the AAT, with the IPCS as the detector. The resolution is 6 km s^{-1} FWHM (or approximately 0.07–0.08 Å at the wavelengths covered here).

The MgII transitions lie in the Lyα forest of this line of sight, but there is no apparent contamination from HI. A fit to the profiles yields six VP components. Strong FeII λ2600 and MgI have been reported by Carswell et al. (1991), but are not presented here.

3.3.11. Q 1148 + 384 $z_{\rm abs} = 0.553362$

This system has a very interesting profile that is comprised of eight VP components in a single kinematic system spread over 200 km s^{-1}. The absorption strengths symmetrically decrease with increasing velocity, giving the overall profile a Gaussian "envelope" appearance. However, it is apparent that the FeII to MgII ratio is not symmetric; FeII is relatively stronger in the blue components of the system. The FeII λ2344, 2374, and 2383 transitions were not captured.

3.3.12. PG 1206 + 459 $z_{\rm abs} = 0.927602$

The kinematics and ionization conditions of this rich, complex system have been studied in detail by Churchill & Charlton (1999). It has been classified as a double systems (Churchill et al. 2000b). The overall system was fitted with twelve VP components over a total of five subsystems. FeII and MgII are present only in VP components eight, ten, and twelve in subsystem #5.

3.3.13. Q 1222 + 228 $z_{\rm abs} = 0.668052$

The profile is characterized by a central strong absorption and a "high–velocity" subsystem at $v \sim 230$ km s^{-1}. This weak subsystem, #2, has relatively strong FeII, and perhaps very weak MgI. Velocities less than -100 km s^{-1} were not observed for the MgII λ2796 transitions, but were for the λ2803 transition. There is no detectable absorption at those velocities. A total of five VP components were fitted to the main, stronger subsystem and a single component was fitted to the high–velocity subsystem. FeII exhibits fine velocity structure in subsystem #1.

3.3.14. PG 1241 + 176 $z_{\rm abs} = 0.550482$

The main MgII profile of this "classic" system (Churchill et al. 2000b) exhibits a redward subcomponent and a smooth blueward asymmetry that is suggestive of bulk motions with varying line–of–sight density rather than a blend of two VP components. The asymmetry is not significant in FeII and MgI, but may be present just below detection levels. There is a subsystem at $v \simeq +140$Å with no detected FeII or MgI. A total of four VP components was fitted to the system. The FeII λ 2344, 2374, and 2383 transitions were not captured by the CCD for the given HIRES configuration.

3.3.15. PG 1248 + 401 $z_{\rm abs} = 0.772953$

This system is classified as a "classic" (Churchill et al. 2000b). The MgII profiles exhibit the "double horn" shape that Lanzetta & Bowen (1992) derived for a smooth density, constant infall velocity kinematic halo model. The velocity separation of the two main absorbing regions is ∼ 50 km s^{-1}. The blue "horn" is comprised of three VP components due to the asymmetry in the overall profile. This central profile is quite similar to the Q 1101 − 264 system at $z_{\rm abs} = 0.3590$. At $v = +225$ km s^{-1}, there is an outlying high velocity optically thin subsystem. This outlier exhibits a small redward asymmetry. Several FeII transitions (λ2344, 2374, 2383, 2587, and 2600) have been detected. The high velocity subsystem is detected in the λ2600 transition, but is not detected to 5 σ in the other FeII transitions. A clear detection of MgI is also present in the high velocity system. Normally, these optically thin high velocity subsystems are not seen to exhibit neutral absorption (this is a rare occurrence).

3.3.16. Q 1254 + 044 $z_{\rm abs} = 0.519389$

The main subsystem in this absorber exhibits an asymmetry, like that in Q 1241 + 176 at $z = 0.5505$, suggestive of bulk motion and varying line–of–sight density. The absorption is stronger, however, such that the asymmetry is seen most strongly in the neutral gas as traced by MgI. This main feature has been fitted with three VP components and shows a typical rotating disk shape as can especially can be seen in the MgI transitions. There are two high velocity, optically thin single VP component subsystems at negative velocities, $v = -160$ and -360 km s^{-1}. Neither MgI nor FeII were detected in these two subsystems. The FeII λ2344, 2374, and 2383 transitions were not captured by the CCD.

3.3.17. Q 1254 + 044 $z_{\rm abs} = 0.934232$

The kinematics of this systems are very similar to those of Q 1248 + 401 at $z = 0.7730$ and also subsystem #2 of Q 0002+051 at $z = 0.8514$. Again, this is the classic "double horn" shape that Lanzetta & Bowen (1992) derived for a smooth density, constant infall velocity kinematic halo model. The velocity separation of the two main absorbing regions is ∼ 40 km s^{-1}. A total of two VP components, one modeling each of the "horns", were fitted to the profiles. The FeII is prominent only in one of the components. MgI is also present in this particular component, but is not detected in the other.

3.3.18. Q 1317 + 277, TON 153 $z_{\rm em} = 0.660051$

This CIV–deficient System (Churchill et al. 2000b) has a full velocity spread of ~ 150 km s^{-1} with a main subsystem that has a full width of ~ 50 km s^{-1} and an asymmetric profile shape. Three subsystems were found and a total of eight VP components were fitted. Subsystem #3 is the most complex of any subsystem at high velocities. Though fitted with three VP components, the profile is more suggestive of bulk motions. FeII has been detected in the main and next strongest subsystems only. Weak MgI absorption is detected in the component with the highest MgII column density.

3.3.19. Q 1421 + 331 $z = 0.902871$

This complex system shows rich variations in ionization, and/or chemical conditions as can be seen by the variations in FeII to MgII strengths across subsystems. The FeII profiles show a strong blueward asymmetry, with a complexity that suggest unresolved fine structure in the data. MgI absorption is seen only in subsystem #2 in the velocity region where MgII is most strongly saturated and exhibits a slight blueward asymmetry. The full profile was fitted with a total of ten VP components. There are two subsystems based upon the objective algorithm, though the profile is more suggestive of three. In the strongest subsystem, the FeII transitions reveal a "disk–like" profile, or the characteristic of organized motion with a density gradient along the line of sight.

3.3.20. Q 1421 + 331 $z_{\rm abs} = 1.172609$

The profile is quite symmetric, though it exhibits three strong centers of higher column density gas. This systems has no associated higher velocity subsystems. The complex MgII kinematics are seen in both MgI and FeII with remarkable little component to component variations. The full profile was fitted with a total of seven VP components.

3.3.21. PG 1634 + 706 $z_{\rm abs} = 0.990239$

The signal–to–noise ratio for this system is the highest in our sample for the MgII and MgI transitions. It is a single kinematic system with no moderate to high velocity subsystems to an equivalent width limit of 0.007 Å. This system is classified as CIV–deficient (Churchill et al. 2000b). The lack of higher velocity subsystems is characteristic of CIV–deficient systems. The total profile velocity spread is ~ 80 km s^{-1} and was fitted with five VP components. The FeII profiles exhibit the classic "double horn" shape, with an overall redward asymmetry.

3.3.22. PKS 2128 − 123, PHL 1598 $z_{\rm em} = 0.429735$

This system is also CIV–deficient (Churchill et al. 2000b), and typical of this class of MgII system, has no higher velocity subsystems. There is a "double–like" characteristic to the profiles. The system has been fitted with a total of four VP components. MgI is associated with all four MgII components and shows a redward asymmetry in the strongest two. Unfortunately, none of the FeII transitions reported by Tytler et al. (1987) and Petitjean & Bergeron (1990) were captured by the CCD,

3.3.23. PKS 2145 + 067 $z_{\rm abs} = 0.790777$

This "classic" system (Churchill et al. 2000b) has three subsystems, each having been fitted with two VP components. These subsystems are separated by ~ 90 km s^{-1}. Only subsystems #1 and #3 have detected FeII and none have detected MgI. The FeII λ2587 transition was not included in the analysis because it was positioned near the pen mark on the HIRES CCD.

4. DISCUSSION OF PROPERTIES

In order to investigate trends in the absorption properties with kinematics (i.e. velocities and kinematic spreads), we have divided the subsystems into three classes, the "low", "intermediate", and "high" velocity subsystems. Recall that the velocity zero points are set by the absorption redshifts, which are computed using Equation A1. There is a natural break in the subsystem velocity distribution at $v = 40$ km s^{-1}, so we divided the low and intermediate velocity classes at 40 km s^{-1} (note that there is only one subsystems with $20 \leq v \leq 40$ km s^{-1}; we conservatively chose 40 km s^{-1}). The median velocity of all subsystems with $v > 40$ km s^{-1} is 165 km s^{-1}, which is where we divided the intermediate and high velocity classes. For the following, we represent the low velocity class with open diamond data points, the intermediate class with open triangles, and the high velocity class with filled triangles.

4.1. *Kinematics*

In Figure 7*a* and *b*, we show subsystem MgII λ2796 equivalent widths vs. subsystem velocity and the subsystem kinematic spreads vs. subsystem velocities, respectively. A horizontal dot–dot line at $W_r(2796)$ Å indicates the sample minimum equivalent width cutoff for the full absorption systems. In general, MgII systems characteristically have a "dominant", optically thick absorbing subsystem. The majority of MgII absorbers have one to a few "intermediate" and "high" velocity subsystems.

The equivalent widths of the low velocity, dominant subsystems are $W_r(2796) < 1.0$ Å, with the majority ranging from $0.3 \leq W_r(2796) \leq 0.6$ Å. Their kinematic spreads typically range between $10 \leq \omega_v \leq 30$ km s^{-1}. The two systems in Figure 7*a* with $W_r(2796) \simeq 1.5$ Å and $\omega_v \simeq 50$ km s^{-1} are DLA/HI–Rich systems; neither of which have intermediate or high velocity subsystems [which may be a characteristic of lower redshift DLAs (Churchill et al. 2000b)].

The moderate and high velocity subsystems have $W_r(2796) \simeq 0.1$ Å and kinematic spreads less than 10 km s^{-1}. They contribute only 10–20% to the system total equivalent width. Out of 24, two have $W_r(2796) > 0.3$ Å (#2 in the $z = 0.9110$ system toward Q0823 − 223 and #2 in the $z = 0.8514$ system toward Q0002 + 051, respectively). They are contributing members in double systems (Churchill et al. 2000b).

There is a break in the velocity distribution at $v \sim 40$ km s^{-1}, which arises because the dominant subsystems, many of which exhibit complex kinematic structure, remove flux over a total velocity span of 30–40 km s^{-1}. The intermediate velocity subsystems have a mean kinematic spread of $\simeq 6.8$ km s^{-1} and those at high velocity have a mean of $\simeq 5.5$ km s^{-1}. The large majority

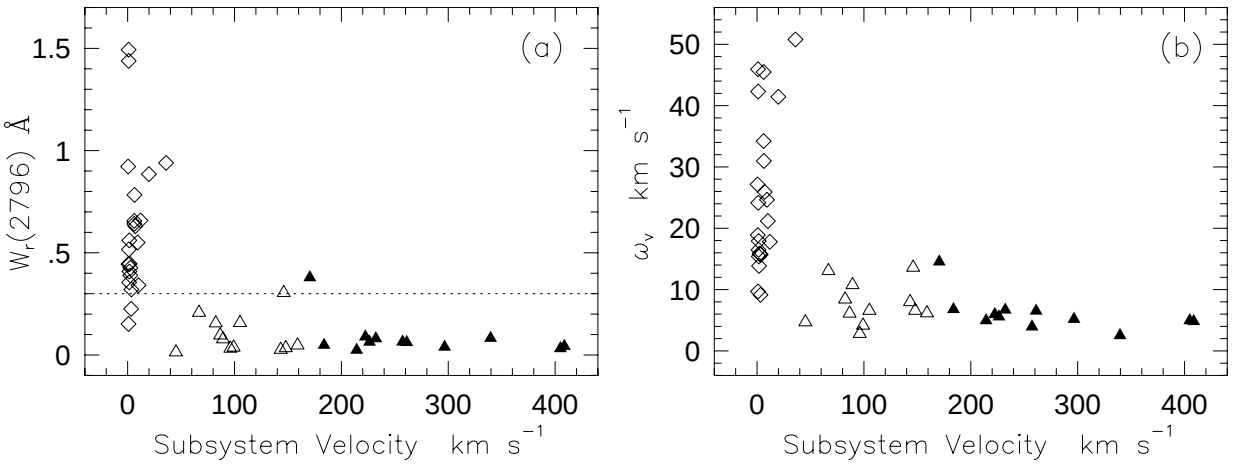

FIG. 7.— (a) MgII λ2796 subsystem equivalent width vs. subsystem velocity, $\langle v \rangle$. Diamonds represent subsystems with $\langle v \rangle \leq 40$ km s^{-1}, open triangles $40 < \langle v \rangle \leq 165$ km s^{-1}, and solid triangles $\langle v \rangle > 165$ km s^{-1}. — (b) Subsystem kinematic spread, ω_v, vs. subsystem velocity. Data types are the same as in panel (a).

of the high velocity subsystems are unresolved, whereas roughly half of the intermediate velocity subsystems are resolved. The anti–correlation between subsystem kinematic spread and velocity is significant at 3 σ. This implies that the high velocity subsystems have little to no bulk motions, whereas the moderate velocity subsystems exhibit a slightly broader range of bulk motions.

What is gleaned from Figures 7*a*–*b*, is that moderate redshift MgII systems have *characteristic kinematics*. They are *not* characterized by multiple "large" subsystems of comparable kinematic spreads and/or equivalent widths separated in velocity. They *are* characterized by a dominant subsystem with a kinematic spread of a few tens of km s^{-1} that is often accompanied by significantly smaller subsystems at relative velocities ranging from a few tens to a few hundreds of km s^{-1} and kinematics spreads of a few to several km s^{-1}. These facts suggest that the lines of sight through intermediate redshift MgII systems with $W_r(2796) > 0.3$ Å are picking out a dominant, relatively more massive structure with somewhat systematic kinematics of a few tens of km s^{-1}, often surrounded by smaller fragments of gas over a fairly large range of relative velocities.

4.2. *Equivalent Width Distribution*

The MgII equivalent widths of the intermediate and high velocity subsystems are similar in strength to those of the weak MgII systems (Churchill et al. 1999b). It is of interest, therefore, to explore if the physical nature of isolated weak systems is similar to those of the moderate and high velocity subsystems clustered within systems with $W_r(2796) \geq 0.3$ Å. The equivalent width distribution provides one means for comparison.

In Figure 8*a*, we plot the rest–frame equivalent width distribution for the intermediate and high velocity subsystems, those with $v > 40$ km s^{-1}. The data have been binned for purpose of presentation. The shaded region gives the equivalent width range over which the detection completeness drops from 100% to zero for unresolved absorption. Compared to a power–law distribution, there appears to be a turnover below $W_r(2796) \simeq 0.08$ Å, well above the region of partial completeness. The dotted line is a maximum likelihood power–law fit to $n(W_r) = CW_r^{-\delta}$ for $W_r > 0.08$ Å, which yielded $\delta = 1.6 \pm 0.7$.

Churchill et al. (1999b) showed that the equivalent width distribution of an unbiased sample of MgII systems follows a power law with $\delta = 1.0 \pm 0.1$ down to $W_r(2796) = 0.02$ Å. The number density of very small equivalent width systems in the "field" continues to increase as $W_r(2796)$ decreases well below 0.08 Å. In contrast, the MgII equivalent width distribution of intermediate and high velocity subsystems turns over below $W_r(2796) \simeq 0.08$ Å. It may be that both the shape and the slope of the equivalent width distribution differs between the population of weak systems and the intermediate and high velocity subsystems of "strong" systems.

Because of the large error in the slope fitted to the kinematic subsystems, however, we cannot discern if the two slopes differ significantly. The turnover below $W_r(2796) < 0.08$ Å, on the other hand, is unambiguous and represents a fundamental difference in the two distributions.

4.3. *AOD Column Densities*

In Figure 8*b*, we present the apparent optical depth (AOD) MgII column densities for the intermediate and high velocity subsystems vs. the subsystem velocity. The shaded region shows the range of column densities where the detection completeness drops from 100% to zero for unresolved absorption. The sample is 100% complete to $\log N(\mathrm{MgII}) = 11.6$ Å. The largest columns, $\log N(\mathrm{MgII}) \simeq 13$ cm^{-2} are primarily distributed among the intermediate velocity subsystems of the double systems (see Churchill et al. 2000b). The more typical column density is less than $\log N = 12.5$ cm^{-2}. As evident from the turnover in the equivalent width distribution (Figure 8*a*), there is a paucity of subsystems with $\log N \leq 12$ cm^{-2}, which is 0.4 dex above where the column density detection sensitivity begins to decline.

It could be argued that smaller column density subsystems are present but that they have very broad kinematic spreads and are therefore not detectable due to the noise in the data (i.e. they have been "removed" during

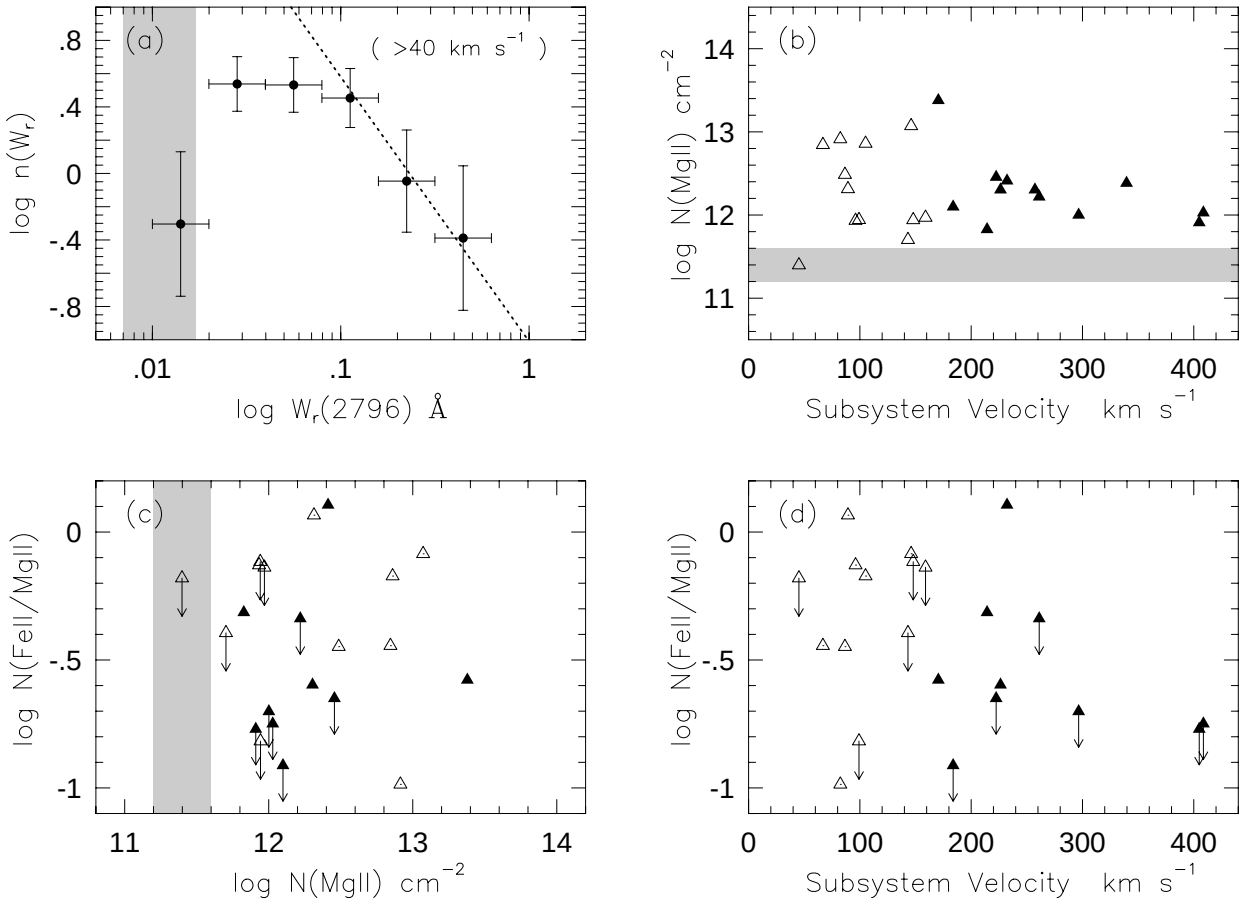

FIG. 8.— (a) The equivalent width distribution of moderate and high velocity kinematic subsystems (those with $\langle v \rangle > 40$ km s^{-1}). The shaded region gives the range where the detection sensitivity drops (partial completeness); below $W_r(2796) = 0.007$ Å there is no detection sensitivity (see Figure 3). The dot–dot line is a power law fit with slope of -1.6 (see text). — (b) Apparent optical depth column densities, $\log N$(MgII) vs. velocities, $\langle v \rangle$, of the kinematic subsystems. Data points types are same as for Figure 7. Typical errors in N(MgII) are 0.2 dex. — (c) Logarithmic ratio N(FeII)/N(MgII) vs. $\log N$(MgII) for moderate and high velocity kinematic subsystems. The shaded regions is the same as in (d) — Logarithmic ratio N(FeII)/N(MgII) vs. subsystem velocities.

the continuum fitting process). However, this argument is not supported by the data. The kinematic spreads of very small column density subsystems are tightly clustered about a small value (see Figure 7); if there were broader subsystems it would be expected that a range of kinematic spreads would be seen in the data. Otherwise, it would have to be argued that a bimodal distribution exists and that one mode has been systematically missed.

In Figures 8*c* and *d*, we show the logarithmic ratio of N(FeII)/N(MgII) vs. N(MgII) and vs. subsystem velocity, respectively. In the moderate and high velocity subsystems, the ratio N(FeII)/N(MgII) varies in the log from 0 to -1. It is fair to say that, over the range $12.2 \leq N(\mathrm{MgII}) \leq 13.4$ cm^{-2} observed in moderate and high velocity subsystems, the likelihood of finding $\log N(\mathrm{FeII})/N(\mathrm{MgII}) = 0$ is as likely as finding $\log N(\mathrm{FeII})/N(\mathrm{MgII}) = -0.5$. It is not clear if subsystems in this MgII column density range commonly have $\log N(\mathrm{FeII})/N(\mathrm{MgII}) = -1$, though one has been found. It does appear that subsystems with $N(\mathrm{MgII}) \leq 12.2$ cm^{-2} may often have $\log N(\mathrm{FeII})/N(\mathrm{MgII}) \sim -1$, though again, there is an exception to this possibility. If all this holds true, it may be that the highest velocity clouds, which have some of the smallest N(MgII), will have some of the smallest N(FeII) to N(MgII) ratios. The data in Figure 8*d* are somewhat suggestive of this trend. However, more systems would need to be analysed in order to make difinitive statements. It is interesting to speculate, however, that a trend in N(FeII)/N(MgII) with subsystem velocity might indicate a very real physical origin and evolution of the highest velocity subsystems.

In Figure 9, we present the apparent optical depth column densities of MgII [top panel], MgI [center panel], and FeII [bottom panel] for all subsystems in a given system. The systems, which are labeled across the top, are ordered by increasing $W_r(2796)$ from left to right. Sample membership is marked below the bottom panel. This ordering is to allow comparisons within and across samples. The shaded region in the top panel gives the range of detection thresholds of unresolved MgII features. Data point types denote velocity class (low, intermediate, and high). Upper and lower limits are shown with downward and upward pointing arrows, respectively.

From Figure 9, it can be seen how often and with what

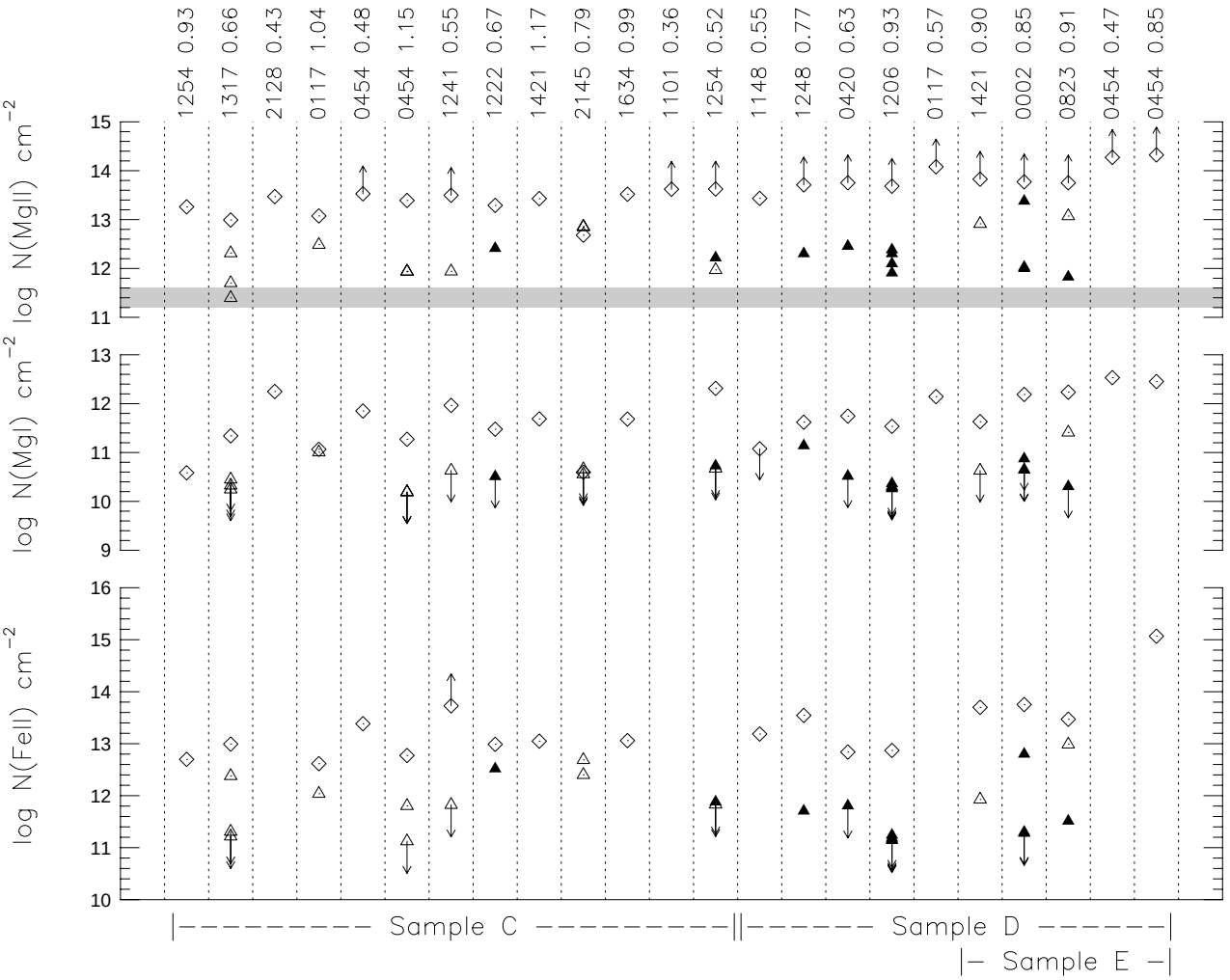

FIG. 9.— Apparent optical depth column densities of N(MgII) [top panel], N(MgI) [center panel], and N(FeII) [bottom panel] for each system. The systems are presented in increasing equivalent width order. Sample memberships are labeled along the bottom. Data points types are same as for Figure 7. Typical errors in N(MgII) are 0.2 dex. The shaded area gives the range of MgII column densities where the detection sensitivity drops from complete to none (for unresolved features).

strengths MgI and FeII are detected in intermediate and high velocity subsystems. An interesting contrast, for example, is seen between the high velocity subsystem in the $z = 0.7730$ system toward Q $1248 + 401$ and that in the $z = 0.6330$ system toward Q $0420 - 014$. Both have comparable MgII column densities, yet the $z = 0.7730$ system has a fairly large MgI column density, while the $z = 0.6330$ system has a restrictive upper limit. The FeII columns may also track this behavior.

4.4. *Kinematics and System Absorption Strength*

In Figure 10*a*–*b*, we show MgII λ2796 equivalent width of the full system vs. subsystem velocities and vs. the velocity spreads of the subsystems, respectively. As with Figures 5 and 6, open circles represent sample B, open boxes represent sample C, and filled boxes represent sample E. Horizontal dot–dot lines separate the samples.

The striking trend seen in Figure 10*a* is the relative paucity of high velocity ($v > 165$ km s^{-1}) subsystems in sample B. Though the demarcation between samples B and C at $W_r(2796) = 0.6$ Å is arbitrary (being based upon previous studies), there appears to be a trend with decreasing system equivalent width. Smaller equivalent width systems have fewer high velocity subsystems; most of their subsystems are at intermediate velocities.

In Figure 10*b*, the intermediate and high velocity subsystems occupy the left hand region ($\omega_v \leq 10$ km s^{-1}) of the diagram, whereas the low velocity, dominant subsystems are distributed over a broad range of kinematic spreads. Sample B systems have no dominant subsystems with ω_v greater than ~ 25 km s^{-1}, whereas all sample C and E systems have dominant subsystems with $\omega_v > 25$ km s^{-1}.

To investigate if these apparent kinematic trends are statistically significant, we computed the two–point velocity correlation function (TPCF) of the kinematic subsystems for samples B, C, D, and E. The TPCF is simply the frequency distribution of subsystem velocity splittings, $\Delta v_{ij} = |v_i - v_j|$ for $i \neq j$, where i and j represent any two subsystems in the sample.

In Figure 11, we present the cumulative distribution of

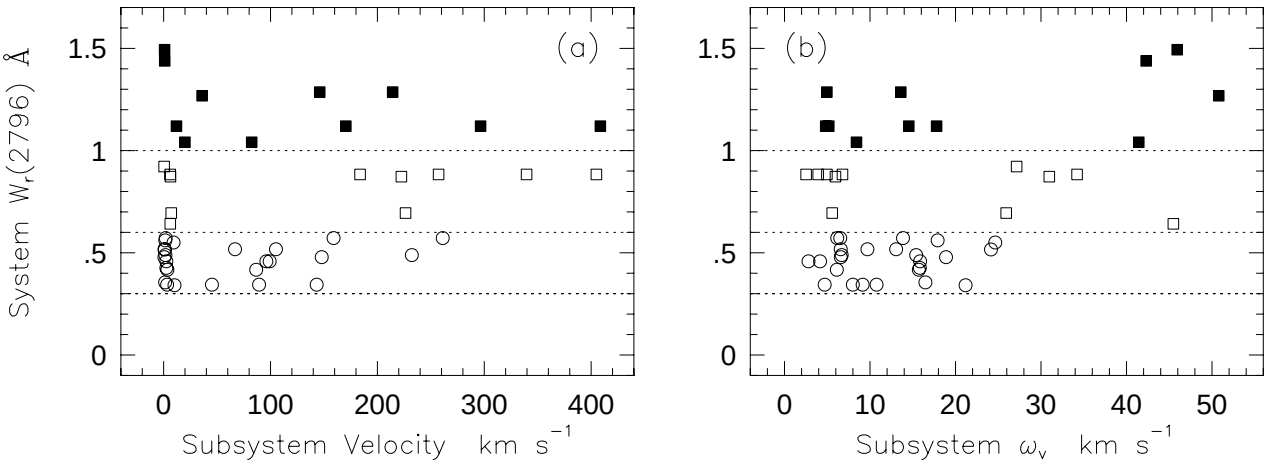

FIG. 10.— (a) Mg II λ2796 equivalent width of the full system vs. kinematic subsystem velocities. Open circles represent Sample B and open boxes represent Sample C. Sample E is represented with filled boxes. — (b) The same vs. kinematic velocity spread of the subsystems. Data types are the same as in panel (a).

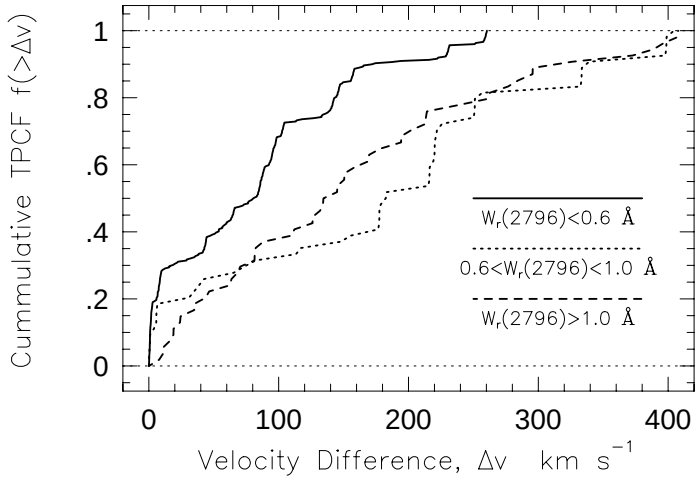

FIG. 11.— (a) The cumulative distribution of the velocity two–point correlation function for all subsystems. Three subsamples are shown, Sample B (solid curve), Sample C (dot–dot curve), and Sample E (dash–dot curve).

the TPCFs for sample B (solid curve), sample C (dot–dot curve), and sample E (dash–dash curve). Sample D, which is the union of samples C and E, is not plotted. There is a fast rise at very small velocity separations for samples B and C that is not present for sample E. This reflects the fact that dominant, low velocity subsystems in the largest equivalent width systems tend to have larger kinematic spreads, which suppresses small velocity separations. The smaller equivalent width systems in sample B do not have velocity pair separations greater than ~ 300 km s^{-1}, whereas *both* samples C and E have velocity pair separations as large as ~ 400 km s^{-1}.

Kolmogorov–Smirnov (KS) tests of sample B vs. samples, C, D, and E, yielded probabilities no greater than 10^{-5} that either sample C, D, or E exhibits the same TPCF as sample B. On the other hand, a KS test of sample C vs. sample E yielded a probability of 0.1; it cannot be ruled out that samples C and E have the same distribution of subsystem velocity splittings.

5. ON THE NATURE OF THE KINEMATIC SUBSYSTEMS

5.1. *Dominant Kinematic Subsystems*

Virtually all Mg II absorbers in our sample are characterized by a dominant, often saturated, kinematic subsystem. For sample B, the kinematic spreads, ω_v, of these dominant subsystems are no greater than 25 km s^{-1}. It is rare for there to be a second kinematic subsystem with comparable kinematic spread and equivalent width (the $z = 0.79$ system toward PKS 2145 + 064 is an exception).

As reported by Steidel, Dickinson, & Persson (1994) and by Steidel (1995), there appears to always be a normal, bright galaxy within $\sim 40h^{-1}$ kpc (sky projected) of the absorbing gas. Furthermore, the physical extent of the absorbing gas was shown to have near–unity covering factor and to be related to the galaxy K luminosity, such that $R(L_K) \simeq 40h^{-1}(L_K/L_K^*)^{0.15}$ kpc. These results further support the scenario in which absorbing gas is associated, in some way, with the total mass (number of stars) in a "host" galaxy, or that there is a strong link between the

host galaxy mass and the extended gaseous environment in which the galaxy is evolving (also see Churchill et al. 1996). Since virtually the entire MgII equivalent width in a given absorber arises from the dominant kinematic subsystem, it has been these subsystems alone that are governing the statistics of absorber–galaxy associations.

There is an observed one–to–one correspondence between optically thick HI and MgII systems with $W_r(2796) > 0.3$ Å and a one–to–one correspondence between optically thin HI and weak systems with $W_r(2796) \leq 0.2$ Å (Churchill et al. 2000a)[6]. This would suggest that the moderate and high velocity kinematic subsystems are optically thin in HI, that the optically thick HI arises in one or a few of the subcomponents in the dominant kinematic subsystem. Photoionization models (Cloudy; Ferland 1996) are consistent with this statement (Churchill et al. 1999b; Churchill & Charlton 1999).

The narrow kinematic spreads and larger HI column densities of the dominant subsystems, would suggest that dominant subsystems arise in higher density structures with some level of systematic kinematics. An unresolved issue is whether the *optically thick* absorbing gas is distributed quasi–uniformly (giving rise to the unity covering factor) in an extended, "spherical" halo (Lanzetta & Bowen 1990; Bergeron & Boissé 1991; Steidel 1993; Steidel 1995; Steidel et al. 1997), or in a more flattened, "disk" geometry (Bowen et al. 1995; Charlton & Churchill 1996; Charlton & Churchill 1998). Absorption line models using random lines of sight through extended disk structures, with flat rotation curves and reasonable vertical velocity dispersions, naturally explain the characteristic properties of the dominant subsystems (Charlton & Churchill 1998).

This by no means renders the "disk model" a unique interpretation of the strongest subsystems in complex absorption line data. However, any simple interpretation must explain the ubiquity and narrow kinematic range of the dominant subsystems. If galaxy disks are not a significant contribution to the absorption, then we are required to suggest a more complex scenario; spatial and kinematic distributions of the absorbing gas, from galaxy to galaxy, would be required to conspire such as to virtually always give rise to a *single* optically thick subsystems with a kinematic spread less than ~ 25 km s^{-1} and still yield a unity covering factor, statistically. As such, the presence and properties of dominant subsystems in MgII systems are important constraints for models of absorbers.

5.2. *Moderate and High Velocity Kinematic Subsystems*

There is no direct evidence whether or not the small $W_r(2796)$, moderate to high velocity subsystems are components in the same spatial distribution around galaxies as the dominant subsystems (i.e. reside within $R(L_K)$ or reside at larger galactocentric distances). As such, inferring their nature and their relationship to the dominant kinematic subsystem is difficult. However, there are some clues to be drawn from the data, which we discuss below.

5.2.1. *Comparison with Galactic HVCs*

The physical locations, sizes, metallicities, and kinematics of Galactic high velocity clouds (HVCs; e.g. Wakker & van Woerden 1997) are currently a matter of debate (e.g. Blitz et al. 1999; Braun & Burton 1999; Charlton, Churchill, & Rigby 2000; also see the series of articles in Hibbard, Rupen, & van Gorkom 2000). It is clear that *some* HVCs are associated with the Galaxy in that they are within a few kiloparsecs and/or are members of large complexes that appear to lie along great circles on the sky. What is not definitive, however, is whether some HVCs are remnants of galaxy group formation and whether or not they are spatially and kinematically distributed throughout the Local Group consistent with material inflowing from the intersection of intergalactic filaments, where multiple galaxies form (e.g. Zhang et al. 1997). Note, however, that the results of Zwaan & Briggs (1999) and Charlton et al. (2000) have placed strong constraints limiting the parameter space of group formation models.

HVCs, including the compact HVCs (Braun & Burton 1999), are detected in HI 21–cm emission, for which the present sensitivity is typically a few $\times 10^{18}$ atoms cm^{-2}; they are optically thick in HI and would give rise to Lyman limit breaks if detected in absorption. Photoionization modeling [using Cloudy (Ferland 1996)] has revealed that MgII absorption with $W_r(2796) \sim 0.1$ Å arises in optically thin HI gas, i.e. $N(\mathrm{HI}) \leq 10^{17.3}$ cm^{-2}, over four decades of ionization parameter[7] for metallicities greater than 0.01 $Z_\odot$ (see Figures 11 & 12 of Churchill et al. 1999b). Detailed modeling of the $z = 0.93$ system toward PKS $1206+459$ has revealed that the moderate and high velocity subsystems in that absorber are tightly constrained to be low ionization, sub–Lyman limit, pockets of gas with relatively high metallicities, i.e. $Z \geq 0.1$ $Z_\odot$ (Churchill & Charlton 1999). These "clouds", which have inferred masses and sizes of $\sim$ few $\times 10$ M$_\odot$ and $\sim$ few $\times 10 - 100$ pc, respectively, are aligned in velocity with highly ionized material (i.e. CIV, NV, and OVI) that arises in a separate gas phase. This multiphase ionization structure is present in most all MgII absorbers having moderate and high velocity subsystems (Churchill et al. 2000b).

Though the ionization structure and metallicities of HVCs are not well known, a comparison of the HI column densities and the inferred masses and sizes of moderate and high velocity subsystems reveals that they very probably are not higher redshift analogues to Galactic HVCs. Because of the large disparity in the HI column densities, this holds independent of whether HVCs are closely associated with galaxies, remnants of group formation, or both.

5.2.2. *Comparison with Weak Systems*

The population of weak MgII systems (Churchill et al. 1999b) has a range of equivalent widths, line widths, and doublet ratios similar to those of the intermediate and high velocity subsystems. As mentioned above, the kinematic subsystems are optically thin in HI, have small masses and sizes, and are aligned in velocity with higher ionization gas in a separate phase. Rigby et al. (2000) have shown that most single–cloud weak systems are also aligned in velocity with a separate high ionization gas phase and that the HI is optically thin. Furthermore, the masses,

[6]We caution that the sample size is small, ~ 15.

[7]The ionization parameter is the ratio of the number density of hydrogen ionizing photons to that of hydrogen.

sizes, and metallicities of many weak systems are similar to the kinematic subsystems, being $\sim$ few $\times$ 10 $M_\odot$ and $\sim$ few $\times$ 10 $-$ 100 pc, respectively (Churchill & Charlton 1999; Rigby et al. 2000).

At face value, these considerations would suggest that the origins, sizes, lifetimes, and chemical and ionization conditions of small $W_r(2796)$ subsystems and of single–cloud weak systems are governed by similar physical processes, even if the environments in which they arise are quite varied. However, as shown in Figure 8 and discussed in § 4, there is a clear drop in the number of moderate and high velocity subsystems with $W_r(2796) < 0.08$ Å, whereas no such decrease is seen for the weak systems down to $W_r(2796) = 0.02$ Å (Churchill et al. 1999b). Therefore, for the weakest subsystems, the governing physical processes must diverge from those of the weakest weak systems.

It is reasonable to explore the possibility that the putative different processes are induced by environment, such as the mass of the potential well (galactic environment) or the distance of the absorbing gas from the potential center. The kinematic subsystems are known to be associated with bright, galaxies with a range of mass, including those with $L_K \sim$ few $\times L_K^*$. Though the impact parameters are $\sim$ 40 kpc or less, the actual galactocentric distances of these weak subsystems are not known. On the other hand, the majority of MgII absorbers selected by $W_r(2796) < 0.3$ Å do *not* have $L_K \geq 0.05 L_K^*$ galaxies within $\sim$ 40 kpc (Churchill et al. 1999b); they are either further out in similar halos or are associated with the small halos of dwarf galaxies with $L_K \leq 0.05 L_K^*$.

Consider photoionized absorbing, cool–phase gas clouds that are pressure confined in hot, virialized gaseous galactic halos with $T_h \sim V_{200}^2 \times 10^6$ K, where V_{200} is the halo circular speed in units of 200 km s^{-1} (proportional to the total mass within the virial radius). The dominant destruction methods would include Rayleigh–Taylor instability, cloud–cloud collisions, Kelvin–Helmoltz instability, and evaporation or condensation (e.g. Mo & Miralda–Escudé 1996). The time scales for these are dependent upon various combinations of the "cloud" masses, M_{cl}, sizes, r_{cl}, densities, n_{cl}, and temperatures, T_{cl}, and upon the virialized halo temperature, T_h, density, n_h, and pressure, P_h, the latter two being functions of distance out in the halo, R. For the following, we will assume that $W_r(2796)$ is a rough indicator of cloud size, r_{cl}.

Rayleigh–Taylor instability sets in when the drag force (ram pressure) on a cloud exceeds the surface self–gravitational force (surface tension). For a cloud of fixed mass, the velocity at which instability sets in varies as $(n_{cl}/n_h)^{1/2} V_{200}^{-3/2} (M_{cl}/r_{cl})$, where n_h scales as R^{-1} and n_{cl} scales with slightly less sensitivity, resulting in a very weak anti–proportionality with R. Smaller clouds are much favored in lower mass halos with little dependence upon galactocentric distance.

The time scale for cloud–cloud collisions depends upon the cloud covering factor, f_c, and scales as $f_c^{-1} R V_{200}^{-1}$. For fixed f_c, the destruction rate of clouds by collisions decreases at large galactocentric distances and is smaller in lower mass halos. If f_c decreases with increasing R, the time scale increases with galactocentric distance more rapidly than to the first power.

Pressure confined clouds moving at the sound speed in an external medium are destroyed by Kelvin–Helmholtz (hydrodynamic) instability on the order of the cloud dynamical time, which scales as $r_{cl} T_{cl}^{1/2}$ (Murray et al. 1993). Clouds with lower densities and smaller sizes are most likely to be destroyed by heat conduction (evaporation) on a time scale very sensitive to the mass of the virialized halo. The evaporation time scales as $M_{cl} r_{cl}^{-1} V_{200}^{-5}$ (Cowie & McKee 1977). Mo & Miralda–Escudé (1996) have suggested that, in cases where the cloud covering factor approaches unity, cloud creation should balance cloud disruption and evaporation. In such a scenario, the minimum cloud mass in this equilibrium process will be smaller in environments where the destruction time scales are longer for small clouds, which occurs in smaller mass halos.

The upshot is that each cloud destruction mechanism favors longer lifetimes for small clouds in smaller mass halos and at large galactocentric distances. This by no means explains the differences in the equivalent width distribution of moderate and high velocity subsystems and weak systems for small $W_r(2796)$. However, it is suggestive that small $W_r(2796)$ clouds are less favored in larger mass halos. Of course, this assumes the ionization conditions and/or metallicities do not systematically vary between weak systems and weak subsystems. As stated above, current evidence is that they do not.

6. PROFILE ASYMMETRIES AND KINEMATICS

One clue to the nature of the moderate and high velocity subsystems may be the kinematic asymmetries of the overall MgII profiles; *in virtually every system with multiple subsystems, those with moderate and high velocity are either all blueshifted or all redshifted with respect to the dominant subsystem.* This phenomenon would naturally arise if moderate and high velocity subsystems are small components in a *systematic distribution* of gas (both spatially and kinematically) that is offset relative to the dominant subsystem, even if this structure extends well beyond $R(L_K)$. Examples are small clouds within a Magellanic Stream–like structure (which does not have a unity covering factor around the Galactic halo), or between the large column density, HI bridges flowing between M81 and its satellite galaxies (Yun, Ho, & Lo 1994). The systematic asymmetries would not *typically* arise, however, from absorbing gas with both unity covering factor and a random spatial and kinematic distribution with respect to the dominant kinematic subsystem.

To illustrate a possible spatial–kinematic relationship between the dominant subsystem and weak, moderate to high velocity subsystems, we examine a simplistic model of an edge–on rotating disk and a spherical infalling halo. We use the probability distribution functions, $\Phi(v)$, for intercepting an absorbing component ("cloud") at a given line of sight velocity through the disk and halo derived by Lanzetta & Bowen (1992; see their Equations 1–5 and Figures 9–11). This model assumes an r^{-2} spatial density profile for the absorbing components.

We have normalized these probability distributions such that $\int_{-\infty}^{\infty} \Phi(v) dv = N_{tot}$, where N_{tot} is the integrated MgII column density of the line of sight passing through the model structure. Using this normalization, one can interpret $\Phi(v)dv$ as $N(v)dv$, the probable column density per unit velocity in the velocity interval v to $v + dv$.

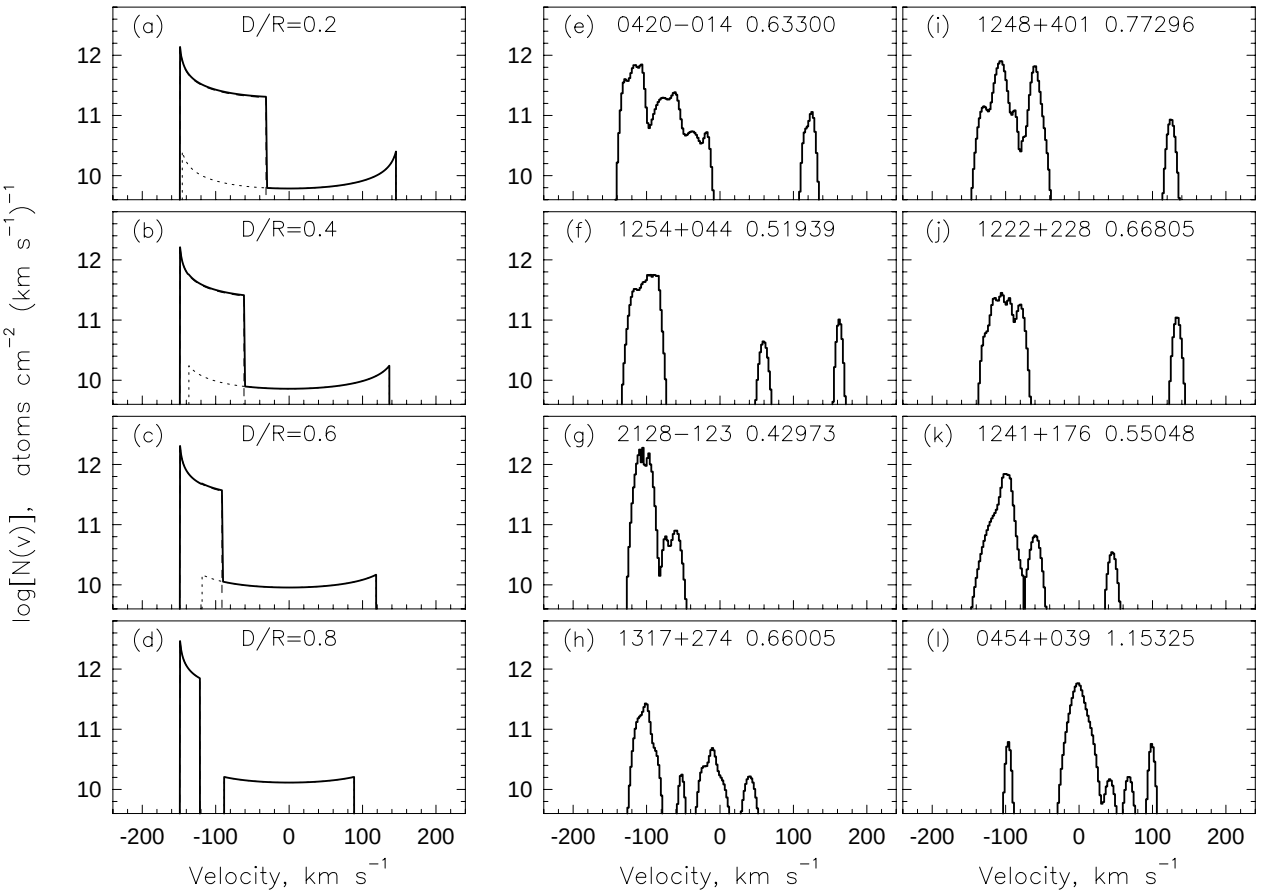

FIG. 12.— (a–d) The logarithm of the column density probability distribution per unit velocity, $N(v)$ based upon simple disk/halo models. The impact parameter, D, is given in units of the absorber radius, R, as labeled in each panel. The dot–dot curve represents absorption from the halo and the dash–dash curve from the disk. The solid curve is the total column density probability at each velocity. The $N(v)$ have been normalized to $\log N(\mathrm{Mg\,II}) = 13.6$ cm^{-2} for the disk component and $\log N(\mathrm{Mg\,II}) = 12.3$ cm^{-2} for the halo component. — (e–l) The logarithm apparent column densities (Equation A6) for eight of the absorbers in the sample. The velocities zero points and the signs of the velocities have been adjusted arbitrarily to better match the probability distributions for display purposes.

We normalize the disk component to the average Mg II column densities (Equation A7) of the dominant subsystems and the halo component to that of the moderate and high velocity subsystems (sample B). These are $\log N_{tot} = 13.6$ cm^{-2} for the disk and 12.3 cm^{-2} for the halo, respectively.

In Figure 12*a–d*, we show the logarithm probable column density velocity distribution for a combined halo/disk structure with $v = 0$ km s^{-1} set to the disk/halo systemic velocity. The disk rotation and halo infall velocities are set to $w_0 = 150$ km s^{-1}, typical of a sub–L^* galaxy. The sense of the disk rotation is chosen toward the line of sight. Each panel illustrates $\log N(v)$ for the ratio of the impact parameter, D, to the size of the absorbing structure, R (the model geometry is illustrated in Figure 9 of Lanzetta & Bowen). The dot–dot curve is the halo absorption and the dash–dash curve is the disk absorption. The solid curve is the combined absorption.

The most salient feature of this model is that the disk absorption is systematically offset from the halo absorption for all impact parameters; the model consistently predicts asymmetric profiles. The peak predicted column density per unit velocity from the disk is always larger than that predicted from the halo. This is governed by the normalization, which is tuned to the data. As impact parameter is increased, the kinematic spreads of both the disk and halo components decrease. For $D/R > 0.7$, the disk absorption and halo absorption no longer overlap in velocity space.

In Figure 12*e–l*, we show Mg II apparent optical depth column density profiles, $\log N_a(v)$, for eight of the systems in our sample that show strong asymmetries (computed from Equation A6). These profiles are generated by inverting the smooth Voigt profile models for display purposes. The Mg II λ2803 transition is used because it is often not as saturated in the strong line cores[8]. The velocity zero points and the sign of the velocities have been adjusted to ease visual comparison with the model distributions.

Qualitatively, the observed profiles are remarkably sim-

[8]Saturation results in a lower limit for in the $N_a(v)$ profiles. The exact limit is dependent upon the uncertainty in the flux values in the line core. At very high signal–to–noise ratio, the limit is determined by the read noise.

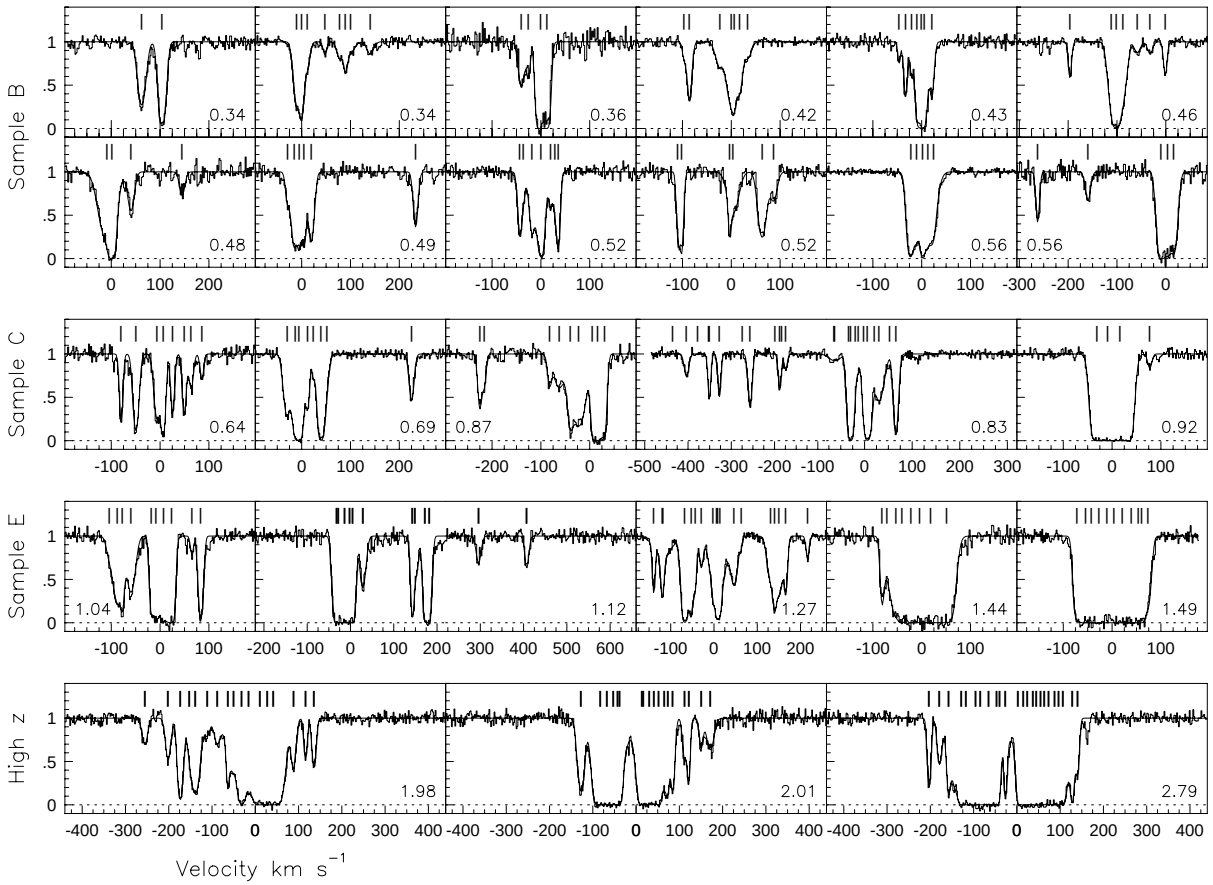

FIG. 13.— A gallery of Mg II λ2796 profiles as a function of rest–frame velocity. The profiles are separated into subsamples (B, C, and E) and ordered by increasing equivalent width. The rest–frame equivalent widths are labeled in the lower corners of each subpanel.

ilar to those predicted by the simple models of discreet absorbing components in a disk/halo absorbing structure. The disk absorption could be interpreted to represent the probability distribution of the dominant kinematic subsystem and the halo absorption to represent the probability distribution of the weak, intermediate to high velocity subsystems.

Such an interpretation is consistent with the observed kinematic asymmetries *and* provides a prediction of what parts of galaxies give rise to the observed kinematic subsystems. That is, many of the observed profile velocity asymmetries may be governed by the passage of the line of sight through a rotating disk. This structure would give rise to a dominant kinematic subsystems offset in velocity from the systemic velocity. Its covering factor must be near unity in order to account for the ubiquity of absorption features with velocity spreads on the order of the disk component of the models. The weak subsystems at intermediate to high velocities would then arise in the "halo" structure comprised of smaller absorbing clouds. This structure would have a somewhat broader, symmetric distribution of velocities. Statistically, this "halo" structure would have a covering factor near unity, based upon 24 moderate to high velocity subsystems observed in 23 systems. However, only 13 systems actually have these subsystems.

If disks play a role in governing the kinematics of Mg II absorbers, the disk orientation is going to give rise to variations in location of the disk component of the model velocity distribution (recall, those presented are for edge–on disks only). In the case of face–on orientations, the velocity width of the disk component will be proportional to the velocity dispersion of the gas perpendicular to the disk (see Charlton & Churchill 1998). The disk systemic velocity will be centered at $\sim v = 0$ km s^{-1} with the velocities of any "halo" structure distributed symmetrically. In Figure 12*l*, we present a possible example of the kinematics expected from a face–on disk orientation.

This absorber is the only one with weak subsystems to *both* sides of the the dominant subsystem. At $z = 1.15325$ toward PKS 0454 + 039 (Figure 2*f*), the candidate absorber is difficult to resolve in an WFPC2/*HST* image from the *HST* archive (also see Le Brun et al. 1997). However, there is an example of a $D = 13.2$ kpc, face–on, disk galaxy (see Figure 1 in Churchill 2000) associated with the $z = 0.55336$ absorber toward Q 1148+384 (Figure 2*k*) that has a central dominant absorption component. Though this system technically is a single kinematic subsystem, several clouds are present whose column densities decrease as subsystem velocity separations from the central component increase. Overall, however, profiles in which the weaker, and/or moderate to high velocity subsystems are distributed symmetrically about the dominant subsystem

are rare in our sample.

7. WHAT IS EVOLVING?

The differential evolution in the Mg II equivalent width distribution has been determined by measuring the redshift path density, dN/dz, for samples with different minimum equivalent widths (see SS92). Absorbers with $W_r(2796) > 0.3$ Å exhibit no cosmological evolution. However, as the minimum $W_r(2796)$ is increased, both the mean redshift of the sample and the rate of evolution (slope of the redshift path density) increase, indicating that the strongest systems evolve away with cosmic time and that the largest systems evolve the most rapidly.

Though we have quantified the Mg II absorption properties from the profiles, we point out that qualitative visual inspection can be more revealing than parameterized representations, especially for the profile "shapes", or kinematic morphologies. We have divided our data into samples B, C, and E using the same minimum equivalent width cut offs employed by SS92, i.e. greater than 0.3, 0.6, and 1.0 Å, respectively. In the upper three panels of Figure 13, we illustrate the Mg II λ2796 profiles in increasing equivalent width order, with the data separated into these three samples. The profiles are presented in rest–frame velocity with the flux normalized and VP models superimposed, including ticks that indicate the number of VP components and their velocities. In the lower corner of each subpanel, the equivalent width is given in angstroms.

The mean kinematic spread of the *dominant subsystems* increases along the sequence from sample B to C to E. This is not surprising, given that the dominant subsystems of larger equivalent width systems are often saturated over a fair fraction of their velocity range. This is reflected in the trend for the largest $W_r(2796)$ systems to have only lower limits on the integrated apparent column densities of their dominant subsystems (see Figure 9). Thus, the equivalent width is directly proportional to the velocity width of the dominant subsystems, which would not hold true if the moderate and high velocity subsystems were often saturated. This could imply, then, that the differential evolution in the equivalent width distribution is primarily due to kinematic evolution (decrease in velocity spread) of the dominant subsystems. However, this is not a unique interpretation.

In the bottom panel of Figure 13, we present examples of higher redshift systems as representatives of the very largest $W_r(2796)$ absorbers[9]. Each has an equivalent width consistent with or greater than 2.0 Å and a redshift greater than $z = 1.3$. If these profiles are representative at higher redshift, then they indicate that large, "double" optically thick subsystems are characteristic of systems that evolve away most rapidly. It has been shown, as one interpretation, that the Mg II evolution rate is consistent with the evolution of galaxy pairs (Churchill et al. 2000b), assuming that each saturated region of the Mg II profiles arise from a separate galaxy,

However, and this cannot be addressed by the current data, there is the question of whether the weak, moderate and high velocity subsystems are vestiges of what is evolving. If they are, then the disappearance of multiple, optically thick subsystems, like those shown in Figure 13, could be explained as either ionization or structure evolution into the weak, moderate and high velocity subsystems. Incorporating knowledge of the profile asymmetries discussed in § 6, this would imply that the Mg II evolution is kinematically asymmetric. In the disk/halo scenario outlined above for connecting galaxy structure to the profile asymmetries, such evolution would imply a reduction in the number of "halo" absorbing components, or clouds.

8. CONCLUSION

We have presented the Mg II $\lambda\lambda$2796, 2803 absorption profiles, resolved at $\simeq 6$ km s^{-1} with HIRES/Keck I, for 23 quasar absorption line systems having $W_r(2796) > 0.3$ Å. We have also presented Fe II, and Mg I profiles when the transitions were detected. The overall absorption properties of many of these systems have been previously investigated (Churchill et al. 2000a).

The complex kinematics were parameterized by defining "kinematic subsystems" and by Voigt profile fitting. We have discussed the absorber properties, including the distributions of equivalent widths, subsystem to subsystem column densities, and velocity separations (see § 4). A companion paper (Churchill, Vogt, & Charlton 2000) will present analysis of the Voigt profile results. The data were divided into three samples by equivalent width range. We found that there are systematic differences, or trends, in the kinematics with increasing equivalent width, and that this may provide clues to the observed differential evolution in the equivalent width distribution of Mg II absorbers (e.g. SS92).

The properties of the "moderate" and "high" velocity kinematic subsystems have been compared to those of the Galactic high velocity clouds (HVCs) and to those of the population of single "cloud" weak systems. We have inferred that the moderate and high velocity subsystems are not higher redshift analogues to HVCs primarily because of the low H I column densities in the former. Though the subsystems and weak systems are comparable in their inferred sizes, metallicities, and ionization conditions, the turnover in the subsystem equivalent width distribution at $W_r(2796) \sim 0.08$ Å would indicate that they reside in different environments. We discussed the time scales for cloud destruction and point out that the smallest clouds are most favored to survive in the smallest mass halos and at the largest galactocentric distances.

Direct knowledge of the kinematic evolution of Mg II absorbers will require an unbiased, higher redshift data set with HIRES/Keck resolution. It is likely that a clear understanding will require charting the kinematics of the higher ionization phases (as seen in C IV absorption, for example) in order to understand the multiphase structure of the gas. It is in the relative kinematics of these ionization phases that the energetics and gas phase structure can be employed to infer the actual mechanisms (i.e. star formation, pair evolution, intergalactic medium infall, chemical enrichment, etc.) that drive the differential evolution in the Mg II equivalent width distribution.

Support for this work was provided by the NSF (AST–9617185), and NASA (NAG 5–6399), California Space Institute (CS–194), and a Sigma–Xi Grants in Aid of Re-

[9]These systems are part of a complementary, targeted survey of the higher redshift, very largest equivalent width Mg II absorbers.

search. We thank M. Keane for assistance with July 1994 observations and discussions very early in the project. We have enjoyed and learned from countless discussions during the course of this work, most notably with J. Bergeron, M. Bolte, J. Charlton, M. Dickinson, F. Drake, S. Faber, R. Guhathakurta, R. Ganguly, J. Hibbard, B. Jannuzi, E. Jenkins, M. Keane, K. Lanzetta, L. Lu, P. Petitjean, M. Pettini, J. Rigby, J. Rachen, M. Rauch, W. Sargent, B. Savage, D. Schneider, K. Sembach, G. Smith, C. Steidel, F. Timmes, D. York, and D. Zaritsky. We thank J. Charlton for reading and commenting on the draft of this manuscript.

APPENDIX

FORMALISM OF MEASURED QUANTITIES

Here, we outline the mathematical formalism for measuring absorption properties directly from the data themselves. We computed these quantities and their measurement errors (uncertainties) for both the overall systems and each of their kinematic subsystems. The computational formalism, including careful treatment of the uncertainties, has been presented in detail in the appendices of Sembach & Savage (1992) and in Churchill (1997), where a few corrections to the Sembach & Savage derivations have been noted.

Systemic Redshifts

The systemic redshift of each absorbing system is used to define the velocity zero point. We determined each absorber's systemic redshift, $z_{\rm abs}$, from the optical depth mean of the MgII λ2796 profiles. We solved the implicit equation,

$$\int_{\lambda_b}^{\lambda_{\rm sys}} \tau_a(\lambda) d\lambda = \int_{\lambda_{\rm sys}}^{\lambda_r} \tau_a(\lambda) d\lambda, \tag{A1}$$

for $\lambda_{\rm sys}$, the observed wavelength at the optical depth median, where λ_b and λ_r are the extreme blueward and redward wavelengths of the overall system, respectively, and $\tau_a(\lambda)$ is the apparent optical depth (Savage & Sembach 1991),

$$\tau_a(\lambda) = \ln \left[\frac{I_c(\lambda)}{I(\lambda)} \right]. \tag{A2}$$

The optical depth median, as opposed to the flux median [i.e. $\{1-I(\lambda)/I_c(\lambda)\}$], is used because it weights the absorption by the *quantity of gas*, providing a column density weighted median. Where the profiles are saturation, i.e. $I(\lambda) \leq |\sigma_I(\lambda)|$, the apparent optical depth is a lower limit, given by $\tau_a(\lambda) = \ln[I_c(\lambda)/|\sigma_I(\lambda)|]$. Between kinematic subsystems, $\tau_a \equiv 0$, in order to eliminate continuum noise.

The absorber redshift is then obtained from $z_{\rm abs} = \lambda_{\rm sys}/2796.352 - 1$. The *formal* redshift uncertainities are typically $(1-5) \times 10^{-6}$, less than ~ 1 km s^{-1} (co–moving).

Equivalent Widths

The standard expression for the observed equivalent width is

$$W = \int_{\lambda_b}^{\lambda_r} \left[1 - \frac{I(\lambda)}{I_c(\lambda)} \right] d\lambda. \tag{A3}$$

The integration is performed for each kinematic subsystem and then the total system equivalent width is obtained by the sum. The limits of integration, λ_b and λ_r, are determined as described in § 2.3.3.

Subsystem Velocities

Each kinematic subsystem has a non–zero velocity. As with the absorber systemic redshifts, we compute the velocities from the apparent optical depth across the MgII λ2796 profile. The velocity, $\langle v \rangle$, is the first velocity moment of the optical depth,

$$\langle v \rangle = \frac{\tau_a^{(1)}}{\tau_a} = \frac{\int_{v_b}^{v_r} \tau_a(v) v dv}{\int_{v_b}^{v_r} \tau_a(v) dv} \tag{A4}$$

where $v = (c/\lambda_{\rm sys}) \cdot (\lambda - \lambda_{\rm sys})$, and where the integration is performed over the wavelength region defining each kinematic subsystem.

Velocity Widths

The velocity width of a kinematic subsystem, ω_v, is defined by the second moment of the apparent optical depth,

$$\omega_v^2 = \frac{\tau_a^{(2)}}{\tau_a} = \frac{\int_{v_b}^{v_r} \tau_a(v) \left[v - \langle v \rangle \right]^2 dv}{\int_{v_b}^{v_r} \tau_a(v) dv}. \tag{A5}$$

This quantity is the equivalent Gaussian width of the optical depth profile.

Apparent Column Densities

The "apparent optical depth" technique of Savage & Sembach (1991) was employed to compute column density profiles, $N(v)$ [atoms cm^{-2}], from

$$N_a(v) = \frac{m_e c}{\pi e^2} \frac{\tau_a(v)}{f\lambda_{\rm o}}, \tag{A6}$$

where fundamental constants have the usual meanings, and the apparent optical depth is given by Equation A2. The $N_a(v)$ profiles of doublets, or other same–ion transitions having $f\lambda_{\rm o}$ differing by a factor of two, can be used to discern the velocity location of unresolved saturation in absorption profiles.

Savage & Sembach have shown that this technique yields accurate column densities when the width of the instrumental spread function does not exceed the *intrinsic* line widths by more than a factor of a few. No corrections [also see Jenkins (1997)] have been applied to the measured $N_a(v)$.

The integrated apparent column density of a system or subsystem is given by

$$N_a = \int_{v_b}^{v_r} N_a(v) dv, \tag{A7}$$

where v_b and v_r are the velocity extrema of the system or kinematic subsystem being measured.

For adopting the "best value" of N_a for an ion, there are three possibilities: (1) All transitions of an ion exhibit some saturation between v_b and v_r, so that $N_a(v)$ is a lower limit. Often, the transition with the smallest $f\lambda$ provides the best constraints on the lower limit; (2) All but one transition of an ion exhibits saturation, in which case, the adopted column density is taken from the unsaturated transition; and (3) All or more than one transition of an ion are unsaturated, providing multiple independent measurements. The adopted value is computed from the optimally weighted mean [i.e. weighted by $1/\sigma^2(N_a)$].

Voigt Profile Decomposition

Voigt profile (VP) decomposition is an established technique for modeling absorption profiles because it is well suited for parameterizing the absorbing gas properties into physically meaningful quantities, i.e. the number of components (clouds), their line–of–sight velocities, column densities, and Doppler b parameters.

When an absorption line having optical depth $\tau(\lambda)$ is recorded by an instrument having a finite resolution defined by its instrumental spread function (ISF), $\Phi(\delta\lambda)$, the measured spectrum is the convolution of the intrinsic spectrum and the ISF,

$$I_{\rm obs}(\lambda) = \Phi(\delta\lambda) \otimes \{I_{\rm o}(\lambda) \exp\left[-\tau(\lambda)\right]\}, \tag{A8}$$

where $I_{\rm o}(\lambda)$ is the emitted intensity, and $I_{\rm obs}(\lambda)$ is the observed intensity.

The optical depth is the product of the line of sight integrated column density, $N = \int n(l) dl$ cm^{-2}, and the atomic absorption coefficient, $\alpha(\lambda)$, and is given by

$$\tau(\lambda) = N\alpha(\lambda) = \frac{\sqrt{\pi} e^2}{m_e c^2} \frac{N f \lambda_{\rm o}^2}{\Delta_\lambda} u(x,y), \tag{A9}$$

where $u(x,y)$ is the Voigt function evaluated at $x = (\lambda - \lambda_{\rm o})/\Delta_\lambda$ and $y = \lambda_{\rm o}^2 \Gamma / 4\pi c \Delta_\lambda$, and where Γ is the transition damping constant (see Table 2) and Δ_λ is the Doppler width. This formalism assumes that the dominant line broadening mechanism is a Lorentzian convolved with a Gaussian (the former being the intrinsic line width and the latter being due to line–of–sight thermal and/or bulk motions). For the computation of the Voigt function, we used the real part of the complex probability function,

$$\begin{aligned} w(z) &= e^{-z^2} \left[1 + \frac{2i}{\sqrt{\pi}} \int_0^z e^{-t^2} dt\right] \\ &= e^{-z^2} {\rm erfc}(-iz) \\ &= u(x,y) + iv(x,y), \end{aligned} \tag{A10}$$

which is accurately computed using the very efficient routine CPF12 (Humlíček 1979).

Thus, for each VP, there are three free parameters, N, $\lambda_{\rm o}$, and Δ_λ. When a systems is a complex blend of multiple VP components, the optical depth used in Equation A8 is the sum of the individual components,

$$\tau(\lambda) = \sum_{i=1}^{N_{\rm vp}} \tau_i(\lambda), \tag{A11}$$

where $\tau_i(\lambda)$ is given by Equation A9, and the number of free parameters becomes $3N_{\rm vp}$.

The component velocities of all transitions are "tied" together, as are the column densities of all transitions of a given ion. The column density of each ion is allowed to vary freely as are the b parameters. For the statistical modeling, we use a χ^2 minimization with a code of our own design, MINFIT (Churchill 1997), which uses the least squares minimizing algorithm DNLSE1 (More 1978) and supporting SLATEC library made publicly available by *netlib.org*.

REFERENCES

Bergeron, J., et al. 1994, ApJ, 436, 33
Bergeron, J. & Boissé, P. 1991, A&A, 243, 344
Boissé, P. Boulade, D., Kunth, D., Tytler, D., & Vigroux, L. 1992, A&A, 262, 401,
Blitz, L., Spergel, D. N., Teuben, P. J., Hartmann, D., & Burton, W. B., 1999, ApJ, 514, 818
Bowen, D. V., Blades, J. C., & Pettini, M. 1995, ApJ, 448, 634
Braun, R., & Burton, W. B. 1999, A&A, 341, 437
Cardelli, J. A., & Savage, B. D. 1995, ApJ, 452, 275
Carswell, R. F., Lanzetta, K. M., Parnell, H. C., & Webb, J. K. 1991, ApJ, 371, 36
Charlton, J. C., & Churchill, C. W. 1996, ApJ, 465, 631
Charlton, J. C., & Churchill, C. W. 1998, ApJ, 499, 181
Charlton, J. C., Churchill, C. W., & Rigby, J. R. 2000, ApJL, in press
Churchill, C. W. 1995, Lick Technical Report, #74
Churchill, C. W. 1997, Ph.D. Thesis, University of California, Santa Cruz
Churchill, C. W. 2000, in Gas and Galaxy Evolution, eds. J. E., Hibbard, M. P. Rupen, & J. H. van Gorkom, ASP Conference Series, (San Francisco: PASP), astro–ph/0009314
Churchill, C. W., & Charlton, J. C. 1999, AJ, 118, 59
Churchill, C. W., Mellon, R. R., Charlton, J. C., Jannuzi, B. T., Kirhakos, S., Steidel, C. C., & Schneider, D. P. 1999a, ApJ, 519, L43
Churchill, C. W., Mellon, R. R., Charlton, J. C., Jannuzi, B. T., Kirhakos, S., Steidel, C. C., & Schneider, D. P. 2000a, ApJ, in press
Churchill, C. W., Mellon, R. R., Charlton, J. C., Jannuzi, B. T., Kirhakos, S., Steidel, C. C., & Schneider, D. P. 2000b, ApJ, in press
Churchill, C. W., Rigby, J. R., Charlton, J. C., & Vogt, S. S. 1999b, ApJS, 120, 51
Churchill, C. W., Steidel, C. C., & Vogt, S. S. 1996, ApJ, 471, 164
Churchill, C. W., Vogt, S. S., & Charlton, J. C. 2000, ApJ, in preparation
Cowie, L. L., & McKee, C. F. 1977, ApJ, 211, 135
Ferland, G. J. 1996, Hazy, University of Kentucky Internal Report
Guillemin, P., & Bergeron, J. 1997, A&A, 328, 499
Hibbard, J. E., Rupen, M. P., & van Gorkom, J. H., eds. Gass & Galaxy Evolution, ASP Conference Series, in prep
Hiebert, K. L., www.netlib.org
Horne, K. 1986, PASP, 98, 609
Humlíček, J. 1979, Journal of Quantative Spectroscopy and Radiative Transfer, 21, 309
Hu, E. M., Tae–Sun, K., Cowie, L., Songaila, A., & Rauch, M. 1995, AJ, 110, 1526
Jenkins, E. B. 1996, ApJ, 471, 292
Lane, W. M., Briggs, F. H., Smette, A. 2000, ApJ, 532, 146L
Lanzetta, K. M., & Bowen, D. V. 1990, ApJ, 357, 321
Lanzetta, K. M., & Bowen, D. V. 1992, ApJ, 391, 48
Lanzetta, K. M., Turnshek, D. A., & Wolfe, A. M. 1987, ApJ, 322, 739
Le Brun, V., Bergeron, J., Boissé, P.,& Deharveng, J. M. 1997, A&A, 321, 733
Lu, L., Sargent, W. L. W., Barlow, T. A., Churchill, C. W., & Vogt, S. S. 1996a, ApJS, 107, 475
Lu, L., Sargent, W. L. W., Womble, D. S., & Takada–Hidai, M. 1996b, ApJ, 472, 509
Marsh, T. 1989, PASP, 100, 1032
Mo, H. J., & Miralda-Escudé, J. 1996, ApJ, 469, 589
More, J. J. 1978, in Numerical Analysis Proceedings, ed. G.A. Watson, Lecture Notes in Mathematics (Springer–Verlag), 630
Morton, D. C. 1991, ApJS, 77, 119
Murray, S. D., White, S. D. M., Blondin, J. M., & Lin, D. N. C. 1993, ApJ, 407, 588
Petitjean, P., & Bergeron, J. 1990, A&A, 231, 309
Press, W. H., Flannery, B. P., Teukolsky, S. A., & Vetterling, W. T. 1986, Numerical Recipes: The Art of Scientific Computing (Cambridge University Press)
Rao, S. M., 2000, private communication
Rao, S. M., & Turnshek, D. A. 1998, ApJ, 500, L115
Rao, S. M., & Turnshek, D. A. 1999, (astro–ph/9909164)
Rigby, J. R., Charlton, J. C., & Churchill, C. W. 2000, ApJ, submitted
Sargent, W.L.W., Steidel, C.C, & Boksenberg, A. 1988, ApJ, 334, 22
Savage, B. D., & Sembach, K. R. 1991, ApJ, 379, 245
Schneider, D. P., et al. 1993, ApJS, 87, 45
Sembach, K. R., & Savage, B. D. 1992, ApJS, 83, 147
Steidel, C. C. 1993, in The Environment and Evolution of Galaxies, eds. J. M. Shull & H. A. Thronson, Jr. (Dordrecht : Kluwer), 263
Steidel, C. C. 1995, in QSO Absorption Lines, ed. G. Meylan (Garching : Springer Verlag), 139
Steidel, C. C. 1998, in Galactic Halos: A UC Santa Cruz Workshop, ASP Conf. Series, V136, ed. D. Zaritsky (San Francisco : PASP), 167
Steidel, C. C., Bowen, D. V., Blades, J., & Dickinson, M. 1995 ApJL, L440, 45
Steidel, C. C., Dickinson, M., Meyer, D. M., Adelberger, K. L., & Sembach, K. R. 1997, ApJ, 480, 568
Steidel, C. C., Dickinson, M. & Persson, E. 1994, ApJ, 437, L75
Steidel, C. C., & Sargent, W. L. W. 1992, ApJS, 80, 1 (SS92)
Tripp, T. M., Lu, L., & Savage, B. D. 1996, ApJS, 102, 239
Tytler, D., Boksenberg, A., Sargent, W. L. W., Young, P., & Kunth, D. 1987, ApJS, 64, 667
van Gorkom, J. H. 1992, in Morphological and Physical Classifications of Galaxies, eds. G. Longo, M. Capaccioli, & G. Busarello (Kluwer Academic), 223
Vogt, S. S., et al. 1994, in Proceedings of the SPIE, 2128, 326
Wakker, B. P, & van Woerden, H. 1997, ARA&A, 35, 217
Yun, M. S., Ho, P. T. P., & Lo, K. Y. 1994, Nature, 372, 530
Zhang, Y., Anninos, P., Norman, M. L., & Meiksin, A 1997, ApJ, 485, 496
Zwaan, M. A., & Briggs, F. H. 2000, ApJ, 530, L61

TABLE 3
KINEMATIC SUBSYSTEM PROPERTIES AND SYSTEM TOTALS

QSO	$z_{\rm abs}$	System	$\langle v \rangle$ [km s^{-1}]	ω [km s^{-1}]	$W_{\rm r}(2796)$ [Å]	DR
Q0002+051	0.85139	1	-12.0 ± 0.4	17.8 ± 0.2	0.658 ± 0.005	1.06 ± 0.01
		2	170.5 ± 0.3	14.5 ± 0.3	0.379 ± 0.006	1.13 ± 0.03
		3	296.6 ± 1.0	5.2 ± 1.0	0.039 ± 0.004	1.63 ± 0.33
		4	408.6 ± 0.9	4.8 ± 0.9	0.043 ± 0.004	1.32 ± 0.22
		Total	···	97.7 ± 0.9	1.120 ± 0.010	1.10 ± 0.01
Q0117+213	0.57640	Total	···	27.1 ± 0.5	0.922 ± 0.006	1.08 ± 0.01
Q0117+213	1.04797	1	-86.6 ± 0.3	6.1 ± 0.4	0.097 ± 0.003	1.80 ± 0.09
		2	3.5 ± 0.3	15.7 ± 0.3	0.321 ± 0.004	1.58 ± 0.03
		Total	···	39.4 ± 0.3	0.417 ± 0.005	1.63 ± 0.03
Q0420-014	0.63300	1	-222.4 ± 0.6	6.0 ± 0.7	0.089 ± 0.005	1.50 ± 0.14
		2	-6.4 ± 1.2	31.0 ± 0.4	0.783 ± 0.009	1.30 ± 0.02
		Total	···	61.1 ± 1.4	0.873 ± 0.010	1.32 ± 0.02
Q0454+039	0.85957	Total	···	45.9 ± 0.6	1.494 ± 0.009	1.03 ± 0.01
Q0454+039	1.15325	1	-96.1 ± 0.6	2.8 ± 1.0	0.032 ± 0.003	1.72 ± 0.25
		2	2.5 ± 0.3	15.9 ± 0.5	0.389 ± 0.005	1.39 ± 0.03
		3	99.2 ± 0.6	4.2 ± 0.8	0.037 ± 0.003	2.20 ± 0.33
		Total	···	31.8 ± 0.8	0.458 ± 0.006	1.45 ± 0.03
Q0454-220	0.47441	Total	···	42.3 ± 0.7	1.439 ± 0.013	1.14 ± 0.01
Q0454-220	0.48334	Total	···	15.8 ± 0.5	0.426 ± 0.006	1.34 ± 0.03
Q0823-223	0.91102[a]	1	-36.0 ± 0.8	50.8 ± 0.3	0.940 ± 0.005	1.40 ± 0.02
		2	146.1 ± 0.2	13.6 ± 0.2	0.304 ± 0.004	···
		3	214.3 ± 0.9	5.0 ± 1.0	0.024 ± 0.003	···
		Total	···	89.4 ± 0.6	1.268 ± 0.007	···
Q1101-264	0.35900	Total	···	24.6 ± 0.5	0.550 ± 0.006	1.31 ± 0.02
Q1148+384	0.55336	Total	···	45.5 ± 0.8	0.642 ± 0.011	1.74 ± 0.06
Q1206+459	0.92760	1	-404.9 ± 0.7	5.0 ± 0.7	0.032 ± 0.002	1.82 ± 0.27
		2	-339.6 ± 0.6	12.5 ± 0.4	0.083 ± 0.003	1.66 ± 0.11
		3	-257.3 ± 0.3	3.9 ± 0.4	0.064 ± 0.002	1.71 ± 0.12
		4	-183.8 ± 0.5	6.8 ± 0.4	0.049 ± 0.003	2.15 ± 0.24
		5	6.2 ± 0.9	34.2 ± 0.5	0.656 ± 0.005	1.31 ± 0.01
		Total	···	117.5 ± 1.8	0.883 ± 0.007	1.41 ± 0.02

TABLE 3—*Continued*

QSO	$z_{\rm abs}$	System	$\langle v \rangle$ [km s^{-1}]	ω [km s^{-1}]	$W_{\rm r}(2796)$ [Å]	DR
Q1222+228	0.66805	1	-1.7 ± 0.5	15.4 ± 0.3	0.408 ± 0.007	1.46 ± 0.03
		2	232.2 ± 0.5	6.7 ± 0.5	0.081 ± 0.004	1.48 ± 0.12
		Total	···	76.9 ± 1.8	0.489 ± 0.008	1.46 ± 0.03
Q1241+176	0.55048	1	0.7 ± 0.6	18.9 ± 0.7	0.444 ± 0.009	1.30 ± 0.04
		2	147.9 ± 1.1	6.6 ± 0.7	0.035 ± 0.004	1.41 ± 0.29
		Total	···	33.0 ± 1.7	0.479 ± 0.010	1.31 ± 0.04
Q1248+401	0.77296	1	7.1 ± 0.7	25.9 ± 0.3	0.631 ± 0.004	1.26 ± 0.01
		2	226.3 ± 0.6	5.6 ± 0.8	0.064 ± 0.003	1.42 ± 0.12
		Total	···	54.5 ± 1.1	0.694 ± 0.005	1.27 ± 0.02
Q1254+044	0.51939[b]	1	-261.1 ± 1.0	6.5 ± 0.9	0.062 ± 0.006	2.63 ± 0.64
		2	-159.0 ± 1.1	6.2 ± 0.8	0.048 ± 0.006	···
		3	1.9 ± 0.8	13.9 ± 0.4	0.446 ± 0.009	1.17 ± 0.04
		Total	···	87.5 ± 4.7	0.556 ± 0.013	1.38 ± 0.05
Q1254+044	0.93423	Total	···	21.2 ± 0.3	0.341 ± 0.005	1.51 ± 0.04
Q1317+274	0.66005[b]	1	-3.2 ± 0.2	9.1 ± 0.2	0.226 ± 0.003	1.49 ± 0.04
		2	45.2 ± 1.2	4.7 ± 1.1	0.014 ± 0.002	···
		3	89.3 ± 0.7	10.8 ± 0.7	0.078 ± 0.003	1.67 ± 0.16
		4	143.2 ± 1.1	8.0 ± 0.7	0.026 ± 0.003	···
		Total	···	52.0 ± 0.6	0.344 ± 0.006	1.68 ± 0.06
Q1421+331	0.90287	1	-19.9 ± 1.4	41.4 ± 0.6	0.885 ± 0.008	1.32 ± 0.02
		2	82.4 ± 0.4	8.4 ± 0.7	0.156 ± 0.005	1.29 ± 0.07
		Total	···	51.4 ± 1.0	1.041 ± 0.010	1.32 ± 0.02
Q1421+331	1.17261	Total	···	24.1 ± 0.5	0.516 ± 0.006	1.40 ± 0.03
Q1634+706	0.99024	Total	···	17.9 ± 0.1	0.561 ± 0.003	1.33 ± 0.01
Q2128-123	0.42973	Total	···	16.5 ± 0.4	0.355 ± 0.008	1.41 ± 0.06
Q2145+064	0.79078	1	-105.1 ± 0.3	6.6 ± 0.3	0.158 ± 0.004	1.33 ± 0.05
		2	0.9 ± 0.5	9.7 ± 0.5	0.152 ± 0.005	1.60 ± 0.10
		3	66.8 ± 0.5	13.1 ± 0.4	0.208 ± 0.005	1.51 ± 0.07
		Total	···	74.7 ± 0.4	0.517 ± 0.008	1.47 ± 0.04

[a]The λ2803 transition was only partially covered by the CCD.

[b]The λ2803 transition was not formally detected in some subsystems. However, the subsystems are deemed real based upon VP decomposition.

TABLE 4
SAMPLES AND SUBSAMPLES

		Sample A $W_r \geq 0.3$ Å	Sample B $0.3 \leq W_r < 0.6$ Å	Sample C $0.6 \leq W_r < 1.0$ Å	Sample D $W_r \geq 0.6$ Å	Sample E $W_r \geq 1.0$ Å
N		23	13	5	10	5
$\langle W_r(2796) \rangle$, Å		0.56	0.48	0.80	0.98	1.04
$\langle z \rangle$		0.77	0.66	0.69	0.81	0.86
$\langle DR \rangle$		1.4	1.4	1.4	1.3	1.1
Membership Chart						
$0002+051$	0.85139	X			X	X
$0117+213$	0.57640	X		X	X	
$0117+213$	1.04797	X	X			
$0420-014$	0.63300	X		X	X	
$0454+039$	0.85957	X			X	X
$0454+039$	1.15325	X	X			
$0454-220$	0.47441	X			X	X
$0454-220$	0.48334	X	X			
$0823-223$	0.91102	X			X	X
$1101-264$	0.35900	X	X			
$1148+384$	0.55336	X		X	X	
$1206+459$	0.92760	X		X	X	
$1222+228$	0.66805	X	X			
$1241+176$	0.55048	X	X			
$1248+401$	0.77296	X		X	X	
$1254+044$	0.51939	X	X			
$1254+044$	0.93423	X	X			
$1317+274$	0.66005	X	X			
$1421+331$	0.90287	X			X	X
$1421+331$	1.17261	X	X			
$1634+706$	0.99024	X	X			
$2128-123$	0.42973	X	X			
$2148+064$	0.79078	X	X			

TABLE 5
SUBFEATURE EQUIVALENT WIDTHS FOR TARGET TRANSITIONS

System	(v^-, v^+)	MgI $W_r(2853)$	FeII $W_r(2344)$	FeII $W_r(2374)$	FeII $W_r(2383)$	FeII $W_r(2587)$	FeII $W_r(2600)$
Q0002 + 051 $z_{\rm abs} = 0.851394$							
1	(−55, 60)	0.166 ± 0.027	0.225 ± 0.022	0.077 ± 0.025	0.347 ± 0.016	0.170 ± 0.025	0.349 ± 0.014
2	(125, 219)	< 0.027	0.047 ± 0.025	< 0.023	0.082 ± 0.019	< 0.025	0.070 ± 0.017
3	(282, 314)	< 0.012	0.025 ± 0.010	< 0.010	< 0.009	< 0.011	< 0.007
4	(393, 423)	< 0.011	< 0.010	< 0.009	< 0.008	< 0.011	< 0.008
Total	(−55, 423)	0.161 ± 0.027	0.297 ± 0.035	0.077 ± 0.025	0.429 ± 0.025	0.170 ± 0.025	0.419 ± 0.022
Q0058 + 019 $z_{\rm abs} = 0.612672$							
1	(−114, 97)	0.300 ± 0.062	1.230 ± 0.416	0.460 ± 0.592	< 5.357	1.043 ± 0.057	1.274 ± 0.037
Total	(−114, 97)	0.300 ± 0.062	1.230 ± 0.416	0.460 ± 0.592	< 5.357	1.043 ± 0.057	1.274 ± 0.037
Q0117 + 212 $z_{\rm abs} = 0.576398$							
Total	(−62, 91)	0.155 ± 0.023	···	···	···	···	···
Q0117 + 212 $z_{\rm abs} = 1.047971$							
1	(−109, −63)	0.012 ± 0.005	< 0.006	< 0.006	0.018 ± 0.005	< 0.006	0.014 ± 0.005
2	(−46, 51)	0.015 ± 0.010	0.016 ± 0.012	< 0.012	0.061 ± 0.009	< 0.012	0.051 ± 0.009
Total	(−109, 51)	0.027 ± 0.011	0.022 ± 0.012	< 0.018	0.080 ± 0.011	< 0.019	0.065 ± 0.010
Q0420 − 014 $z_{\rm abs} = 0.633004$							
1	(−241, −201)	< 0.009	< 0.073	< 0.049	< 0.051	< 0.027	< 0.018
2	(−96, 51)	0.062 ± 0.031	< 0.229	< 0.153	< 0.174	< 0.097	0.076 ± 0.054
Total	(−241, 51)	0.062 ± 0.031	< 0.302	< 0.202	< 0.225	< 0.124	0.076 ± 0.054
Q0450 − 132 $z_{\rm abs} = 0.493937$							
Total	(−91, 80)	0.078 ± 0.068	···	···	···	···	···
Q0450 − 132 $z_{\rm abs} = 1.174615$							
1	(−119, 135)	···	0.765 ± 0.020	0.485 ± 0.033	1.072 ± 0.019	···	1.131 ± 0.019
2	(143, 176)	···	< 0.005	< 0.007	< 0.006	···	0.014 ± 0.006
Total	(−119, 176)	···	0.765 ± 0.020	0.485 ± 0.033	1.072 ± 0.019	···	1.146 ± 0.020
Q0454 + 039 $z_{\rm abs} = 0.859565$							
Total	(−95, 121)	0.306 ± 0.022	0.978 ± 0.015	0.719 ± 0.021	1.144 ± 0.018	1.007 ± 0.016	1.232 ± 0.014
Q0454 + 039 $z_{\rm abs} = 1.153254$							
1	(−109, −79)	< 0.004	< 0.005	< 0.004	···	< 0.004	0.009 ± 0.005
2	(−35, 81)	0.026 ± 0.012	0.048 ± 0.017	0.019 ± 0.014	0.056 ± 0.020	0.014 ± 0.013	0.075 ± 0.014
3	(83, 115)	< 0.004	< 0.006	< 0.005	< 0.007	< 0.004	< 0.005
Total	(−109, 115)	0.026 ± 0.012	0.048 ± 0.017	0.019 ± 0.014	0.056 ± 0.020	0.014 ± 0.013	0.084 ± 0.015
Q0454 − 220 $z_{\rm abs} = 0.474410$							
Total	(−98, 106)	0.333 ± 0.014	···	···	···	0.677 ± 0.067	0.975 ± 0.029
Q0454 − 220 $z_{\rm abs} = 0.483340$							
Total	(−60, 41)	0.070 ± 0.010	···	···	···	0.069 ± 0.028	0.162 ± 0.043
Q0823 − 223 $z_{\rm abs} = 0.911017$							
1	(−157, 75)	0.189 ± 0.029	0.123 ± 0.050	0.006 ± 0.054	0.371 ± 0.039	0.118 ± 0.026	0.298 ± 0.024
2	(105, 185)	0.034 ± 0.011	0.048 ± 0.020	< 0.022	0.123 ± 0.014	0.037 ± 0.009	0.111 ± 0.009
3	(199, 230)	< 0.005	< 0.010	< 0.011	< 0.007	< 0.005	0.007 ± 0.005
Total	(−157, 230)	0.224 ± 0.031	0.171 ± 0.054	0.006 ± 0.054	0.494 ± 0.041	0.155 ± 0.028	0.416 ± 0.026

TABLE 5—*Continued*

System	(v^-, v^+)	Mg I $W_r(2853)$	Fe II $W_r(2344)$	Fe II $W_r(2374)$	Fe II $W_r(2383)$	Fe II $W_r(2587)$	Fe II $W_r(2600)$
Q1101 − 264 $z_{\rm abs} = 0.359002$							
Total	$(-57, 94)$	···	···	···	···	···	···
Q1148 + 384 $z_{\rm abs} = 0.553362$							
Total	$(-96, 101)$	< 0.063	···	···	···	0.065 ± 0.081	0.151 ± 0.071
Q1206 + 459 $z_{\rm abs} = 0.927602$ A[E]							
1	$(-421, -386)$	< 0.005	< 0.006	< 0.006	< 0.006	< 0.006	< 0.006
2	$(-366, -310)$	< 0.007	< 0.009	< 0.009	< 0.009	< 0.010	< 0.008
3	$(-275, -236)$	< 0.005	< 0.007	< 0.007	< 0.007	< 0.008	< 0.006
4	$(-204, -160)$	< 0.006	< 0.007	< 0.007	< 0.008	< 0.008	< 0.006
5	$(-80, 89)$	0.042 ± 0.020	0.033 ± 0.024	0.018 ± 0.024	0.098 ± 0.026	0.030 ± 0.030	0.077 ± 0.020
Total	$(-421, 89)$	0.042 ± 0.020	0.033 ± 0.024	0.018 ± 0.024	0.098 ± 0.026	0.030 ± 0.030	0.077 ± 0.020
Q1213 − 003 $z_{\rm abs} = 1.320059$							
Total	$(-221, 175)$	0.686 ± 0.054	1.073 ± 0.091	0.417 ± 0.067	1.668 ± 0.057	0.875 ± 0.066	1.585 ± 0.031
Q1213 − 003 $z_{\rm abs} = 1.554148$							
1	$(-273, -235)$	< 0.010	< 0.008	< 0.007	< 0.008	< 0.010	< 0.008
2	$(-218, 155)$	0.215 ± 0.075	0.499 ± 0.060	0.278 ± 0.049	0.849 ± 0.046	0.464 ± 0.064	0.853 ± 0.047
Total	$(-273, 155)$	0.215 ± 0.075	0.499 ± 0.060	0.278 ± 0.049	0.849 ± 0.046	0.464 ± 0.064	0.853 ± 0.047
Q1222 + 228 $z_{\rm abs} = 0.668052$							
1	$(-43, 42)$	0.038 ± 0.016	0.063 ± 0.045	< 0.035	0.113 ± 0.035	< 0.027	0.119 ± 0.022
2	$(213, 253)$	< 0.009	< 0.024	< 0.018	0.028 ± 0.021	< 0.015	0.047 ± 0.011
Total	$(-43, 253)$	0.038 ± 0.016	0.063 ± 0.045	< 0.052	0.140 ± 0.041	< 0.042	0.166 ± 0.025
Q1225 + 317 $z_{\rm abs} = 1.794833$							
1	$(-147, 136)$	0.275 ± 0.046	0.300 ± 0.043	0.086 ± 0.035	0.661 ± 0.025	···	0.620 ± 0.050
2	$(136, 195)$	< 0.013	< 0.013	< 0.009	< 0.009	···	< 0.016
Total	$(-147, 195)$	0.275 ± 0.046	0.300 ± 0.043	0.086 ± 0.035	0.661 ± 0.025	···	0.620 ± 0.050
Q1241 + 176 $z_{\rm abs} = 0.550482$							
1	$(-49, 62)$	0.098 ± 0.030	···	···	···	0.096 ± 0.047	0.236 ± 0.048
2	$(133, 161)$	< 0.011	···	···	···	< 0.017	< 0.018
Total	$(-49, 161)$	0.098 ± 0.030	···	···	···	0.096 ± 0.047	0.236 ± 0.048
Q1248 + 401 $z_{\rm abs} = 0.772957$							
1	$(-52, 69)$	0.049 ± 0.021	0.105 ± 0.026	0.045 ± 0.026	0.241 ± 0.021	0.116 ± 0.019	0.233 ± 0.018
2	$(207, 248)$	0.016 ± 0.007	< 0.011	< 0.011	< 0.010	< 0.008	0.014 ± 0.008
Total	$(-52, 248)$	0.065 ± 0.022	0.105 ± 0.026	0.045 ± 0.026	0.241 ± 0.021	0.116 ± 0.019	0.247 ± 0.020
Q1254 + 044 $z_{\rm abs} = 0.519389$							
1	$(-277, -244)$	< 0.013	···	···	···	< 0.018	< 0.021
2	$(-173, -143)$	< 0.012	···	···	···	< 0.016	< 0.018
3	$(-33, 40)$	0.169 ± 0.019	···	···	···	0.185 ± 0.029	0.298 ± 0.024
Total	$(-407, 40)$	0.169 ± 0.019	···	···	···	0.185 ± 0.029	0.298 ± 0.024
Q1254 + 044 $z_{\rm abs} = 0.934232$							
Total	$(-61, 32)$	0.005 ± 0.019	0.021 ± 0.022	< 0.023	0.056 ± 0.022	0.040 ± 0.020	0.051 ± 0.015
Q1317 + 274 $z_{\rm abs} = 0.660051$							
1	$(-33, 30)$	0.026 ± 0.009	0.060 ± 0.021	< 0.028	0.104 ± 0.014	0.028 ± 0.010	0.099 ± 0.011
2	$(36, 58)$	< 0.004	< 0.010	< 0.013	< 0.007	< 0.005	< 0.006
3	$(62, 118)$	< 0.008	< 0.021	< 0.028	0.049 ± 0.013	< 0.009	0.027 ± 0.012
4	$(126, 158)$	< 0.006	< 0.015	< 0.018	< 0.009	< 0.006	< 0.008
Total	$(-33, 158)$	0.026 ± 0.009	0.060 ± 0.021	< 0.087	0.153 ± 0.020	0.028 ± 0.010	0.126 ± 0.016

TABLE 5—*Continued*

System	(v^-, v^+)	MgI $W_r(2853)$	FeII $W_r(2344)$	FeII $W_r(2374)$	FeII $W_r(2383)$	FeII $W_r(2587)$	FeII $W_r(2600)$
			Q1329 + 412 $z_{\rm abs} = 0.893337$				
1	$(-45, 25)$	< 0.033	< 0.037	< 0.030	0.069 ± 0.021	< 0.034	0.051 ± 0.031
2	$(102, 139)$	< 0.022	< 0.022	< 0.016	0.032 ± 0.013	< 0.021	0.029 ± 0.018
Total	$(-45, 139)$	< 0.055	< 0.058	< 0.046	0.101 ± 0.025	< 0.054	0.080 ± 0.035
			Q1354 + 193 $z_{\rm abs} = 0.456588$				
1	$(-90, -61)$	< 0.009	···	···	···	···	< 0.033
2	$(-51, 56)$	0.038 ± 0.028	···	···	···	···	0.149 ± 0.088
Total	$(-90, 56)$	0.038 ± 0.028	···	···	···	···	0.149 ± 0.088
			Q1421 + 331 $z_{\rm abs} = 0.902871$				
1	$(-118, 46)$	0.048 ± 0.032	0.163 ± 0.030	0.063 ± 0.028	0.309 ± 0.027	0.121 ± 0.045	0.223 ± 0.034
2	$(50, 112)$	< 0.014	< 0.014	< 0.012	0.022 ± 0.015	< 0.022	< 0.016
Total	$(-118, 112)$	0.048 ± 0.032	0.163 ± 0.030	0.063 ± 0.028	0.331 ± 0.031	0.121 ± 0.045	0.223 ± 0.034
			Q1421 + 331 $z_{\rm abs} = 1.172609$				
Total	$(-60, 53)$	0.057 ± 0.026	0.058 ± 0.020	< 0.022	0.140 ± 0.018	< 0.031	0.131 ± 0.018
			Q1622 + 235 $z_{\rm abs} = 0.656114$				
Total	$(-91, 89)$	···	< 0.130	0.447 ± 0.152	< 0.155	0.700 ± 0.090	1.015 ± 0.050
			Q1622 + 235 $z_{\rm abs} = 0.797107$				
1	$(-83, -46)$	< 0.021	< 0.055	< 0.049	···	< 0.024	< 0.027
2	$(-40, 26)$	< 0.035	< 0.068	< 0.070	···	< 0.038	< 0.040
3	$(47, 80)$	< 0.198	< 0.042	< 0.038	···	< 0.021	< 0.024
Total	$(-83, 80)$	< 0.254	< 0.166	< 0.157	···	< 0.083	< 0.092
			Q1622 + 235 $z_{\rm abs} = 0.891253$				
Total	$(-114, 95)$	0.307 ± 0.033	0.659 ± 0.102	0.431 ± 0.089	1.517 ± 1.587	0.754 ± 0.344	1.080 ± 0.421
			Q1634 + 704 $z_{\rm abs} = 0.990240$				
Total	$(-48, 59)$	0.058 ± 0.010	0.069 ± 0.037	< 0.033	0.135 ± 0.018	0.042 ± 0.015	0.127 ± 0.011
			Q2128 − 123 $z_{\rm abs} = 0.429735$				
Total	$(-54, 35)$	0.162 ± 0.026	···	···	···	···	···
			Q2145 + 064 $z_{\rm abs} = 0.790777$				
1	$(-127, -82)$	< 0.011	0.008 ± 0.016	< 0.017	0.053 ± 0.019	···	0.041 ± 0.014
2	$(-23, 30)$	< 0.012	< 0.019	< 0.019	< 0.026	···	< 0.019
3	$(32, 105)$	< 0.015	< 0.026	< 0.026	0.034 ± 0.032	···	< 0.023
Total	$(-127, 105)$	< 0.038	0.008 ± 0.016	< 0.063	0.087 ± 0.038	···	0.041 ± 0.014

TABLE 6
SUBSYSTEM AOD COLUMN DENSITIES

System	(v^-, v^+)	MgII	MgI	FeII
		Q0002 + 051 $z_{\rm abs} = 0.851394$		
1	$(-55, 60)$	13.773 ± 0.001	12.188 ± 0.024	13.753 ± 0.003
2	$(125, 219)$	13.379 ± 0.003	< 10.874	12.801 ± 0.024
3	$(282, 314)$	12.001 ± 0.035	< 10.655	< 11.300
4	$(393, 423)$	12.028 ± 0.031	< 10.642	< 11.279
Total	$(-55, 423)$	13.931 ± 0.001	12.232 ± 0.022	13.802 ± 0.004
		Q0117 + 212 $z_{\rm abs} = 0.5764$		
Total	$(-62, 91)$	> 14.080	12.144 ± 0.019	
		Q0117 + 212 $z_{\rm abs} = 1.047971$		
1	$(-109, -63)$	12.486 ± 0.010	11.006 ± 0.077	12.038 ± 0.045
2	$(-46, 51)$	13.075 ± 0.005	11.065 ± 0.097	12.616 ± 0.018
Total	$(-109, 51)$	13.174 ± 0.004	11.337 ± 0.063	12.718 ± 0.017
		Q0420 − 014 $z_{\rm abs} = 0.633004$		
1	$(-241, -201)$	12.456 ± 0.019	< 10.517	< 11.806
2	$(-96, 51)$	> 13.753	11.745 ± 0.057	12.840 ± 0.081
Total	$(-241, 51)$	13.774 ± 0.001	11.770 ± 0.054	12.879 ± 0.075
		Q0454 + 039 $z_{\rm abs} = 0.859565$		
Total	$(-95, 121)$	> 14.323	12.453 ± 0.009	15.068 ± 0.028
		Q0454 + 039 $z_{\rm abs} = 1.153254$		
1	$(-109, -79)$	11.933 ± 0.028	< 10.186	11.804 ± 0.108
2	$(-35, 81)$	13.391 ± 0.008	11.271 ± 0.072	12.773 ± 0.020
3	$(83, 115)$	11.943 ± 0.028	< 10.195	< 11.126
Total	$(-109, 115)$	13.421 ± 0.008	11.338 ± 0.061	12.826 ± 0.020
		Q0454 − 220 $z_{\rm abs} = 0.474410$		
Total	$(-98, 106)$	> 14.272	12.532 ± 0.005	> 14.515
		Q0454 − 220 $z_{\rm abs} = 0.483340$		
Total	$(-60, 41)$	> 13.527	11.849 ± 0.018	13.384 ± 0.051
		Q0823 − 223 $z_{\rm abs} = 0.911017$		
1	$(-157, 75)$	> 13.752	12.234 ± 0.016	13.470 ± 0.007
2	$(105, 185)$	13.072 ± 0.007	11.411 ± 0.057	12.987 ± 0.012
3	$(199, 230)$	11.827 ± 0.038	< 10.305	11.513 ± 0.198
Total	$(-157, 230)$	13.839 ± 0.001	12.299 ± 0.016	13.597 ± 0.006

TABLE 6—*Continued*

System	(v^-, v^+)	MgII	MgI	FeII
		Q1101 − 264 $z_{\rm abs} = 0.359002$		
Total	$(-57, 94)$	> 13.621		
		Q1148 + 384 $z_{\rm abs} = 0.553362$		
Total	$(-96, 101)$	13.433 ± 0.019	< 11.077	13.186 ± 0.046
		Q1206 + 459 $z_{\rm abs} = 0.927602$		
1	$(-421, -386)$	11.910 ± 0.031	< 10.262	< 11.140
2	$(-366, -310)$	12.384 ± 0.014	< 10.366	< 11.242
3	$(-275, -236)$	12.304 ± 0.015	< 10.286	< 11.156
4	$(-204, -160)$	12.099 ± 0.022	< 10.306	< 11.187
5	$(-80, 89)$	> 13.683	11.535 ± 0.053	12.870 ± 0.019
Total	$(-421, 89)$	13.738 ± 0.001	11.627 ± 0.042	12.905 ± 0.018
		Q1222 + 228 $z_{\rm abs} = 0.668052$		
1	$(-43, 42)$	13.290 ± 0.010	11.477 ± 0.068	12.988 ± 0.030
2	$(213, 253)$	12.412 ± 0.019	< 10.509	12.518 ± 0.055
Total	$(-43, 253)$	13.344 ± 0.009	11.521 ± 0.061	13.115 ± 0.026
		Q1241 + 176 $z_{\rm abs} = 0.550482$		
1	$(-49, 62)$	> 13.497	11.964 ± 0.042	> 13.728
2	$(133, 161)$	11.941 ± 0.049	< 10.634	< 11.825
Total	$(-49, 161)$	13.509 ± 0.001	11.984 ± 0.040	< 13.734
		Q1248 + 401 $z_{\rm abs} = 0.772957$		
1	$(-52, 69)$	> 13.710	11.620 ± 0.058	13.544 ± 0.017
2	$(207, 248)$	12.304 ± 0.015	11.141 ± 0.088	11.707 ± 0.178
Total	$(-52, 248)$	13.726 ± 0.001	11.744 ± 0.049	13.550 ± 0.017
		Q1254 + 044 $z_{\rm abs} = 0.519389$		
1	$(-277, -244)$	12.219 ± 0.038	< 10.728	< 11.881
2	$(-173, -143)$	11.970 ± 0.057	< 10.674	< 11.832
3	$(-33, 40)$	> 13.625	12.313 ± 0.041	> 13.948
Total	$(-407, 40)$	13.655 ± 0.002	12.342 ± 0.038	< 13.957
		Q1254 + 044 $z_{\rm abs} = 0.934232$		
Total	$(-61, 32)$	13.261 ± 0.024	10.585 ± 0.569	12.699 ± 0.030
		Q1317 + 274 $z_{\rm abs} = 0.660051$		
1	$(-33, 30)$	12.991 ± 0.008	11.341 ± 0.063	12.992 ± 0.019
2	$(36, 58)$	11.398 ± 0.085	< 10.247	< 11.218
3	$(62, 118)$	12.314 ± 0.017	< 10.450	12.380 ± 0.051
4	$(126, 158)$	11.703 ± 0.050	< 10.328	< 11.309
Total	$(-33, 158)$	13.100 ± 0.007	11.457 ± 0.048	13.100 ± 0.018
		Q1421 + 331 $z_{\rm abs} = 0.902871$		
1	$(-118, 46)$	> 13.827	11.631 ± 0.071	13.699 ± 0.026
2	$(50, 112)$	12.914 ± 0.030	< 10.632	11.928 ± 0.157
Total	$(-118, 112)$	13.877 ± 0.003	11.673 ± 0.065	13.706 ± 0.026

TABLE 6—*Continued*

System	(v^-, v^+)	MgII	MgI	FeII
		Q1421 + 331 $z_{\rm abs} = 1.172609$		
Total	$(-60, 53)$	13.429 ± 0.018	11.688 ± 0.061	13.049 ± 0.014
		Q1634 + 704 $z_{\rm abs} = 0.990240$		
Total	$(-48, 59)$	13.519 ± 0.001	11.684 ± 0.024	13.059 ± 0.010
		Q2128 − 123 $z_{\rm abs} = 0.429735$		
Total	$(-54, 35)$	13.471 ± 0.003	12.248 ± 0.023	
		Q2145 + 064 $z_{\rm abs} = 0.790777$		
1	$(-127, -82)$	12.860 ± 0.006	< 10.558	12.688 ± 0.035
2	$(-23, 30)$	12.681 ± 0.011	< 10.597	···
3	$(32, 105)$	12.845 ± 0.009	< 10.660	12.401 ± 0.149
Total	$(-127, 105)$	13.279 ± 0.005	< 11.084	12.869 ± 0.056

TABLE 7
CLOUD PROPERTIES FOR MgII ABSORBERS

System QSO	z_{abs}	Cloud $\langle v \rangle$ [km s^{-1}]	MgII $\log N$ [cm^{-2}]	MgII b [km s^{-1}]	FeII $\log N$ [cm^{-2}]	FeII b [km s^{-1}]	MgI $\log N$ [cm^{-2}]	MgI b [km s^{-1}]
0002 + 051	0.85139	−32.2	13.36 ± 0.70	7.36 ± 1.66	13.13 ± 0.00	3.70 ± 0.01	< 10.23	···
		−28.1	13.88 ± 0.30	6.17 ± 4.89	12.74 ± 0.01	1.23 ± 0.01	11.84 ± 0.10	11.42 ± 2.45
		28.5	12.50 ± 0.01	8.32 ± 0.31	12.21 ± 0.10	3.62 ± 0.09	∼ 11.6	···
		−13.7	15.85 ± 2.67	2.34 ± 1.27	13.78 ± 0.01	6.84 ± 0.12	11.70 ± 0.10	3.91 ± 1.18
		−1.6	13.51 ± 0.23	3.65 ± 2.26	< 12.28	···	< 10.73	···
		5.4	14.17 ± 0.21	3.68 ± 0.23	13.18 ± 0.03	3.23 ± 0.35	11.71 ± 0.13	8.37 ± 1.39
		142.8	12.92 ± 0.02	3.03 ± 0.17	12.43 ± 0.05	1.86 ± 0.55	< 10.77	···
		149.4	12.39 ± 0.06	9.41 ± 0.79	11.39 ± 0.52	···	< 10.77	···
		172.4	13.42 ± 0.03	3.44 ± 0.14	12.30 ± 0.06	5.59 ± 1.14	< 10.78	···
		182.6	13.20 ± 0.01	4.48 ± 0.17	12.42 ± 0.04	3.58 ± 0.56	< 10.72	···
		296.0	12.04 ± 0.03	6.70 ± 0.70	< 11.74	···	< 10.75	···
		407.4	12.05 ± 0.03	5.23 ± 0.54	< 11.72	···	< 10.80	···
0117 + 213	0.57640	−30.6	13.48 ± 0.31	10.53 ± 2.20	···	···	11.37 ± 0.14	19.02 ± 6.54
		−8.9	13.80 ± 0.31	19.49 ± 2.81	···	···	11.78 ± 0.05	8.66 ± 0.82
		16.3	14.61 ± 0.09	14.39 ± 0.41	···	···	11.77 ± 0.04	23.15 ± 2.65
		77.2	11.60 ± 0.06	4.56 ± 1.11	···	···	< 10.61	···
0117 + 213	1.04797	−97.0	11.55 ± 0.09	2.98 ± 1.21	11.32 ± 0.39	···	11.09 ± 0.15	17.87 ± 8.26
		−85.8	12.46 ± 0.01	5.28 ± 0.26	12.00 ± 0.05	4.56 ± 0.71	< 10.35	···
		−23.3	12.20 ± 0.06	10.87 ± 1.26	< 11.32	···	< 10.35	···
		−0.2	12.74 ± 0.13	10.30 ± 1.93	12.40 ± 0.09	12.54 ± 1.96	11.02 ± 0.12	14.43 ± 5.26
		6.0	12.21 ± 0.28	4.44 ± 1.26	11.70 ± 0.17	···	< 10.35	···
		17.4	12.38 ± 0.11	6.44 ± 0.94	11.65 ± 0.29	4.24 ± 2.48	< 10.35	···
		33.5	11.91 ± 0.08	9.05 ± 1.66	11.84 ± 0.44	12.48 ± 6.33	< 10.35	···
0420 − 014	0.63300	−225.0	12.34 ± 0.06	4.13 ± 0.80	< 11.91	···	< 10.77	···
		−215.8	11.95 ± 0.14	3.47 ± 1.53	< 11.91	···	< 10.77	···
		−82.3	11.91 ± 0.12	4.15 ± 1.25	< 11.89	···	< 10.81	···
		−62.2	12.47 ± 0.07	15.05 ± 2.96	< 11.85	···	< 10.82	···
		−39.5	12.62 ± 0.01	5.99 ± 0.60	< 11.89	···	< 10.83	···
		−22.5	13.05 ± 0.04	15.70 ± 1.34	< 11.88	···	< 10.82	···
		5.4	13.22 ± 0.41	2.24 ± 0.61	12.13 ± 0.28	6.93 ± 6.05	11.01 ± 1.16	∼ 29.0
		16.1	13.37 ± 0.05	8.83 ± 0.70	12.64 ± 0.09	5.94 ± 1.89	11.57 ± 0.15	11.05 ± 3.37
		30.9	12.80 ± 0.03	3.97 ± 0.41	12.20 ± 0.15	1.79 ± 3.27	10.99 ± 0.27	3.74 ± 2.80
0454 + 039	0.85957	−72.2	13.03 ± 0.07	6.25 ± 0.51	12.73 ± 0.03	3.00 ± 0.36	10.34 ± 0.46	∼ 7.0
		−53.8	14.50 ± 2.91	∼ 6.5	14.51 ± 0.05	6.50 ± 0.33	11.74 ± 0.04	6.50 ± 0.72
		−42.5	∼ 13.9	∼ 5.0	13.33 ± 0.21	5.00 ± 1.46	11.19 ± 0.16	5.00 ± 1.81
		−26.9	∼ 13.9	∼ 8.8	13.51 ± 0.06	8.75 ± 1.64	11.12 ± 0.22	8.75 ± 5.72
		−10.4	∼ 14.2	∼ 5.5	13.77 ± 0.19	5.25 ± 0.99	11.47 ± 0.16	5.50 ± 1.27
		4.2	∼ 14.5	∼ 10.8	14.31 ± 0.13	10.50 ± 3.49	11.75 ± 0.17	10.75 ± 4.13
		21.2	∼ 14.6	∼ 8.0	14.73 ± 0.14	8.00 ± 1.62	11.86 ± 0.10	8.00 ± 1.26
		39.6	∼ 14.0	∼ 6.8	13.88 ± 0.14	6.75 ± 2.21	11.24 ± 0.21	6.75 ± 3.90
		53.8	∼ 13.9	∼ 5.5	13.51 ± 0.54	5.50 ± 5.30	11.12 ± 0.57	∼ 5.5
		60.8	∼ 14.1	∼ 4.0	13.68 ± 0.29	4.25 ± 0.68	11.30 ± 0.30	3.50 ± 1.40
		73.6	12.73 ± 0.79	7.00 ± 4.26	12.73 ± 0.04	4.50 ± 0.54	10.34 ± 0.47	∼ 7.5
0454 + 039	1.15325	−96.3	12.00 ± 0.02	2.86 ± 0.36	11.97 ± 0.06	2.02 ± 1.14	< 10.48	···
		−11.5	12.57 ± 0.08	9.22 ± 0.53	12.06 ± 0.08	3.86 ± 1.20	11.09 ± 1.06	∼ 37.9
		−1.2	13.24 ± 0.02	8.46 ± 0.42	12.54 ± 0.03	4.07 ± 0.50	10.87 ± 0.12	3.56 ± 1.66
		12.4	12.58 ± 0.04	9.35 ± 0.49	12.02 ± 0.09	9.25 ± 2.27	∼ 10.9	∼ 0.5
		41.8	11.63 ± 0.06	7.42 ± 1.37	11.32 ± 0.25	∼ 1.2	< 10.47	···
		67.7	11.62 ± 0.05	6.35 ± 1.13	11.49 ± 0.18	6.60 ± 3.94	< 10.21	···
		99.0	11.99 ± 0.02	3.27 ± 0.35	< 11.54	···	< 10.48	···
0454 − 220	0.47441	−81.1	12.48 ± 0.07	3.72 ± 0.54	< 12.10	···	10.63 ± 0.22	5.50 ± 2.62
		−70.8	12.33 ± 0.27	9.77 ± 4.30	< 12.07	···	< 10.16	···
		−52.4	13.06 ± 0.09	10.64 ± 1.84	12.81 ± 0.53	13.60 ± 3.95	< 10.14	···
		−40.4	14.59 ± 2.53	3.65 ± 2.59	13.29 ± 0.31	14.39 ± 7.31	11.11 ± 0.12	8.12 ± 2.27
		−21.9	15.06 ± 2.63	3.74 ± 2.47	12.49 ± 0.49	3.85 ± 5.03	11.47 ± 0.64	0.56 ± 0.33
		−4.3	13.90 ± 2.67	3.60 ± 4.14	15.73 ± 7.98	5.63 ± 8.99	12.31 ± 0.02	17.94 ± 0.97
		18.6	13.90 ± 0.06	23.97 ± 4.55	14.00 ± 0.05	28.40 ± 1.91	11.95 ± 0.05	12.68 ± 0.66
		51.4	13.46 ± 0.07	13.94 ± 0.43	13.61 ± 0.29	6.11 ± 1.54	11.39 ± 0.03	10.22 ± 0.92

TABLE 7—*Continued*

System QSO	$z_{\rm abs}$	Cloud $\langle v \rangle$ [km s^{-1}]	Mg II $\log N$ [cm^{-2}]	Mg II b [km s^{-1}]	Fe II $\log N$ [cm^{-2}]	Fe II b [km s^{-1}]	Mg I $\log N$ [cm^{-2}]	Mg I b [km s^{-1}]
0454 − 220	0.48334	−46.6	11.81 ± 0.05	0.92 ± 0.08	< 11.96	···	10.49 ± 0.24	6.25 ± 5.15
		−33.1	12.32 ± 0.01	3.88 ± 0.23	< 12.30	···	< 10.37	···
		−20.8	11.95 ± 0.03	2.19 ± 0.68	< 12.27	···	< 10.20	···
		−9.6	12.67 ± 0.49	3.78 ± 1.36	< 12.24	···	10.82 ± 0.25	4.71 ± 4.25
		−1.0	13.17 ± 0.11	5.69 ± 3.48	13.41 ± 0.10	7.75 ± 0.52	11.45 ± 0.07	2.83 ± 0.79
		5.3	13.00 ± 0.18	5.93 ± 0.80	< 12.28	···	11.58 ± 0.04	2.57 ± 0.74
		21.0	12.37 ± 0.01	4.55 ± 0.15	12.47 ± 0.14	4.00 ± 2.44	10.47 ± 0.17	2.57 ± 3.27
0823 − 223	0.91102	−139.2	12.49 ± 0.01	1.53 ± 0.12	12.21 ± 0.00	1.97 ± 0.68	10.76 ± 5.56	5.64 ± 4.65
		−119.3	12.35 ± 0.00	4.23 ± 0.29	12.22 ± 0.01	4.23 ± 0.77	10.92 ± 5.67	11.87 ± 22.52
		−117.7	12.44 ± 0.01	27.54 ± 2.05	< 10.95	···	< 10.57	···
		−67.5	13.25 ± 0.01	7.17 ± 0.15	13.04 ± 0.00	6.56 ± 0.20	11.93 ± 0.01	6.90 ± 0.44
		−52.4	12.80 ± 0.01	3.51 ± 0.32	12.33 ± 0.01	1.02 ± 0.17	11.47 ± 0.04	3.32 ± 0.72
		−43.2	12.27 ± 0.02	3.00 ± 0.50	11.98 ± 0.01	3.74 ± 1.16	< 10.91	···
		−29.3	12.02 ± 0.01	5.01 ± 0.54	11.53 ± 0.01	1.09 ± 0.87	10.69 ± 0.46	11.27 ± 10.67
		−2.2	12.27 ± 0.01	0.95 ± 0.20	11.92 ± 0.02	0.85 ± 0.21	< 10.90	···
		6.3	12.62 ± 0.04	2.58 ± 0.44	12.55 ± 0.01	0.96 ± 0.22	11.32 ± 0.34	11.53 ± 8.76
		8.2	12.98 ± 0.00	17.78 ± 0.65	12.81 ± 5.98	16.70 ± 1.27	< 10.55	···
		13.8	12.49 ± 0.01	3.22 ± 0.60	12.36 ± 0.01	3.57 ± 0.69	< 10.56	···
		46.2	12.53 ± 0.00	9.92 ± 0.40	12.43 ± 0.00	10.33 ± 0.97	< 10.18	···
		62.9	11.45 ± 0.03	0.77 ± 0.14	< 11.53	···	< 10.22	···
		131.2	12.48 ± 0.08	9.78 ± 1.08	12.37 ± 0.09	8.26 ± 1.70	11.09 ± 0.33	18.87 ± 12.10
		140.3	12.40 ± 0.11	3.53 ± 0.89	12.31 ± 0.11	1.96 ± 1.15	< 10.55	···
		150.1	12.68 ± 0.09	10.27 ± 2.05	12.62 ± 0.09	8.84 ± 2.03	11.13 ± 0.47	22.59 ± 15.07
		166.1	12.30 ± 0.05	3.93 ± 0.43	12.19 ± 0.05	1.88 ± 0.87	< 10.54	···
		216.5	11.79 ± 0.03	3.64 ± 0.59	12.02 ± 0.99	2.43 ± 1.99	< 10.54	···
1101 − 264	0.35900	−37.4	11.91 ± 0.05	10.37 ± 1.75	···	···	···	···
		−8.0	13.48 ± 0.04	7.92 ± 0.30	···	···	···	···
		14.0	12.18 ± 0.05	5.03 ± 1.03	···	···	···	···
		30.2	12.98 ± 0.02	6.26 ± 0.40	···	···	···	···
		46.6	12.42 ± 0.03	5.40 ± 0.48	···	···	···	···
		71.4	11.57 ± 0.07	3.99 ± 1.28	···	···	···	···
1148 + 384	0.55336	−79.8	12.56 ± 0.04	2.90 ± 0.27	13.23 ± 1.90	1.88 ± 0.97	< 10.92	···
		−49.4	12.78 ± 0.02	6.02 ± 0.24	12.61 ± 0.07	5.29 ± 1.34	< 10.91	···
		−6.0	12.64 ± 0.04	7.15 ± 0.74	12.32 ± 0.15	5.85 ± 3.01	< 10.92	···
		6.6	12.91 ± 0.04	4.11 ± 0.37	12.62 ± 0.08	3.16 ± 1.21	< 10.93	···
		25.6	12.41 ± 0.03	3.62 ± 0.34	11.88 ± 0.29	3.99 ± 5.13	< 10.94	···
		49.7	12.43 ± 0.03	3.79 ± 0.41	11.93 ± 0.24	2.91 ± 4.45	< 10.95	···
		63.6	12.09 ± 0.04	4.94 ± 0.83	< 12.00	···	< 10.95	···
		85.5	11.85 ± 0.05	3.52 ± 0.90	< 12.02	···	< 10.96	···
1206 + 459	0.92760	−403.5	11.92 ± 0.03	5.98 ± 0.55	< 11.47	···	< 10.40	···
		−350.7	12.16 ± 0.02	2.89 ± 0.26	< 11.48	···	< 10.41	···
		−327.7	12.12 ± 0.02	2.98 ± 0.28	< 11.48	···	< 10.40	···
		−256.8	12.35 ± 0.01	4.77 ± 0.20	< 11.48	···	< 10.41	···
		−188.0	12.01 ± 0.02	3.10 ± 0.37	< 11.49	···	< 10.40	···
		−174.2	11.60 ± 0.05	3.69 ± 0.89	< 11.49	···	< 10.41	···
		−62.8	11.72 ± 0.07	16.19 ± 3.54	< 11.47	···	< 10.40	···
		−29.0	13.44 ± 0.04	5.67 ± 0.15	12.75 ± 0.02	6.19 ± 0.27	11.03 ± 0.10	5.09 ± 1.51
		−13.3	11.53 ± 0.08	1.07 ± 0.26	< 11.50	···	< 10.43	···
		6.0	13.29 ± 0.01	7.38 ± 0.14	12.21 ± 0.06	8.52 ± 1.26	11.30 ± 0.10	10.42 ± 1.89
		30.4	12.60 ± 0.01	12.70 ± 0.49	< 11.45	···	< 10.41	···
		66.0	12.82 ± 0.01	5.08 ± 0.10	12.07 ± 0.05	2.85 ± 0.76	10.81 ± 0.29	12.34 ± 6.50
1222 + 228	0.66805	−28.2	12.05 ± 0.10	4.79 ± 1.22	11.89 ± 0.15	1.94 ± 3.20	< 10.60	···
		−15.4	12.73 ± 0.07	5.51 ± 1.12	12.11 ± 0.21	5.32 ± 3.74	10.91 ± 0.49	8.80 ± 13.8
		−4.9	12.70 ± 0.07	3.83 ± 1.02	12.58 ± 0.07	4.35 ± 1.20	10.66 ± 0.56	1.98 ± 5.81
		5.2	12.62 ± 0.04	3.65 ± 0.66	12.65 ± 0.14	1.52 ± 0.57	10.93 ± 0.18	4.70 ± 3.03
		19.7	12.68 ± 0.02	6.50 ± 0.41	12.27 ± 0.08	6.68 ± 1.89	10.94 ± 0.17	7.64 ± 4.01
		233.4	12.40 ± 0.02	5.19 ± 0.31	< 14.94	···	11.02 ± 0.22	8.06 ± 5.2
1241 + 176	0.55048	−8.4	13.07 ± 0.02	19.41 ± 0.58	< 12.92	···	11.29 ± 0.21	17.79 ± 8.42
		1.6	13.52 ± 0.15	5.90 ± 0.57	13.57 ± 0.05	7.59 ± 0.68	11.74 ± 0.06	5.79 ± 0.93
		40.5	12.31 ± 0.03	8.05 ± 0.65	12.19 ± 0.18	4.05 ± 3.34	11.42 ± 0.24	26.65 ± 18.87
		145.2	11.96 ± 0.05	6.54 ± 1.13	< 12.07	···	< 10.85	···

TABLE 7—*Continued*

System QSO	$z_{\rm abs}$	Cloud $\langle v\rangle$ [km s^{-1}]	MgII $\log N$ [cm^{-2}]	MgII b [km s^{-1}]	FeII $\log N$ [cm^{-2}]	FeII b [km s^{-1}]	MgI $\log N$ [cm^{-2}]	MgI b [km s^{-1}]
$1248+401$	0.77296	-29.6	12.66 ± 0.02	8.48 ± 0.43	12.27 ± 0.07	9.81 ± 2.05	<10.72	···
		-13.1	12.80 ± 0.16	5.66 ± 1.27	12.62 ± 0.15	5.31 ± 1.47	10.91 ± 0.48	7.77 ± 7.24
		-5.2	13.33 ± 0.04	7.41 ± 0.34	13.54 ± 0.03	3.39 ± 0.20	11.45 ± 0.17	1.12 ± 0.64
		12.6	12.31 ± 0.02	3.54 ± 0.40	12.04 ± 0.11	8.32 ± 3.06	<10.71	···
		23.8	11.70 ± 0.07	1.35 ± 0.88	<10.44	···	<10.74	···
		39.7	13.26 ± 0.02	6.51 ± 0.23	12.87 ± 0.02	4.22 ± 0.33	11.23 ± 0.48	5.80 ± 2.92
		52.2	11.89 ± 0.15	5.34 ± 1.31	11.70 ± 0.18	3.85 ± 3.43	<10.69	···
		225.2	12.30 ± 0.01	5.53 ± 0.24	11.98 ± 0.10	4.15 ± 1.98	11.16 ± 0.07	7.66 ± 1.89
$1254+044$	0.51939	-262.4	12.25 ± 0.04	3.31 ± 0.52	<12.17	···	<10.95	···
		-159.4	12.05 ± 0.05	6.28 ± 1.12	<12.15	···	<10.94	···
		-9.7	15.75 ± 0.10	3.18 ± 0.22	13.81 ± 0.15	4.73 ± 0.58	12.18 ± 0.04	6.36 ± 0.64
		4.1	12.86 ± 0.17	4.77 ± 2.83	13.37 ± 0.22	9.47 ± 6.24	11.17 ± 0.17	2.13 ± 3.30
		16.2	13.00 ± 0.09	7.95 ± 1.00	12.60 ± 0.64	7.36 ± 3.72	11.52 ± 0.12	12.90 ± 4.23
$1254+044$	0.93423	-37.6	12.72 ± 0.01	9.68 ± 0.27	11.90 ± 0.12	11.53 ± 4.10	<10.67	···
		4.3	13.07 ± 0.01	7.57 ± 0.16	12.66 ± 0.02	4.41 ± 0.34	11.00 ± 0.11	4.77 ± 2.01
$1317+274$	0.66005	-10.4	12.63 ± 0.04	7.29 ± 0.49	12.60 ± 0.04	6.53 ± 0.90	<10.54	···
		0.0	12.69 ± 0.04	4.55 ± 0.36	12.81 ± 0.04	2.49 ± 0.37	11.27 ± 0.07	4.48 ± 1.17
		11.6	12.02 ± 0.05	6.02 ± 0.77	11.99 ± 0.06	2.05 ± 1.50	<10.52	···
		47.5	11.50 ± 0.07	3.68 ± 1.21	<11.63	···	<10.54	···
		77.6	11.81 ± 0.11	6.98 ± 1.89	<11.63	···	<10.52	···
		89.7	11.92 ± 0.08	4.65 ± 1.04	12.00 ± 0.15	5.04 ± 2.52	<10.53	···
		100.2	11.77 ± 0.08	10.24 ± 2.19	11.88 ± 0.11	1.57 ± 3.20	<10.52	···
		140.4	11.75 ± 0.05	9.01 ± 1.48	<11.64	···	<10.52	···
$1421+331$	0.90287	-103.6	11.96 ± 0.14	7.57 ± 1.65	11.61 ± 0.18	~2.5	<10.69	···
		-87.8	12.77 ± 0.08	9.23 ± 1.71	11.93 ± 0.17	6.77 ± 3.75	<9.74	···
		-77.0	12.52 ± 0.11	3.56 ± 0.84	11.75 ± 0.22	4.90 ± 3.37	<10.69	···
		-59.7	12.65 ± 0.01	10.34 ± 0.45	12.13 ± 0.07	5.48 ± 1.36	<11.58	···
		-17.6	12.79 ± 0.04	3.37 ± 0.32	12.86 ± 0.10	0.76 ± 0.07	<10.70	···
		-8.2	12.93 ± 0.08	3.46 ± 0.85	12.48 ± 0.05	3.89 ± 0.79	<10.32	···
		7.6	13.29 ± 0.06	10.23 ± 2.03	12.77 ± 0.05	7.74 ± 1.35	10.74 ± 0.33	4.60 ± 4.43
		23.4	14.44 ± 0.85	4.03 ± 0.94	13.60 ± 0.02	4.99 ± 0.18	11.58 ± 0.06	7.47 ± 1.23
		65.2	11.62 ± 0.06	2.45 ± 1.24	<11.26	···	<10.72	···
		83.1	12.99 ± 0.03	4.41 ± 0.17	12.27 ± 0.07	5.49 ± 1.27	<10.70	···
$1421+331$	1.17261	-43.4	12.46 ± 0.03	4.08 ± 0.42	12.20 ± 0.06	1.91 ± 1.08	10.85 ± 0.38	6.83 ± 5.38
		-36.2	11.94 ± 0.10	4.88 ± 1.57	11.58 ± 0.16	0.93 ± 0.63	<10.27	···
		-17.9	12.57 ± 0.03	6.71 ± 0.63	12.32 ± 0.04	6.36 ± 0.99	<10.14	···
		0.6	13.11 ± 0.02	7.23 ± 0.36	12.75 ± 0.02	6.32 ± 0.45	11.53 ± 0.07	10.59 ± 2.62
		20.2	12.06 ± 0.06	4.09 ± 1.03	~12.3	~0.2	<10.08	···
		28.9	11.96 ± 0.22	2.26 ± 1.76	<10.95	···	10.72 ± 0.60	~4.5
		35.8	12.75 ± 0.07	2.95 ± 0.49	12.32 ± 0.09	4.86 ± 1.08	10.81 ± 0.32	~3.1
$1634+706$	0.99024	-21.9	13.11 ± 0.01	7.39 ± 0.15	12.77 ± 0.02	5.19 ± 0.27	11.35 ± 0.04	6.85 ± 0.74
		-10.0	12.17 ± 0.11	2.15 ± 0.81	12.15 ± 0.09	4.33 ± 1.57	<9.97	···
		1.7	12.82 ± 0.16	6.46 ± 0.86	12.38 ± 0.13	4.20 ± 1.12	10.85 ± 0.48	7.65 ± 5.33
		12.9	13.10 ± 0.09	16.68 ± 2.40	12.33 ± 0.22	12.47 ± 5.54	11.30 ± 0.30	17.59 ± 5.69
		24.7	12.09 ± 0.20	5.03 ± 1.34	<11.49	···	<10.39	···
$2128-123$	0.42973	-39.8	12.38 ± 0.04	7.66 ± 0.91	···	···	<10.47	···
		-25.7	12.01 ± 0.08	3.48 ± 1.23	···	···	11.37 ± 0.14	9.03 ± 4.18
		-0.6	15.24 ± 0.51	4.45 ± 0.46	···	···	12.12 ± 0.03	4.98 ± 0.48
		12.2	13.49 ± 0.07	5.58 ± 0.47	···	···	11.70 ± 0.08	6.39 ± 1.52
$2145+064$	0.79078	-109.5	12.55 ± 0.00	2.04 ± 0.01	~10.1	~24.8	~0.0	···
		-101.7	13.38 ± 0.06	2.42 ± 0.08	12.82 ± 0.02	3.86 ± 0.36	<10.69	···
		-3.4	12.56 ± 0.15	1.04 ± 0.17	<11.82	···	<10.78	···
		3.6	12.57 ± 0.02	14.12 ± 0.58	<11.79	···	<10.71	···
		63.3	12.76 ± 0.01	9.91 ± 0.32	12.39 ± 0.09	5.28 ± 1.65	<10.69	···
		86.6	12.18 ± 0.04	8.86 ± 1.00	11.86 ± 0.23	~1.6	<10.72	···

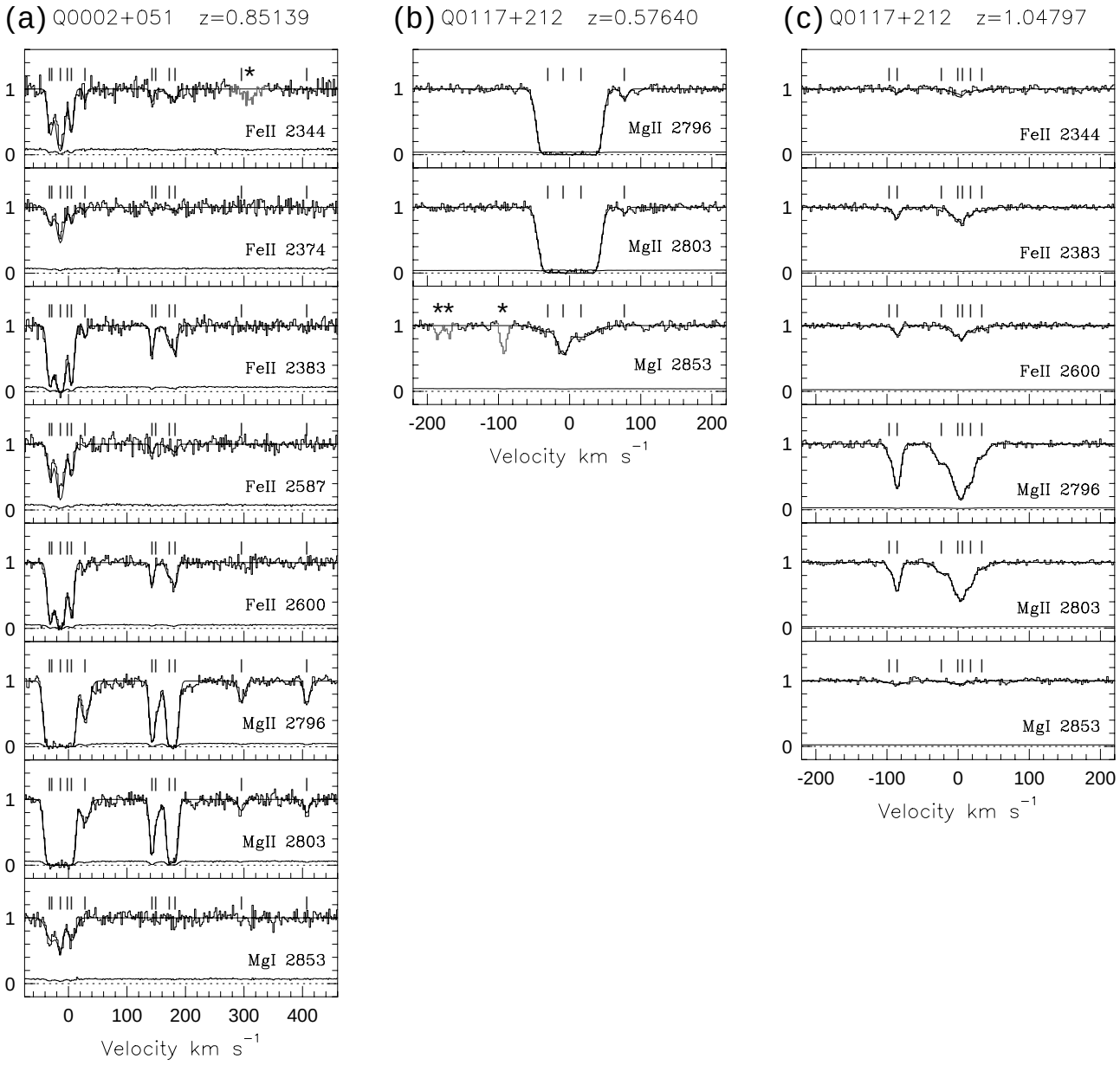

FIG. 2.— The HIRES/Keck profiles of detected transitions for systems in the $0002+051$ and $0117+212$ spectra. The data are aligned in rest–frame velocity. Ticks above the normalized spectra are the centroids of the VP components. The VP model spectra (the fits) are shown as solid curves superimposed upon the data.

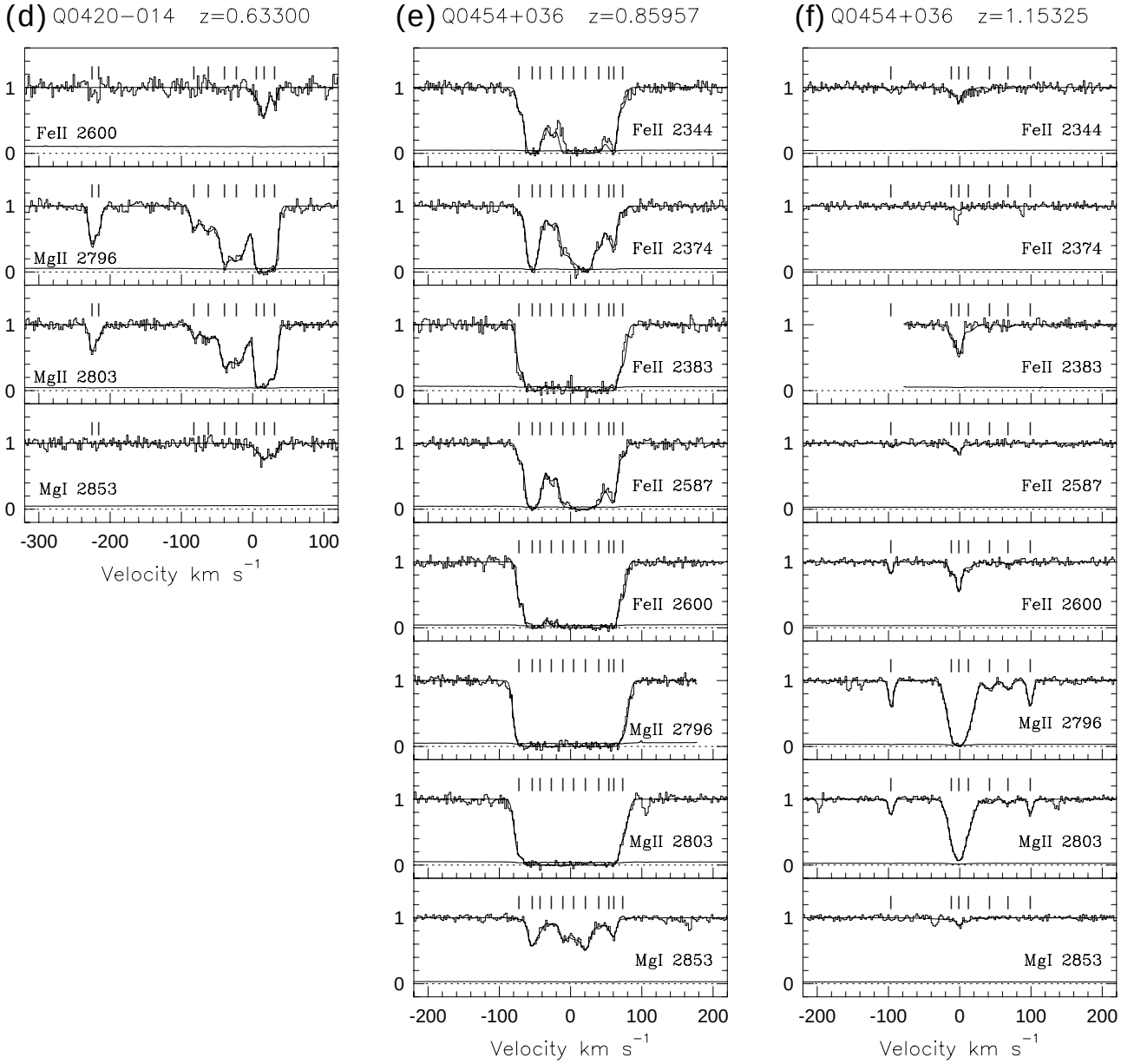

FIG. 2. CONT.— Same as for Figures 2*a*–*c*, but for $0420-014$ and $0454+036$.

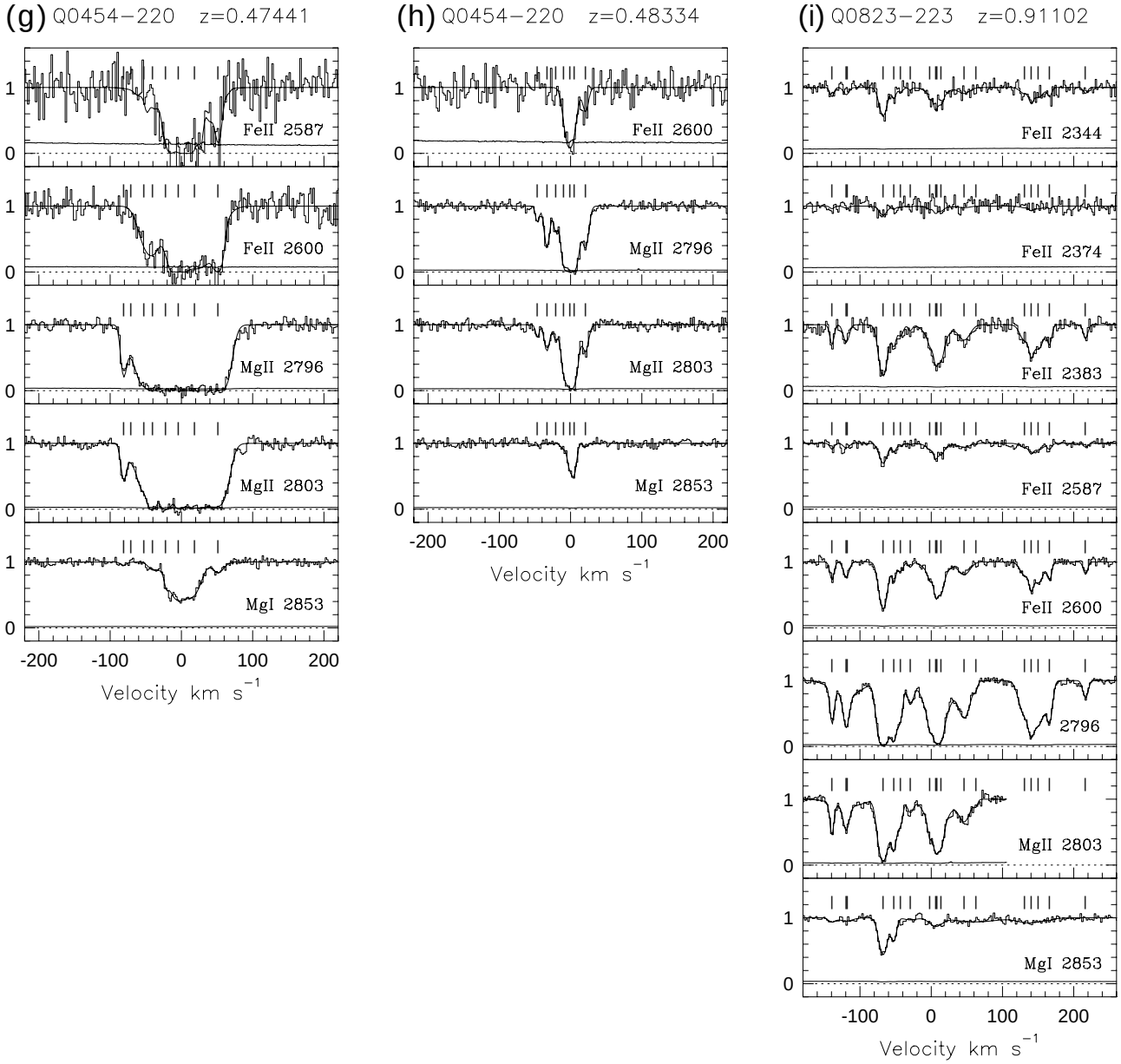

FIG. 2. CONT.— Same as for Figures 2*a*–*c*, but for 0454 − 220 and 0823 − 223.

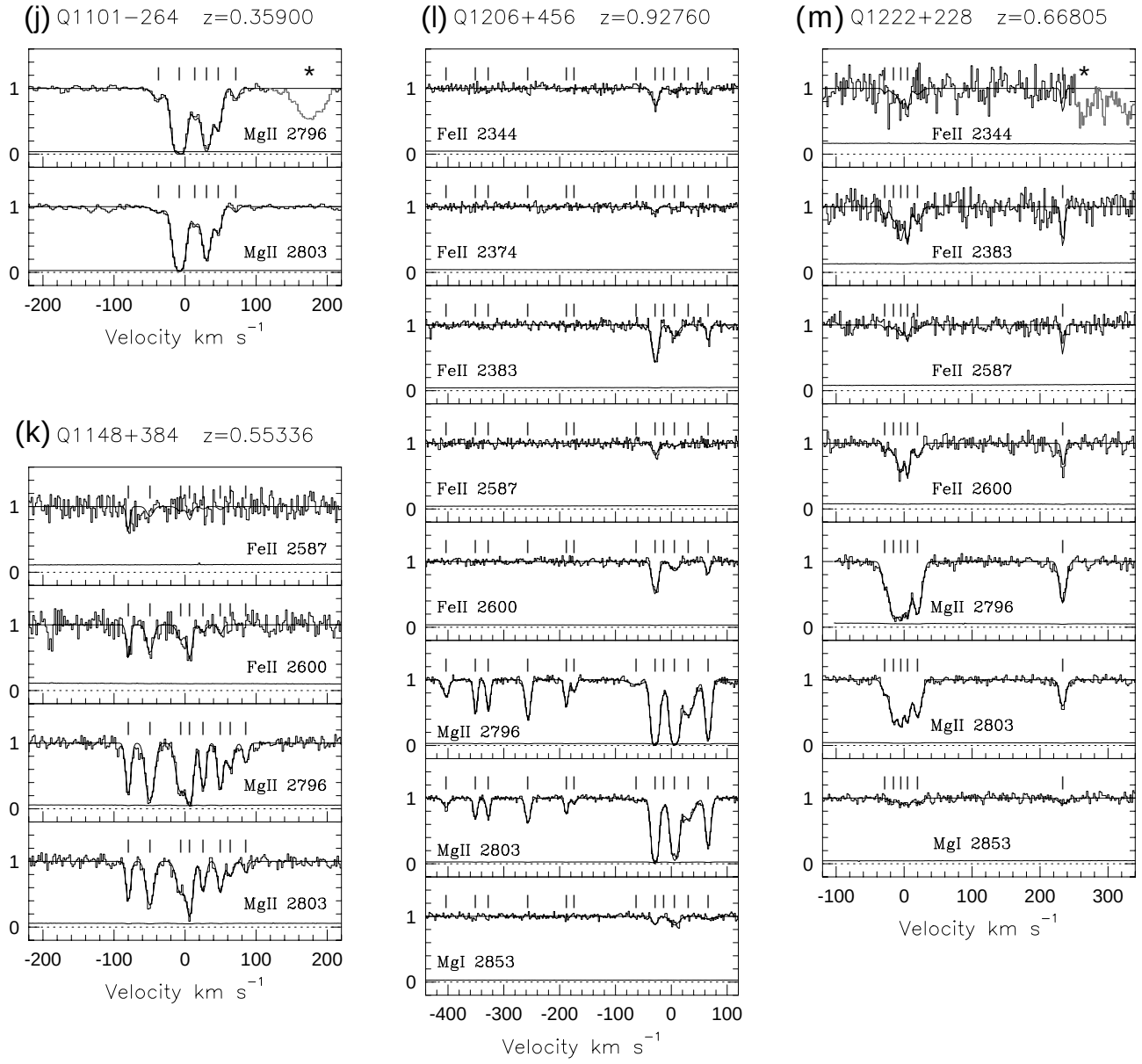

FIG. 2. CONT.— Same as for Figures 2*a*–*c*, but for $1101-264$, $1148+384$, $1206+459$, and $1222+228$.

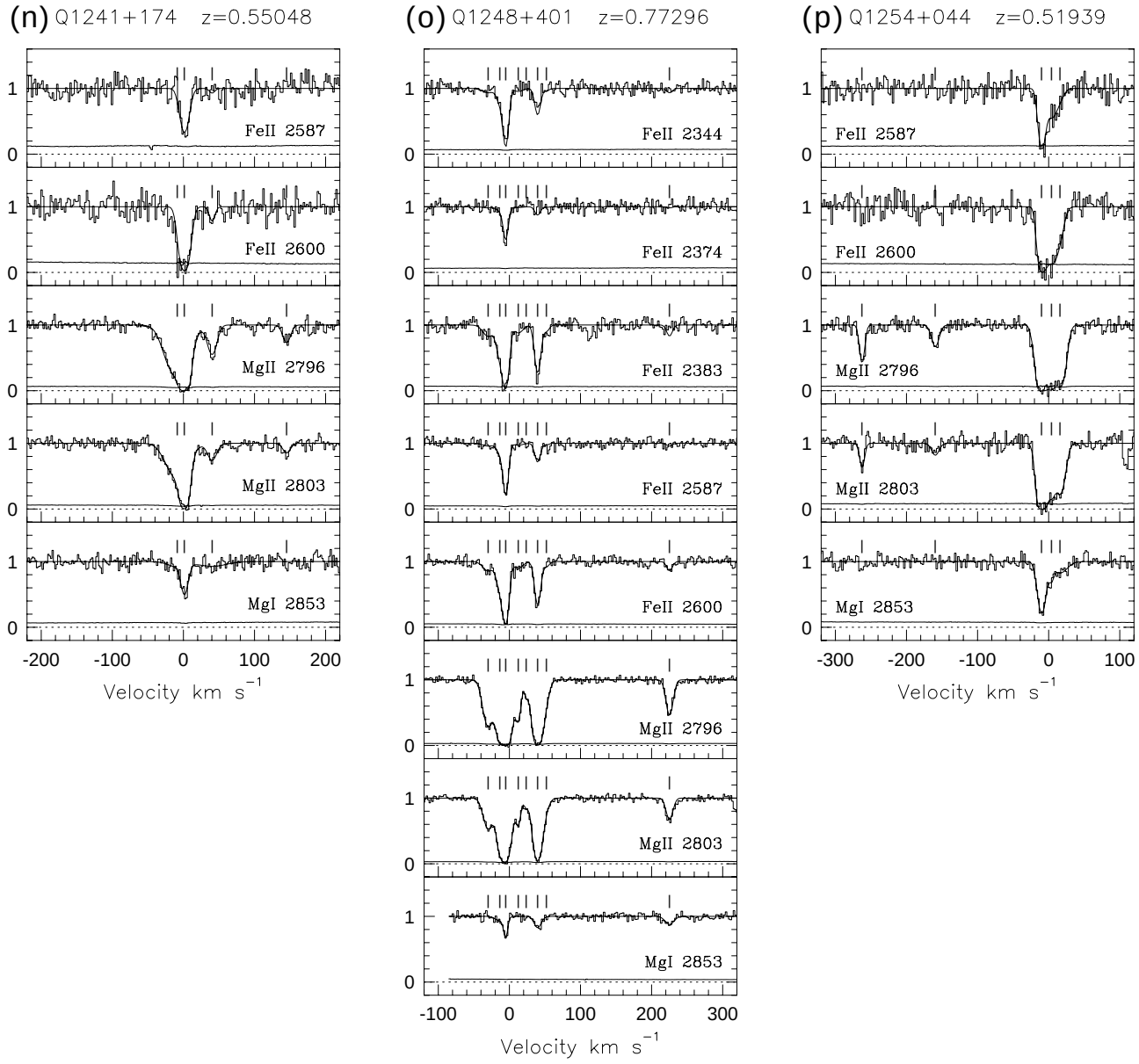

FIG. 2. CONT.— Same as for Figures 2*a*–*c*, but for 1241 + 174, 1248 + 401, and 1254 + 044.

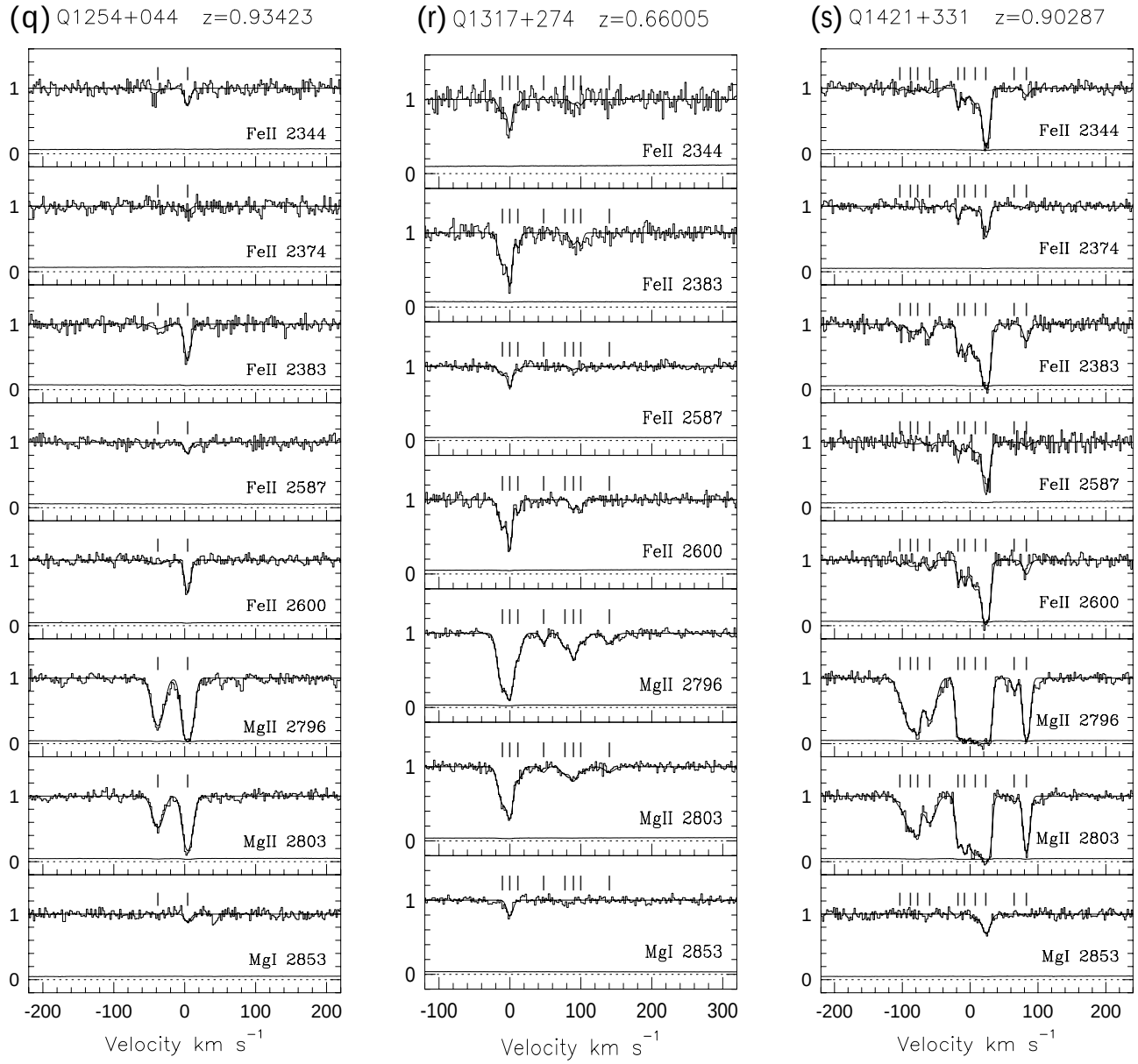

FIG. 2. CONT.— Same as for Figures 2*a*–*c*, but for $1254+044$, $1317+274$, and $1421+331$.

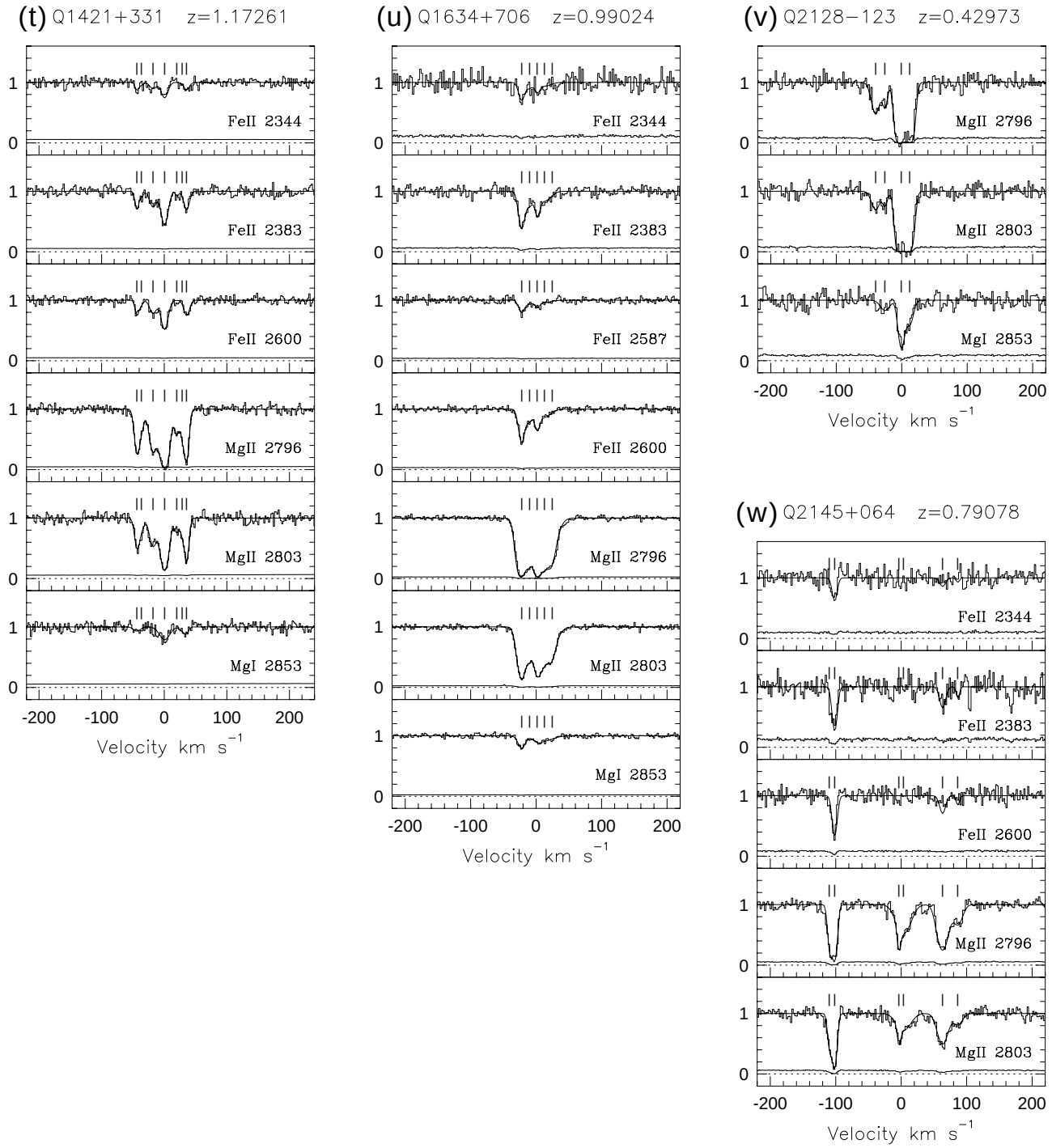

FIG. 2. CONT.— Same as for Figures 2*a*–*c*, but for $1421+331$, $1634+706$, $2128-123$, and $2145+064$.